From accretion to outflows of massive protostars

Dissertation

der Mathematisch-Naturwissenschaftlichen Fakultät
der Eberhard Karls Universität Tübingen
zur Erlangung des Grades eines
Doktors der Naturwissenschaften
(Dr. rer. nat.)

vorgelegt von
Anders Kölligan, M.Sc.
aus Köln

Tübingen
2018

Gedruckt mit Genehmigung der Mathematisch-Naturwissenschaftlichen Fakultät
der Eberhard Karls Universität Tübingen.

Tag der mündlichen Qualifikation	12.10.2018
Dekan:	Prof. Dr. Wolfgang Rosenstiel
1. Berichterstatter:	Dr. Rolf Kuiper
2. Berichterstatter:	Prof. Dr. Wilhelm Kley

Preface

This thesis is based on two projects that I worked on during my dissertation and that are planned to be published separately within the next months. The goal of the first and main project is the magneto-hydrodynamic simulation of a massive prestellar collapse with a focus on jets and outflows. This project is described in chapter 2. The topic of the second project is a frequently observed asymmetry in position-velocity diagrams of protostellar accretion disks, that can be explained by multiple resonances of molecular lines. It is found in chapter 3.

I wrote the full text of this thesis and produced all data for both projects myself. However, my collaborators, especially my supervisor Rolf Kuiper, were always by my side, discussing results and questions, contributing ideas and theories, proof-reading, suggesting edits of the text etc. Therefore, I was never alone with my research and writing and will in the following use "we" instead of "I" when writing in the first person.

Thus, first of all, I want to thank Rolf Kuiper for his friendship, valuable counsel, his dedication to introduce me to his collaborators and friends, the opportunity to travel to so many amazing places, and the great time that we spend together. I also want to express my gratitude to my friend, collaborator, and senior researcher Dylan Kee who helped me greatly with his explanations, our discussions and his diligent proof-reading. I greatly enjoyed the time we spent together on conferences, in Tübingen, Delaware, Cologne, or anywhere else.

Also I want to thank my other close collaborators, Alberto Sanna and Katharine Johnston, for their suggestions on the second project and our other work together, as well as the fun time I had working with them. Last but not least, I want to thank Christian Fendt, Ralf Pudritz, Neal Turner, Harold Yorke, Andrea Mignone, Shu-Ichiro Inutsuka, and Daniel Seifried, for the fruitful discussions and explanations.

However, I would never have been able to get so far without the support of my family, first of all, my wife Vera and my brother Sören who have always been there for me. I also wish to express my gratitude to my uncle Johannes and his wife Ellen, who gave me backing and shared their life experience with me when my parents couldn't. To close my acknowledgments, I want to thank my supportive and caring grandparents, Maria and Heinrich.

Finally, I wish everyone an informative and inspiring read of my thesis.

Tübingen, 2018

Anders Kölligan

Abstract

Massive stars live short but intense lives. While less numerous than low-mass stars, they enormously impact their surroundings by several feedback mechanisms. They form in opaque and far-away regions of the galaxy, such that one of these feedback mechanisms also becomes one of few records of their evolution: their bright large-scale outflows. Their emergence and related phenomena, such as the accretion disk that launches them, comprise the main focus of this thesis.

In chapter 2, we present our magneto-hydrodynamic (MHD) simulations that were conducted with non-ideal MHD, self-gravity, and very high resolutions as they have never been achieved before. In our comprehensive convergence study, we investigate computational conditions necessary to resolve (pseudo-) disk formation and outflow launching processes, and we analyze possible caveats. We explore the magneto-hydrodynamic processes of the collapse of a massive prestellar core, including an analysis of the forces involved and their temporal evolution. We follow the initial 100 $M_\odot$ cloud core for up to two free-fall times, during which it collapses under its own self-gravity to self-consistently form a dense disk structure that eventually launches outflows. The setup allows us not only to show a comprehensive evolutionary picture of the collapse, but also enables the resolution of highly-collimated magneto-centrifugal jets and magnetic pressure driven tower flows as separate structures. This is only possible in very high resolutions and is, to our knowledge, the first time this has been achieved. Of the two outflow components, the tower flow dominates angular momentum transport, while the mass outflow rate is dominated by the entrained material from the interaction of the jet with the stellar environment and just a part of the ejected medium is directly launched from the accretion disk. Taking into account both the mass launched from the disk's surface as well as the entrained material from the envelope, we find an ejection-to-accretion efficiency of 10%. Additionally, a tower flow can only develop to its full extent when much of the original envelope has already dispersed as otherwise the ram-pressure of the infalling material inhibits the launching on wider scales. We argue that non-ideal MHD is required to form centrifugally supported accretion disks and that the disk size is strongly dependent on spatial resolution. We find that a converged result for disk and both outflow components requires a spatial resolution of $\Delta x \leq 0.17$ au at 1 au and a sink cell size of ≤ 3.1 au. Our results indicate that massive stars not only possess slow wide-angle tower flows, but also produce magneto-centrifugal jets, just as their low-mass counterparts. Therefore, the actual difference between low-mass and high-mass star formation lies in the embededness of the high-mass star. This implies that the jet and tower flow interact with the infalling large-scale stellar environment, potentially resulting in entrainment.

In chapter 3, we investigate the occurrence of observed asymmetries in position-velocity diagrams and show how even symmetric objects can produce them. To this end, we give a qualitative description of the idea, backed up by direct integration of the line radiation transport equation including the effect of resonances. We show that these asymmetries naturally arise by reabsorption when infall (or outflow) velocities and rotational velocities are of the same magnitude, such that the emission from the warm, central regions of the accetion disk is absorbed in the colder outer regions of the envelope as they reach the same line-of-sight velocities. These multiple resonances of the molecular lines can be considered a special case of self-absorption.

Zusammenfassung

Massereiche Sterne führen kurze, aber sehr intensive Leben. Zwar sind sie deutlich seltener als Sterne mit geringerer Masse, doch üben sie, durch unterschiedliche Rückkopplungsprozesse, einen enormen Einfluss auf ihre Umgebung aus. Da sie in undurchsichtigen und weit entfernten Regionen unserer Galaxie entstehen, wird einer dieser Prozesse zu einem Dokument ihrer Entwicklung: ihre hell leuchtenden, weit ausgedehnten Ausflüsse. Ihre Entstehung und Phänomene, die mit ihnen in Zusammenhang stehen, wie die Akkretionsscheibe, von der sie gestartet werden, stellen den Fokus dieser Arbeit dar.
In Kapitel 2 stellen wir unsere Magneto-Hydrodynamik-Simulationen vor, die mit nicht-idealer Magneto-Hydrodynamik, Eigengravitation und bisher unerreicht hohen Auflösungen durchgeführt wurden. In unserer umfassenden Konvergenzstudie untersuchen wir, welche numerischen Parameter notwendig sind, um (Pseudo-)Scheibenentstehung und die Startprozesse von Ausflüssen auflösen zu können und erörtern mögliche Probleme. Wir erforschen die magneto-hydrodynamischen Prozesse, die beim Kollaps eines prestellaren Kerns auftreten, inklusive einer Analyse der dazugehörigen Kräfte und deren Zeitentwicklung. Wir folgen dem anfänglichen 100 $M_\odot$ Wolkenkern für bis zu zwei Freifallzeiten, während der er, durch seine Eigengravitation, kollabiert und selbstkonsistent eine dichte Scheibenstruktur bildet, die schließlich Ausflüsse startet. Dieses Setup ermöglicht es uns nicht nur ein umfassendes Bild der Zeitentwicklung des Kollapses zu zeigen, sondern auch eng gebündelte magneto-zentrifugale Jets und, durch den magnetischen Druck getriebene, Tower-Flows als separate Strukturen aufzulösen. Dies ist nur mit sehr hohen Auflösungen möglich und ist, soweit uns bekannt ist, das erste Mal, dass dies erreicht wurde. Von beiden Ausflusskomponenten dominiert der Tower-Flow den Drehimpulstransport, während der Massetransport durch mitgerissenes Material, aus der Wechselwirkung von Jet und des stellaren Umfelds beherrscht wird und nur ein Teil aus der Akkretionsscheibe stammt. Wenn beides, also das Material aus der Akkretionsscheibe, sowie das mitgerissene Material, berücksichtigt wird, erhalten wir eine Auswurf-zu-Akkretions-Effizienz von 10%. Zusätzlich kann ein Tower-Flow sich nur vollständig ausbilden, wenn ein großer Teil der ursprünglichen Hülle bereits aufgelöst ist, da sonst der dynamische Druck des einfallenden Materials die Beschleunigung auf größeren Skalen verhindert. Wir schlussfolgern zum einen, dass nicht-ideale MHD notwendig ist, um zentrifugal gestützte Akkretionsscheiben zu bilden, und zum anderen, dass die Scheibengröße stark von der räumlichen Auflösung abhängt. Darüber hinaus benötigt ein konvergiertes Ergebnis für die Scheibe, als auch die beiden Ausflusskomponenten, eine räumliche Auflösung von $\Delta x \leq 0.17$ au bei 1 au und eine Senkzellengröße von ≤ 3.1 au. Unsere Ergebnisse weisen darauf hin, dass massereiche Sterne nicht nur langsame, weitwinklige Tower-Flows, sondern auch magneto-zentrifugale Jets besitzen, genau wie ihre niedrigmassigen Gegenstücke. Somit liegt der tatsächliche Unterschied zwischen niedrigmassiger und massereicher Sternentstehung in der Einbettung von massereichen Sternen in deren Umgebung. Dies impliziert, dass der Jet und der Tower-Flow mit der einfallenden großskaligen Umgebung interagieren, was wiederum potentiell zum Mitreißen von Material führt.
In Kapitel 3 untersuchen wir das Auftreten von beobachteten Asymmetrien in Position-Geschwindigkeits-Diagrammen und zeigen, wie sogar symmetrische Objekte diese produzieren können. Dazu geben wir zunächst eine qualitative Beschreibung, die wir mit der direkten Integration der Strahlungstransportgleichung, inklusive dem Effekt von Resonanzen,

stützen. Wir zeigen, dass diese Asymmetrien natürlicherweise durch Reabsorption auftreten, wenn Einfall- (oder Ausfluss-) Geschwindigkeiten ähnliche Werte zur Rotationsgeschwindigkeit haben. In Folge kann die Emission der warmen, zentralen Regionen der Akkretionsscheibe in den kälteren, äußeren Regionen der Umgebung absorbiert werden, wenn die gleichen Geschwindigkeiten entlang der Sichtlinie erreicht werden. Diese multiplen Resonanzen von molekularen Spektrallinien bilden einen Spezialfall von Selbstabsorption.

Contents

Chapter 1

Introduction

Stars are with us every hour of every day. During the day, the sun provides us with heat and light, and during the night we can see a vast field of a virtually uncountable number of stars. They are undoubtedly fascinating objects. Unfortunately, they are very distant and our sources of information on them are rather limited. While we receive other types of particles as well, such as cosmic rays and neutrinos, their electromagnetic radiation already contains vast amounts of information.

1.1 Star formation

Historically, stars were primarily distinguished by absorption lines in their spectra and the intensity of their radiation. Based on their spectra, hydrogen burning stars are divided into different classes denoted by the letters O, B, A, F, G, K, and M. These classes translate into different surface temperatures and with that to peaks in different parts of the electromagnetic spectrum. This also means that they appear to have different colors. Since they were originally thought to represent stellar evolutionary stages, the O-end of the classification is also called "early" and the M-end is called "late". In addition to these spectral classes, subcategories have been added, enabling a more precise classification. They divide each class into 10 parts, stretching from the numbers 0 to 9, with subcategory 0 having the highest surface temperature, and subcategory 9 the lowest. For historical reasons, the highest temperature subcategory of spectral class O is O2. Eventually, the classification system for hydrogen burning stars reaches from a very hot "early" O2 star (with a surface temperature of $\simeq 40000$ K) to a rather cool "late" M9 star (with a surface temperature of just $\simeq 2300$ K).[1] All stars spend most of their lifecycle burning hydrogen to helium. This stage of their evolution is called the *main sequence*. For such stars, the surface temperature is directly related to their mass and radius, where high-mass O stars shine brightly in white-blue and low-mass M stars appear dimly red. Since these hydrogen burning stars are stable over long periods of time, they are in force equilibrium of self-gravity and thermal pressure. This stability in time also implies that they have to be in thermal equilibrium and radiate away all the energy released by nuclear fusion. Therefore, the relation between luminosity L, effective temperature T, and stellar radius $R_\star$ is known:

$$L_\star = 4\pi R_\star^2 \sigma_\mathrm{B} T_\mathrm{eff}^4 \,, \tag{1.1}$$

[1] Our own sun with a surface temperature of 5800 K is a G2 star.

with σ_B the Stefan-Boltzmann constant and T_{eff} the effective (black body) temperature of the star.
The optical properties of the matter between astronomical objects and observers on earth also influence their observations significantly. As a result, a star's true luminosity is not immediately accessible by observation and since its radius is not known either, astronomers use another measure to describe the color of an object: the *color index*. It is defined as the difference of the fluxes in the visual and the blue band. When it is cleaned from possible influences such as dust absorption, emission, and reddening, it is called the *intrinsic color index*, and can be used to calculate the surface temperature of stars.
To characterize stars based on their luminosities, a system of magnitudes is used. As stars emit their radiation (to first order) equally in all directions, the intensity that reaches us on earth reduces with distance. This has to be accounted for and, consequently, astronomers normalize their absolute magnitudes to a distance of 10 pc. The result is the absolute magnitude of a star. For the visual band, it is given by

$$M_{\text{vis}} = -2.5 \log F_{\text{vis}}(10\ \text{pc}) + \text{constant}\,, \tag{1.2}$$

with the flux in the visual band F_{vis} and the constant chosen such that the magnitude of an A0 star on the main sequence is 0.
Combining both the absolute magnitude and the surface temperature, stars can be characterized very well by the *Hertzsprung-Russel* (HR) diagram, which is a plot of the absolute visual magnitudes (or luminosities) against the color index (or surface temperatures). HR diagrams are powerful tools to visualize stellar populations and their evolutionary sequences. An example of a theoretical HR-diagram (i.e. an HR-diagram using luminosities and temperatures) is presented in Fig. 1.1.

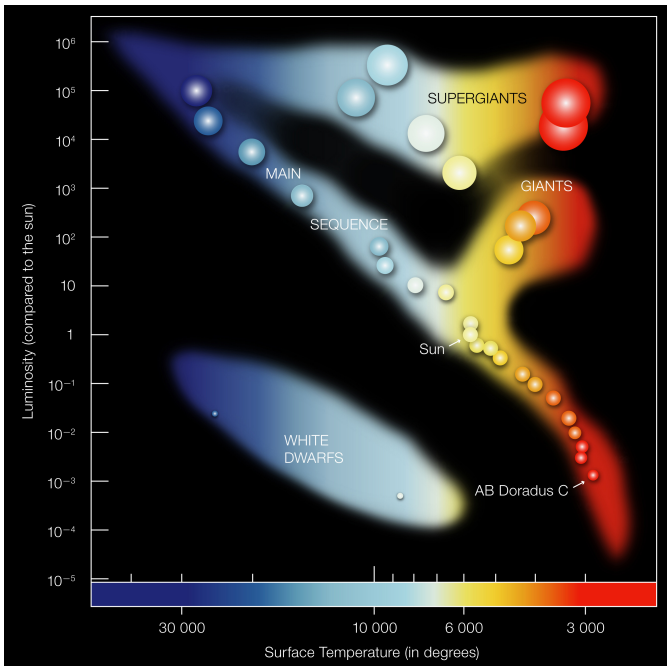

Figure 1.1: An example of a theoretical HR-diagram showing the position of the sun w.r.t. the main sequence, the giant branches, and the white dwarfs. (Credit: ESO)

The main sequence is typically populated by most stars, as they spend most of their lifetime burning hydrogen to helium, and is visible as a band of stars going from high luminosities (low magnitudes) and high temperatures (low color indices) to low luminosities (high magnitudes) and low temperatures (high color indices) as described by Eqn. (1.1). This corresponds to the colored diagonal going from the top-left to the lower-right in Fig. 1.1. Consequently, main-sequence O stars are found in the top-left and red dwarfs in the lower-right. During their hydrogen burning phase, stars move only a small amount w.r.t. the main sequence. Therefore, the main sequence acts as a reference point for other stellar evolutionary stages represented in the HR-diagram. Later evolutionary stages include the giants that are situated towards higher luminosities and lower temperatures and white dwarfs that are situated towards lower luminosities and higher temperatures. However, the focus of the present work is star formation and, consequently, the early phases of stellar evolution are discussed in the following sections.

1.1.1 Giant molecular clouds, clusters, and cores

Ultimately, stars are made from interstellar medium (ISM). ISM mainly consists of hydrogen and helium, with a small fraction of heavier elements. Consequently, it is classified by its predominant state of hydrogen. There are three phases we distinguish. Hydrogen is found as atomic hydrogen or HI, ionized hydrogen or HII, and, most importantly for star formation, molecular hydrogen H_2. The states of hydrogen correspond to different average temperatures and, as the transition regions between different phases are very narrow, these phases can be distinguished comfortably.
Star formation requires clouds of relatively cold molecular gas, such that gravity can overcome thermal pressure support locally. Gas that fulfils this requirement is predominantly found in *giant molecular clouds* (GMCs) and most of the star formation in these GMCs is localized in regions with increased densities: the *star forming clumps* or *protoclusters*. As GMCs are generally considered to be gravitationally bound objects, stabilized primarily by turbulence and magnetic fields, there have to be mechanisms to form star forming clusters, i.e. mechanisms that can make *subcritical* (supported) GMCs *supercritical* (able to collapse). The support by magnetic fields can be reduced either by ambipolar diffusion (a non-ideal MHD effect) or super-Alfvénic turbulence, i.e. turbulence with higher velocities than the magneto-acoustic waves[2], which can lead to magnetic reconnections, converting magnetic energy into radiation. Turbulence dissipates naturally on timescales comparable to the time it takes to form clumps, though it can be replenished by various effects. However, it can also lead to enhanced densities on small scales.[3] The result eventually is a perturbation in the previously stable hydrostatic equilibrium of the region that is not dampened naturally anymore, but instead increases exponentially. Therefore, locally the gravitational pull overwhelms thermal pressure. Such a gravitational instability occurs when a region reaches the *Jeans mass*

$$M_{\mathrm{J}} = \left(\frac{k_{\mathrm{B}}T}{G\mu m_{\mathrm{H}}}\right)^{3/2} \rho^{-1/2}, \tag{1.3}$$

where k_{B} is the Boltzmann constant, ρ is the density, G is the gravitational constant, μ is the molecular mass, and m_{H} the mass of atomic hydrogen. A clump typically contains many Jeans

[2]More information is found in 1.3.1.

[3]The relative importance of these effects is a matter of active research, though all of these effects can contribute to form a clump.

masses and, therefore, can rapidly fragment into several prestellar cores. The distribution of prestellar cores is described by the *core-mass function* (CMF). The shape of the CMF is another topic of active research, as it is unclear how exactly the CMF relates to the *initial mass function* (IMF) that describes the distribution of stars when they first reach the main sequence. This is particularly relevant for the formation of massive stars, as massive clusters may fragment into very numerous smaller cores, forming predominantly low-mass stars. For low- to few solar mass stars, however, we have a well-established picture on how they evolve from cores to fully developed hydrogen-burning stars.

1.1.2 Protostellar evolution

The formation process of a typical low- to a few solar mass star can be divided into several phases. Larson [1969], who conducted the first collapse simulation of a prestellar core, was the first to describe these phases in detail, thereby giving us insights into the inner workings of a prestellar core. Starting from a marginally stable core in a GMC, an event like an external shock wave, feedback from other stars, the dissociation of the stabilizing magnetic fields or of turbulence can lead to an increased density, resulting in a gravitational instability. In the collapse that follows, the potential energy of the core can be radiated away efficiently due to its relatively low optical depth. The characteristic timescale of this collapse is the free-fall time

$$t_{\mathrm{ff}} = \left(\frac{3\pi}{32\, G\, \rho}\right)^{-1/2} \tag{1.4}$$

that the core would need to completely contract, considering only gravity. As the density increases, the optical depth of major portions of the core approach unity. This means that the heat from the gravitational collapse becomes trapped and the temperature in the center rises while the material is compressed further since the collapse does not stop and more material is accreted. The rising density and temperature increase the thermal pressure up to a point when it becomes comparable to gravity, halting the collapse. This fist stage of hydrostatic equilibrium is called *first Larson-core* or just *first core* and it marks the onset of the main accretion phase. Due to the pressure exerted by the infalling material and its own self-gravity, this first core still continues to contract. Because the heat released by this contraction cannot escape radiatively, this process is effectively an adiabatic contraction with an adiabatic index $\gamma \simeq 5/3$, corresponding to a monatomic ideal gas. As more energy is converted, the temperature rises until the first vibrational degrees of freedom of H_2 can get excited, which then changes the effective adiabatic index to that of a diatomic molecule $\gamma \simeq 7/5$. While this reduces the subsequent temperature increase, the core continues to heat up until the temperature reaches $\simeq 2000$ K where the dissociation of H_2 begins. The heat consumed by dissociation of H_2 prevents the temperature from rising much further, while the core continues to contract, thereby increasing its density to a point where gravity can overcome thermal pressure support again. What follows is the *second collapse* of the first core. Finally, when most of the H_2 is dissociated, thermal pressure builds up again and stabilizes a *second (hydrostatic) core*. This second core is the actual *protostar*.
Since the initial core rotates, angular momentum conservation always leads to a higher densities in the midplane perpendicular to the axis of rotation. This results first in a rotationally flattened envelope and, consequently, in the formation of a centrifugally supported accretion disk. The accretion disk plays an important role for the subsequent formation of the

star, as it regulates the accretion process, can launch jets and outflows, and eventually forms planets, brown dwarfs, and stellar companions. For massive stars it also enables accretion despite high radiation pressures from the protostar.
During this phase, deuterium burning starts and together with gravitational contraction provides energy and thereby the protostar's luminosity. Meanwhile, the continuous accretion to the protostar reduces the optical depth of the surrounding envelope and the protostar becomes optically detectable. At this point in time, a large part of the core is already depleted. Therefore, this is considered the end of the main accretion phase; the protostar becomes a *pre-main-sequence* star. This also means that the deuterium supply ceases, leaving only gravitational contraction as source of energy. The succeeding pre-main-sequence phase is the topic of next section.

1.1.3 The pre-main-sequence

The point when protostars first become optically visible and appear in the HR diagram is called the *birthline*. From this point in time until they reach the main sequence they are considered pre-main-sequence stars[4]. The contraction process changes their luminosity and effective temperature relatively rapidly. As a result, their position in the HR-diagram changes correspondingly. The characteristic timescale, these pre-main-sequence stars need to radiate away a significant portion of their thermal and gravitational energy, is given by their *Kelvin-Helmholtz* (contraction) *time*

$$t_{\mathrm{KH}} = \frac{G\, M_\star^2}{R_\star\, L_\star}\,. \tag{1.5}$$

Combining this equation with Eqn. (1.1)[5] shows that the Kelvin-Helmholtz time is critically dependent on the effective temperature as $t_{\mathrm{KH}} \propto T^{-4}$. The effective surface temperature is a great deal higher for more massive objects than for lower mass objects and, consequently, massive pre-main-sequence stars contract significantly faster than their low-mass counterparts. For example, a solar mass star has a Kelvin-Helmholtz time of $\simeq 10^7$ yr, while a 10 $\mathrm{M}_\odot$ star has a Kelvin-Helmholtz time of just $\simeq 10^5$ yr. As they continue to contract, their core temperatures and densities eventually reach values sufficient to start hydrogen fusion, at which point they have finally reached the main sequence, more specifically the zero-age main sequence.
This evolutionary picture changes, though, for very massive stars. For a core of > 8 $\mathrm{M}_\odot$ the Kelvin-Helmholtz time approaches the free-fall time, and thus hydrogen fusion can start even before the protostar is visible. The evolution of massive stars is discussed in the next section.

1.1.4 Massive star formation

Unfortunately, we do not have such a complete picture of the formation process of massive stars as we have for lower mass stars. Currently, two formation modes for massive star formation are considered: *core accretion* and *competitive accretion and coalescence*.

[4] Very massive stars arguably do not have a well-defined pre-main sequence phase, as they ignite nuclear fusion while still accreting. Therefore, it is a matter of semantics if they are considered pre-main-sequence or already on the main-sequence.

[5] Eqn. (1.1) is not strictly valid, since the object is not in hydrostatic equilibrium, though on these timescales it is a good estimate.

The core accretion model assumes that high-mass star formation is basically a scaled-up version of low-mass star formation with the important difference of significantly higher time-averaged accretion rates of the order of up to 10^{-3} $M_\odot$ yr^{-1}. For comparison, accretion rates in low-mass star formation are highly episodic and on average at least two to three orders of magnitude lower [Audard et al., 2014]. Therefore, massive star formation requires a gravitationally bound core of sufficient mass as initial condition. To concentrate so much mass, the core needs some kind of support against fragmentation, although the nature of this support has not yet been conclusively found, there are possible explanations for this. Krumholz and McKee [2008] suggest that nearby low-mass protostars provide support in the form of radiative feedback, while Kunz and Mouschovias [2009], as well as Tan et al. [2013] suggest magnetic fields should be able to stabilize the core.
Under these preconditions, the subsequent collapse of the prestellar core and the protostellar formation process must still differ from the low-mass formation process. As mentioned above, massive protostars start burning hydrogen while they are still embedded and accreting. The vast amounts of energy released by this nuclear fusion process result in much higher luminosities than a low-mass protostar can ever produce. This, in turn, results in extremely high radiation pressures that can even rival the gravitational pull, effectively stopping accretion in spherical symmetry. The point when this happens is given by the generalized Eddington luminosity

$$L_{\mathrm{Edd}} = \frac{4\pi\, G\, M_\star\, c}{\kappa_{\mathrm{dust}}}\,, \tag{1.6}$$

where κ_{dust} denotes the dust opacity. It is reached for a protostar of $\simeq 10\ M_\odot$, immediately posing the question how stars of higher masses can form, as such stars are frequently observed. This problem was solved by Nakano [1989] and Kuiper et al. [2010], by realizing that accretion disks provide an optically thin channel along the rotational axis, where radiation can escape, while accretion through the dense accretion disk cannot be stopped by radiation pressure of this magnitude.
In competitive accretion and coalescence [Bonnell et al., 2001], massive stars are thought to form in the centers of star-forming clusters, while low-mass stars predominantly form in their outer regions. The idea is that all initial cores are of relatively similar mass, but deep inside the gravitational well of the cluster, higher ambient gas densities are present due to the global collapse of the star forming clump. These higher densities then enable the forming protostars in the center to accrete more mass via Bondi-Hoyle accretion than the protostars in the outer regions of the cluster. In addition, the centers of the cluster then contain a high density of protostars that may even be able to merge and form higher-mass stars.
A major difference between the core accretion and the competitive accretion scenario is the prediction of smaller accretion rates in competitive accretion and, while disk mediated accretion plays a role in both models, competitive accretion predicts smaller size disks with varying orientations in the cluster. Massive star formation could also be a hybrid of both models or they could develop under different circumstances. So while our own simulations start from a massive prestellar core, as predicted by the core accretion model, the formation processes of disks and outflows work similarly in both models and, therefore, our results are not strictly bound to one scenario or the other.
Problems like massive star formation are much too complex to be solved analytically and crude approximations are unable to capture all the involved physical aspects to a satisfying degree. Therefore, numerical hydrodynamics provides a very insightful way to approach them

and we give a basic introduction to it in the next section.

1.2 Numerical fluid dynamics

Hydrodynamics is governed by conservation laws that constitute a system of hyperbolic partial differential equations (PDE) that have to be solved to evolve a system in time. These conservation equations are the continuity equation

$$\frac{\partial}{\partial t}\rho + \nabla \cdot (\rho \vec{v}) = 0\,, \tag{1.7}$$

with the fluid velocity $\vec{v}$, the momentum conservation equation

$$\frac{\partial}{\partial t}(\rho \vec{v}) + \nabla \cdot (\rho \vec{v}\vec{v}) + \nabla p = F_{\text{ext}}\,, \tag{1.8}$$

where p denotes the pressure and F_{ext} constitutes all the external forces that are to be considered, e.g. the effect of the gravitational potential V_{grav}, $F_{\text{g}} = -\rho \nabla V_{\text{grav}}$ could be added here, and the equation of energy conservation

$$\frac{\partial}{\partial t}(\rho \epsilon) + \nabla \cdot (\,(\rho \epsilon + p)\vec{v}) = 0\,, \tag{1.9}$$

with the total internal specific energy ϵ.
In integrating other forces into the momentum equation, it is worth noting that the use of a source term, as it was done for gravity, is not always sufficient. One example for such a force is viscosity. Viscosity is described by the Navier-Stokes equation, where we arrive at by adding $\nabla \cdot \sigma_{\text{visc}}$, with the viscous stress tensor σ_{visc}, to the left-hand side of the momentum equation. Here, the importance of viscosity can be judged by examining the Reynolds number

$$Re = \frac{\rho \bar{v} \bar{l}}{\eta_{\text{visc}}}\,, \tag{1.10}$$

with typical length scales $\bar{l}$, typical velocities $\bar{v}$, and the coefficient of shear viscosity η_{visc}. A flow with $Re \gg 1$ is rather inviscid and tends to be turbulent, and a flow with $Re \ll 1$ is viscous and mostly laminar. Turbulent flows have a range of scales, as the characteristic length and velocity scales vary. As a result, small-scale turbulence can itself act as a form of viscosity, and can be used in a larger scale simulation to mimic turbulence on smaller scales.
Using the Lagrangian, or comoving derivative

$$\frac{D}{Dt} = \frac{\partial}{\partial t} + \vec{v} \cdot \nabla \tag{1.11}$$

equations (1.7), (1.8), and (1.9) can be cast in the Lagrange form, effecitvely transforming them into a frame of reference moving with the particles

$$\frac{D}{Dt}\rho = \quad -\rho \nabla \cdot v \tag{1.12}$$

$$\frac{D}{Dt}\vec{v} = \quad \frac{\nabla p}{\rho} \tag{1.13}$$

$$\frac{D}{Dt}\epsilon = \quad -\frac{p}{\rho}\nabla \cdot \vec{v}\,. \tag{1.14}$$

To close this system of equations, one needs an additional equation connecting density and pressure, which is the equation of state. Since astrophysics often deals with very low densities and comparatively warm gas, a good approximation is the ideal equation of state

$$p = \frac{\rho k T}{\mu} \,. \tag{1.15}$$

It is valid, as long as internal energy changes by radiation can be neglected or it is coupled with radiative transfer to produce a realistic internal energy budget. To relate the internal energy and pressure, the caloric equation of state

$$p = (\gamma - 1)\rho\epsilon \,, \tag{1.16}$$

with the adiabatic index $\gamma = \frac{f+2}{f}$ is used. Here γ depends on the internal degrees of freedom of a molecule. For a collapse simulation, where much of the converted potential energy is radiated away, instead of an ideal equation of state with a radiative transfer code, an isothermal equation of state is a useful approximation as well, as it effectively eliminates the energy conservation equation.
A system of conservation equations, such as the equations of hydrodynamics, can generally be written as

$$\frac{\partial \mathbf{Q}}{\partial t} + \nabla \cdot \mathbf{F}(\mathbf{Q}, x) = \mathbf{S}(\mathbf{Q}) \,. \tag{1.17}$$

Here, the hydrodynamic quantities are combined into a vector $\mathbf{Q}$ and, consequently, $\mathbf{F}(\mathbf{Q}, x) = \mathbf{Q}\,\mathbf{V}(x)$ is the flux of the quantity $\mathbf{Q}$ with velocities $\mathbf{V}(x)$. The (magneto)-hydrodynamics code PLUTO [Mignone et al., 2007], that we apply in our simulations, is a grid-based code that uses a Godunov-type scheme to integrate the system in time, thereby solving Eqn. (1.17). Grid-based algorithms divide the system in cells, and a state of the system at any given time is given by the values of all the hydrodynamic quantities in each cell. Similarly, time is divided into discrete intervals. In a Godunov scheme, the system can be advanced from one timestep to the next by solving an initial value problem for each cell. Each cell interface constitutes a Riemann problem, where neighboring cells have constant, but different values for their hydrodynamic variables, whereby there is a jump at the interface. In such a problem, one has to advect each quantity according to (1.17). To solve this system analytically, one would have to diagonalize the Jacobian $\frac{\partial F}{\partial Q}$ and then solve the scalar PDEs that follow, resulting in a self-similar solutions to the Riemann problem. However, due to the strong non-linearity of the equations this is a rather complicated and numerically costly problem, and, as a result, approximate Riemann solvers are used. These approximate Riemann solvers allow us to construct the fluxes over the interfaces of neighboring cells, which is what we need to advance the state in time. Notably, it is crucial to restrict the timestep of the numerical scheme such that the different solutions from opposing cell interfaces do not traverse the full length of a cell. Therefore, as Courant et al. [1928] analyzed, the highest-velocity characteristic constrains the maximal timestep.
Numerical schemes like these can not only capture pure hydrodynamics but can also be extended to include magnetic fields. The basis of this is magneto-hydrodynamics which is introduced in the following section.

1.3 Magneto-hydrodynamic effects

In this chapter, we give a short introduction to MHD, with a focus on the most important magneto-hydrodynamic effects during core-collapse. First, the basics of *ideal* MHD are presented, followed by its influences on the accretion disk, non-ideal effects, and finally, magneto-centrifugal and magnetic pressure-driven launching mechanisms, where we also stress the distinction between them. It is in no way intended to be comprehensive, rather it aims to give the reader an idea of the basic concepts. For a more detailed review we recommend Spruit [2013].

1.3.1 Introduction to ideal magneto-hydrodynamics

Here, we give a short introduction to the most important aspects of ideal MHD, for the problem we wish to solve. As the name suggests, magneto-hydrodynamics is an extension of hydrodynamics that includes magnetic fields. In fact, it combines the conservation laws that govern fluid motions, equations (1.7), (1.8), and (1.9) with electric and magnetic fields, governed by Maxwell's equations (ignoring dielectric properties of the fluid):

$$4\pi\vec{j} + \frac{\partial\vec{E}}{\partial t} = c\nabla\times\vec{B} \tag{1.18}$$

$$\frac{\partial\vec{B}}{\partial t} = -c\nabla\times\vec{E} \tag{1.19}$$

$$\nabla\cdot E = 4\pi\sigma \tag{1.20}$$

$$\nabla\cdot B = 0\,, \tag{1.21}$$

with the electric current $\vec{j}$, the electric field $\vec{E}$ the magnetic field $\vec{B}$, and the charge density σ. The first assumption in magneto-hydrodynamics is that the gas is highly ionized and that on the temporal and spatial scales that we consider, we can assume infinite fluid conductivity. This assumption has the consequence that the electric field of a moving particle vanishes and only the magnetic field remains relevant for its movement. Plugging this information into Maxwell's equations leads to the central equation of (ideal) MHD

$$\frac{\partial\vec{B}}{\partial t} = \nabla\times(\vec{v}\times\vec{B})\,, \tag{1.22}$$

the induction equation. Another consequence of this approximation is that electric currents lose their significance and only remain in the equations as the curl of the magnetic field $\vec{j} = \frac{c}{4\pi}\nabla\times\vec{B}$. In practice, this means that diffusive effects for $\vec{B}$ are not considered in the equations of magneto-hydrodynamics [6]. This modified induction equation has important consequences for electromagnetic forces in fluids as well. The resulting Lorentz force F_L is given by

$$F_\mathrm{L} = \frac{1}{4\pi}(\nabla\times\vec{B})\times\vec{B}\,. \tag{1.23}$$

[6] Using computer simulations, though we have to discretize these formulae. This means that our simulation cannot follow these equations perfectly and, therefore, there is always a degree of numerical diffusivity even in the most modern and accurate solver algorithms.

We can combine these two equations with the continuity equation (1.7) to get a simple instructive picture of how fluids coupled with magnetic field behave.
First, we can determine the movement of particles without the knowledge of any other quantities appearing in Maxwell's equations than the magnetic field $\vec{B}$. Also, inverting the sign of $\vec{B}$ in the induction equation and in the Lorentz force leaves both equations unchanged. This means that in ideal MHD, the sign of the magnetic field is of no relevance. Additionally, we note that the Lorentz force has only a component perpendicular to the magnetic field.
A second interesting observation is that the induction equation and the continuity equation both describe how a quantity changes in time depending on the velocity and some derivation of said quantity. To see their similarities more clearly, we follow Spruit [2013]'s remarks on the topic here. The divergence in the continuity equation (1.7) can be expanded to get

$$\frac{\partial \rho}{\partial t} = -\rho \nabla \cdot \vec{v} - \vec{v} \cdot \nabla \rho \,. \tag{1.24}$$

The first term describes contraction and expansion of the medium and the second term advection. Using vector identities and the solenoidarity of B, the induction equation can be expanded to a similar form

$$\frac{\partial \vec{B}}{\partial t} = -\vec{B} \nabla \cdot \vec{v} - (\vec{v} \cdot \nabla)\vec{B} + (\vec{B} \cdot \nabla)\vec{v} \,. \tag{1.25}$$

The first term again describes the effect of compression and expansion and the second term describes the effects of advection. The last term constitutes an effect unique to the magnetic field's behavior. Its meaning becomes more apparent when combining equations (1.24) and (1.25) into

$$\frac{d\vec{B}}{dt}\left(\frac{\vec{B}}{\rho}\right) = \left(\frac{\vec{B}}{\rho} \cdot \nabla\right)\vec{v} \,. \tag{1.26}$$

Accordingly, the last term describes how the ratio of magnetic flux to the mass density changes when the fluid velocity varies along a field line.
To get an intuitive understanding of MHD, we need a last ingredient: *Alfvén's theorem*. It states that fluid particles behave in ideal MHD as if they were tightly bound to the magnetic field lines. An intuitive derivation can e.g. be found in Spruit [2013, section 2.1]. Therefore, a good way to think of particles in MHD is as *beads on wires*, where the magnetic field lines represent the wires. Here an important thing to remember is that sometimes these wires can be quite rigid and strong, like a solid iron wire, and sometimes they hardly have any influence at all, more like weak rubber bands.
To see how exactly these wires influence the particles moving along them, it is useful to rewrite the Lorentz force:

$$F_{\mathrm{L}} = \frac{1}{4\pi}(\nabla \times \vec{B}) \times \vec{B} = -\frac{1}{8\pi}\nabla \vec{B}^2 + \frac{1}{4\pi}(\vec{B} \cdot \nabla)\vec{B} \,. \tag{1.27}$$

The resulting two separate terms are the *magnetic pressure* ($-\frac{1}{8\pi}\nabla \vec{B}^2$) and the *magnetic curvature force* ($\frac{1}{4\pi}(\vec{B} \cdot \nabla)\vec{B}$). This representation provides us with a more comprehensible picture of how magnetic forces in MHD act. The magnetic pressure is a term that exerts a force from high to low magnetic field strengths like thermal pressure exerts a force from high to low pressure regions. The curvature force can be further rewritten as $-\frac{1}{4\pi}\frac{B^2}{r_{\mathrm{c}}}\hat{\mathbf{r}}_{\mathrm{c}}$ with the

curvature radius r_c. It can be visualized as a force acting in direction of the curvature of a field line. This means it acts to straighten out the field line if it is bent. In collapse simulations, we can see both processes taking place at the same time, though one component usually dominates over the other. In the accretion disk, in which the magnetic field lines are usually pointing perpendicular to the disk's surface, the magnetic pressure is potentially the dominant component, whereas in magneto-centrifugal launching the curvature component is more pronounced. The jet collimation process and magnetic towers are good examples of both components working at the same time and on similar magnitudes(although not in the same direction, see the next section for more details).
Finally, since our simulations and analyses are kept in spherical coordinates, it is useful to express equation (1.23) in r- ϑ and φ coordinates, resulting in

$$F_{\mathrm{L}}^{r} = -\nabla B^2 + \nabla \cdot B_{\mathrm{r}}\vec{B} - \frac{B_\theta^2 + B_\phi^2}{r} \tag{1.28}$$

$$F_{L}^{\theta} = -\nabla B^2 + \nabla \cdot B_\theta\vec{B} + \frac{B_r B_\theta - \cot(\theta) B_\phi^2}{r} \tag{1.29}$$

$$F_{L}^{\phi} = -\nabla B^2 + \nabla \cdot B_\phi\vec{B} + \frac{B_r B_\phi + \cot(\theta) B_\theta B_\phi}{r}\,. \tag{1.30}$$

The Alfvén surface

Yet another important concept is the *Alfvén surface*. It is the surface around the central mass where the poloidal flow velocity and the poloidal component of the Alfvén velocity $\vec{v}_{\mathrm{A}}$

$$\vec{v}_{\mathrm{A}} = \frac{\vec{B}}{\sqrt{4\pi\,\rho}} \tag{1.31}$$

are equal[7]. There are several modes of magneto-acoustic waves and they travel with velocities between the sonic velocity and the Alfvén velocity. The Alfvén Mach Number $M_{\mathrm{A}} = \frac{v_{\mathrm{A}}}{v_{\mathrm{flow}}}$, which is the direct analog to the sonic Mach number, is an indicator for the magnetic energy compared to the kinetic energy. Therefore, the Alfvén surface divides magnetically dominated regions from inertia dominated regions.

The magneto-rotational instability and magnetic breaking

A consequence of magnetic forces are the *magneto-rotational instability* and *magnetic breaking*. Both terms are associated with the phenomenon that magnetic fields in accretion disks can effectively transport angular momentum outwards[8].
The principle idea is that the magnetic field lines couple particles rotating at different radii and, consequently, with different velocities. Due to this differential rotation, the magnetic field exerts a torque that accelerates the slower moving particles while decelerating the faster particles, potentially until they have the same angular velocity. When the field has a component parallel to the equatorial plane, i.e. the field lies relatively flat in the accretion disk,

[7] As the magnetic field is, in general, anisotropic, specific components of the Alfén velocity are often of higher importance than its absolute value. Correspondingly, the Alfén Mach number has a direction dependence as well.

[8] In this context we usually mean an effective transport outwards, though the process can work in both directions.

this coupling is between disk material at different radii. As the rotational velocities in an accretion disk reduce with radius, this leads to an acceleration of the particles at higher radii and a deceleration of particles at lower radii. Therefore, particles at lower radii lose momentum and move to even lower radii, while the opposite happens to particles at higher radii, i.e. they gain momentum and their orbital radius increases. This additional displacement amplifies the effect of acceleration and deceleration, consequently leading to a runaway process, called the magneto-rotational instability [Balbus and Hawley, 1991]. This effect eventually leads to a turbulent mixing of gas in the accretion disk, potentially on scales too small to resolve in simulations. The resulting turbulent viscosity can further increase angular momentum transport.
In magnetic breaking, the coupling is from the centrifugally supported accretion disk to particles in the envelope moving at slower angular velocities. The principle of angular momentum transport is the same; particles with higher velocity are decelerated and slow moving particles are accelerated, only now the slow moving particles reside at much higher radii than the fast moving particles. Here, angular momentum is directly transported outwards by the magnetic field and no turbulence is induced. In this way, the accretion disk is coupled by magnetic field lines to the whole envelope. This can, in ideal MHD, totally suppress the formation of a centrifugally supported disk (*magnetic breaking catastrophe*).

Non-ideal MHD

The assumption of perfect conductivity has significant caveats. For example, the magnetic breaking catastrophe could totally suppress the formation of a centrifugally supported disk. Also, there is a radiatively shielded region in the disk, usually referred to as the dead zone, where the assumption of perfect conductivity is more than questionable. To include non-ideal effects, the induction equation of ideal MHD has to be modified into

$$\frac{\partial \vec{B}}{\partial t} = \nabla \times \left(-\eta \nabla \times \vec{B} + (\vec{v} + \vec{v}_{\mathrm{H}} + \vec{v}_{\mathrm{AD}}) \times \vec{B} \right) . \tag{1.32}$$

The first term $-\eta \nabla \times \vec{B}$ describes *Ohmic dissipation* and is caused by collisions between electrons and neutrals. The second term $\vec{v}_{\mathrm{H}} = \vec{v}_{\mathrm{e}} - \vec{v}_{\mathrm{i}}$ expands the equation to consider different velocities for electrons $\vec{v}_{\mathrm{e}}$ and ions $\vec{v}_{\mathrm{i}}$. It is usually referred to as *Hall drift*. The last term $\vec{v}_{\mathrm{AD}} = \vec{v}_{\mathrm{i}} - \vec{v}$ describes collisions of ions and the neutral species and is called *ambipolar diffusion*. There is an ongoing discussion on the importance of these effects in various regimes that depend on the details of the chemical composition and the environment. However, most authors agree that non-ideal effects play an important role in the star-formation process. With the possibility of forming centrifugally supported disks, MHD can also lead to magneto-centrifugally launched jets, which are the topic of the next section.

1.3.2 Magneto-centrifugal launching

One of the launching mechanisms we are interested in was first described by Blandford and Payne [1982] in a self-similar axial symmetric model and was improved and extended during the following decades [e.g. Pelletier and Pudritz, 1992]. The idea is that magnetic field lines anchored in a fast rotating accretion disk accelerate particles at larger radii to super-Keplerian rotational velocities which are then accelerated outwards by the centrifugal force. The

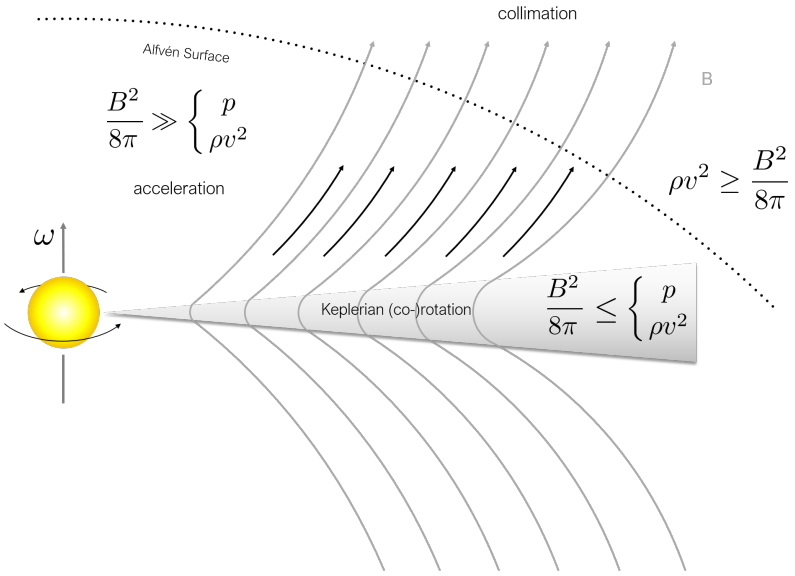

Figure 1.2: The principal of magneto-centrifugal launching from accretion disks.

launching principle is outlined in Fig. 1.2. Here, the situation presented is itself divided into three distinct regions: a dense accretion disk with high pressure and dominated by kinetic forces, a low-density region above the disk, but inside of the Alfvén surface, where magnetic forces are much stronger than thermal or kinetic forces, and an envelope outside the Alfvén surface, where kinetic forces are stronger than magnetic forces again.
It is instructive to follow a particle on the surface of a rotating disk through the three phases of a jet: launching, acceleration and collimation. In the initial launching process, the particle is supported from below by the thermal pressure of the disk and apart from that it is held in place by the gravitational pull of the protostar and the disk. As described above, in the ideal MHD approximation that Blandford also originally applied, all charged particles are tightly bound to the magnetic field lines. This means that, as long as the particle travels with the magnetic field lines or tangential to them, it is not affected by the Lorentz force. During the collapse, the magnetic field lines have assumed an hour-glass shape, as indicated by the grey lines in Fig. 1.2, and are anchored in the disk at a lower cylindrical radius than where they reach through the surface of the disk. Accordingly, the field line that goes through a particle on the surface rotates a bit faster than the particle would in centrifugal equilibrium. Since the particle considered is at the surface of the disk, magnetic forces are dominant and can increase its rotational velocity. Therefore, it becomes accelerated to super-Keplerian velocity and is centrifugally accelerated outwards. However, since the particle is tightly bound to the field line, it can only travel along it on its way outwards and, following the hour-glass shape of the field line, is eventually lifted upwards.
Here begins the second phase of the jet; the acceleration. Since it is still on its original field line and this field line moves it to even higher cylindrical radii, the centrifugal force steadily increases with increasing distance travelled and the particle's acceleration, in turn, rises further as well. This acceleration can only be slowed down when the kinetic energy of the particle reaches the local energy of the magnetic field (at the Alfvén surface). Then the particle's inertial forces also become comparable to the Lorentz force exerted by the magnetic field line and with increasing distance from the Alfvén surface, rather than accelerating the

particle further, the magnetic field line becomes bent through the inertial forces of the particle.

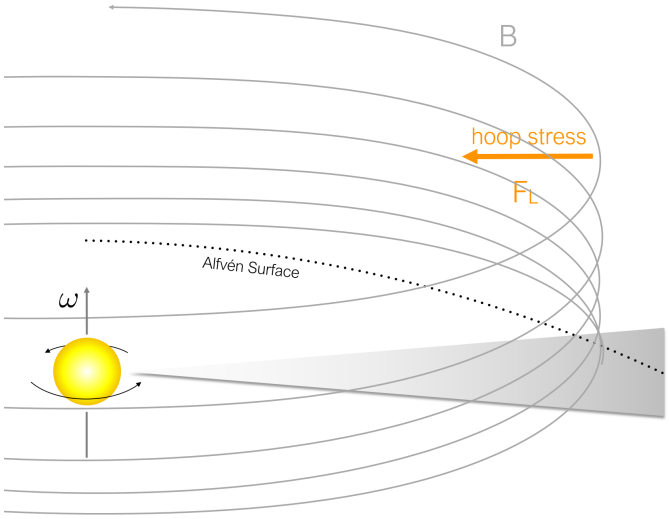

Figure 1.3: The principal of magnetic collimation of an outflow.

This introduces the last phase of a jet: the collimation. The bent magnetic field lines form a helical shape above the disk and fast particles are traveling along them. Since the magneto-hydrodynamic Lorentz forces have a component that points into a curved magnetic field topology (called magnetic curvature force, or in case of a collimating force *hoop-stress*), Lorentz forces and the centrifugal force can balance each other in the cylindrical radial direction, effectively confining the radius of the jet to a region close to the polar axis as visible in Fig. 1.3.
Such a magneto-centrifugal launching mechanism produces fast, and tightly collimated jets. However, outflows can also be launched by magnetic pressure. This possibility is the topic of the next section.

1.3.3 Magnetic towers

Magnetic tower flows [Lynden-Bell, 2003] work on different scales than the magneto-centrifugal launching discussed above. They develop outside of the Alfvén surface and above the disk. As mentioned, outside of the Alfvén surface, the inertial forces of the particles in the rotating disk are stronger than the magnetic forces and, therefore, the magnetic field lines are rather bent by the moving particles instead of governing their movement. This means that in the outer part of the disk the magnetic field assumes a helical topology not unlike the one assumed above the magneto-centrifugal launching region. After several rotations of the accretion disk, the magnetic field lines pile up like indicated in Fig. 1.4. This piling-up of magnetic field lines increases the magnetic field at low altitudes near the disk. Hence, a vertical gradient in the magnetic field strength develops and with it a gradient in the magnetic pressure $B^2/8\pi$. The corresponding magnetic energy-buildup can be released by uncoiling the helix, thereby accelerating particles on these helical field lines upwards. This results in a slower, but usually more massive and wider outflow compared to magneto-centrifugal launching. How both types of outflows develop during the complex collapse of a massive prestellar core is the scientific focus of the first project of this thesis, that is presented in the consequent chapter.

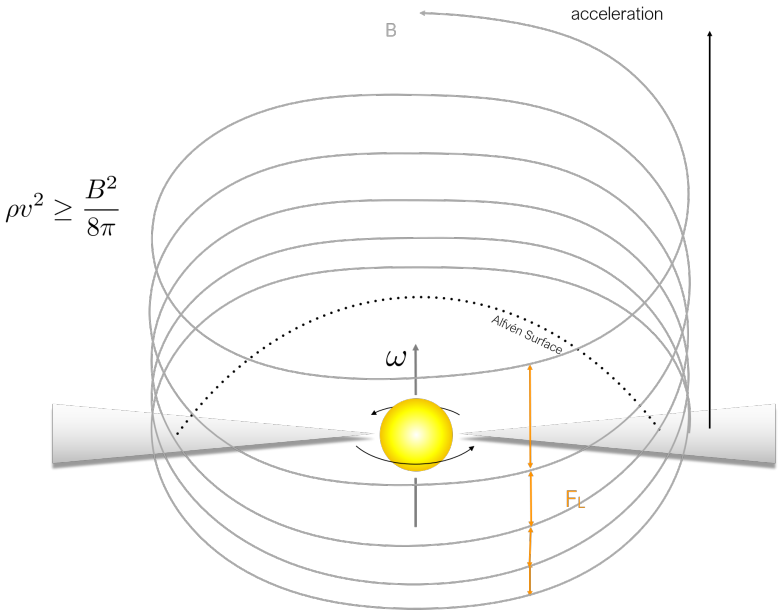

Figure 1.4: The working mechanism of magnetic towers.

Chapter 2

Magneto-hydrodynamic collapse of prestellar cores

As we have seen, massive star formation is a field with many research opportunities and there are many open questions waiting to be answered. The primary objectives of the first project presented in this chapter is to construct a comprehensive evolutionary picture of the collapse of a massive prestellar core. This means that we need to investigate computational conditions necessary to resolve (pseudo-) disk formation, as well as jets and outflows and identify possible caveats, enabling us to judge the reliability and quality of the physical processes simulated. Therefore, we can perform a detailed analysis of the physical processes involved in disk formation and outflow launching, as well as their time evolution, ultimately deriving quantities comparable with observations of real star-forming objects. The gained knowledge brings us then a little closer to answering important questions of massive star formation: Does high-mass star formation work like a scaled-up version of low-mass star formation? What are the differences? Do the dynamics of accretion and outflows follow the same principles? Why are outflows of massive stars usually less collimated than low-mass protostellar outflows?

2.1 Introduction

Many details of the formation process of massive stars are still poorly understood. This is mainly due to their large average distances from our solar system and due to the fact that their early evolutionary stages take place in opaque clouds of gas and dust barely penetrable by our current observational capabilities [e.g. Zinnecker and Yorke, 2007]. Still, we can observe a prominent feature of their evolutionary phase: their bright large-scale outflows [e.g. Frank et al., 2014].
While massive stars are rare, they have a much more significant impact on their surroundings than the large number of low-mass stars. During their whole lifetime, their feedback mechanisms influence not only their close neighborhood but their whole natal clusters. Therefore, they influence the IMF of their home clusters, provide heavy elements for later generations of stars and act as giant stellar laboratories (such as G023.01-00.41 [Sanna et al., 2014]).
The enormous radiative and mechanical luminosities of massive stars impact a vast range of scales and processes, such as the reionization of the universe, the evolution of galaxies, the

regulation of the interstellar medium, the formation of star clusters, and even the formation of planets around stars in such clusters.
The knowledge gained through the study of low-mass stars possibly provides important insights into massive star formation as well, although it is still a matter of debate which aspects of their evolution appear similarly in massive stars. Some aspects of star formation should theoretically work similarly, independent of scale. These processes are called scale invariant. Many theoretical and numerical works, therefore, use abstract units that can be rescaled to be applicable to different objects and phenomena. With respect to the problem at hand, the question arises if massive star formation as a whole just behaves as an upscaled version of its low mass counterpart (i.e. they behave scale-invariant) or if there are entirely different phenomena in both mass regimes (i.e. not scale invariant processes). Depending on the number of simulated physical processes, we can expect some simulations to show scale invariant behaviour. From other physical processes, we know that they behave very differently in low and high-mass star formation. An example for a scale invariant process in star formation are the high luminosities coming from a massive protostar compared to a low-mass protostar.
Although, we study outflows within a collapsing cloud core here, i.e. including the non-scale invariant self-gravity of the gas, the gravitational potential of the launching and collimation region is dominated by the central star, in which case the MHD equations are to a major degree invariant w.r.t. the gas density. The aspects of MHD that govern the launching and collimation of outflows are self-similar. That means they only depend on the ratios between different variables and are, therefore, of the same form, regardless if the resulting outflows are launched from a supermassive black hole or from a low-mass protostar[1]. Even in this case, however, the environmental conditions can be very different and result in different initial conditions, as in the case for low- and high-mass star formation.
To form massive stars, an equally massive mass reservoir is needed, which is then dominated by gravity and, depending on the initial mass-to-flux ratios[2], the magnetic field. Thermal pressure, on the other hand, is (in contrast to low-mass star formation) expected to be negligible. For massive cores, feedback by radiation pressure, ionization, and line-driving potentially contribute immensely to the evolution, while for low-mass cores, these effects are not present or relevant at all. While in both cases the early evolution takes place in deeply embedded regions, in low-mass cores, the envelope is to a large degree depleted before their radiation becomes a relevant factor for their continuing evolution. This is not the case for massive cores where the strong gravitational pull quickly accumulates mass, and with it potential energy that is converted into thermal and radiative energy, accompanied by high accretion luminosities. When the protostar finally starts its fusion processes, its feedback mechanisms eventually stop accretion in the non-shielded polar regions completely, launch winds, etc. All these processes influence the evolution of the collapse immensely while a significant part of the envelope is still present and the (proto)star is still not observationally accessible.
Outflows potentially have different launching principles and work on different spatial and

[1]However, the first case will produce a relativistic jets and in the latter case relativistic effects can be safely ignored.

[2]This is usually given in units of the critical mass-to-flux ratio (Eqn. (2.4)). A mass-to-flux ratio of 1, in principle, means that the Lorentz force can balance gravity in the initial cloud and so the core is sub-critical and will not collapse.

temporal scales. There are numerous known ways to launch outflows: they can be accelerated by line driving [Kee et al., 2016, Vaidya et al., 2011], by magneto-centrifugal acceleration at the interface of the stellar magnetosphere with the disk [X-Winds Shu et al., 1994], by magneto-centrifugal processes from the centrifugally supported part of the disk [Blandford and Payne, 1982], by magnetic pressure alone [Lynden-Bell, 2003], by continuum-radiation pressure [e.g. Yorke and Sonnhalter, 2002, Kuiper et al., 2010, 2011], and on the largest scales by expanding HII regions [e.g. Kuiper and Hosokawa, 2018]. A comprehensive overview of the state-of-the-art of modeling MHD jets in massive star formation is given in Section 2.2.2. In this chapter, we are focussed on the very early evolutionary stages of massive star formation and are interested mainly in magneto-hydrodynamic launching processes without contributions by radiation. That means we focus on magneto-centrifugal launching from rotating accretion disks and winds driven by magnetic pressure. In the early stages that we simulate, processes like line-driving, radiation pressure, and ionization are considered to be negligible, though in principle they may become important during the temporal span of our simulations. There are established analytic models describing these types of outflows: the fast jet that is launched from the rapidly rotating disk inside of the Alfvén-radius[3] described by Blandford and Payne [1982] and a slower, more massive wind launched outside the Alfvén-surface where the magnetic field is wound up by differential rotation, producing a so-called magnetic tower flow as described by Lynden-Bell [2003].
Beside the physical launching process itself, its influence on the evolution of the system composed of star, accretion disk, and the envelope is important for our understanding of star formation. Outflows could alleviate another important issue: as Mestel [1965] first realized, prestellar clouds have a much higher average angular momentum than the final stars. Therefore, there must be an efficient way to remove excess angular momentum during the evolutionary process. Magnetic breaking and magnetically induced turbulence due to the magneto-rotational instability can potentially provide this mechanism [Shu et al., 1994, Lovelace et al., 1995]. Magnetically driven winds can remove a large portion of angular momentum without removing too much mass, due the strong coupling between particles in the jet to the rest of the accretion disk through magnetic fields. This also means that jets and outflows inject (angular) momentum in their environment and are an important feedback effect that influences not only a single star but a whole star-forming region.
To give an overview on the current chapter: in section 2.2, we summarize important observations of massive protostars and the state-of-the-art of MHD modeling of jets and outflows from massive protostars (including the cloud collapse). In section 2.3, we describe the methods and parameters used in our simulation. In section 2.4, we then give an overview on the temporal evolution of our collapse simulations. In sections 2.5 and 2.6, we analyze the convergence properties of our numerical setup with respect to the resolution and the sink cell size and discuss caveats. In section 2.7, we describe our physical findings in detail, explaining disk formation and outflow mechanisms, and in section 2.8, we summarize our results.

[3]The Alfvén-radius is the radius at which magneto-acoustic waves propagate as fast as the material flows in the polar direction. It is a fancy way to differentiate between the regions where the material flow governs the magnetic field topology and the region where the magnetic field topology governs the flow direction. Note the keyword *polar direction*; this means here that, while in the toroidal direction the magnetic field lines are dragged along with the flow, in the polar direction the rotating magnetic field lines move material around and can, therefore, also accelerate material. See section 1.3 for more details on the principles of the launching process.

2.2 Previous studies

In the following, we give a brief overview on previous works on jets and outflows in massive star formation. We start with observed properties and continue with a comprehensive review on computational studies that include magnetic fields. Thereby, we highlight the results in terms of the disk formation process, the launching of outflows, and their characteristic properties, such as disk mass, radius, and outflow momenta.

2.2.1 Observed properties of jets and wide-angle outflows

A very comprehensive review is given in Frank et al. [2014]. Here, we just want to mention a few important results that can be easily compared with simulations.
While direct observation of the outflow launching engine is not yet possible, there are several other quantities that can be derived from larger scale observations and are, therefore, accessible to us. One of those quantities is the mass outflow rate for which all necessary components can be derived from other directly measurable quantities. This means that typical outflow rates from massive prestellar cores are well known, as well as the accretion-to-outflow-efficiency. Classical T-Tauri-Stars [Cabrit et al., 2007, Agra-Amboage et al., 2009] as well as Herbig Ae/Be-Stars [Ellerbroek et al., 2013] have accretion-to-outflow-rates of about 10%. It is not entirely clear if this ratio also holds for more massive O/B-stars but if these massive stars have similar accretion and ejection mechanisms they are expected to have similar rates. This ratio is also predicted in the seminal work by Blandford and Payne [1982] on self-similar magneto-centrifugal jets, though they actually predict a dependence on the magnetic lever arm and one arrives at this 10% ratio only for the very idealized conditions that they assume in their model.
Directly related to the accretion-to-outflow-efficiency is the issue that the observed star formation efficiency is only on the order of $\simeq 0.3$ [Offner et al., 2014, Padoan et al., 2014] which means that there must be a way to remove mass from the collapsing cloud core or halt it for extended time scales (longer than the evolutionary timescale of the forming star). A possible resolution to this issue is, as several authors pointed out, that the observed accretion rates are far too low to acquire the masses observed in the IMF [Evans et al., 2009, Caratti o Garatti et al., 2012] which means that accretion (and outflows) are thought to be episodic events. Recent simulations and observations [Caratti o Garatti et al., 2016, Stecklum et al., 2017] of accretion disks in massive star formation provide ample evidence that these episodes are triggered by the accretion of gaseous clumps created by disk fragmentation [Meyer et al., 2017], similar to FU Orionis objects in lower mass star formation.
A very remarkable recent observation by McLeod et al. [2018] observed a massive young stellar object in the Large Magellanic Cloud (LMC), that shows signs of such a highly collimated fast magneto-centrifugal jet that we describe here. In its surroundings, nearby O-stars seem to have dispersed the envelope by alleviated ionization feedback enabled by the low dust content of the LMC, revealing for the first time the inner workings of a protostellar outflow of a massive protostar. They report jet velocities of $300 - 400$ km/s, mass outflow rates of 2.9×10^{-6} $M_\odot$ yr^{-1}, and derive outflow lifetimes of $(28 - 37)$ kyr from the extent of the jet. In the next section, we summarize the results of relevant numerical studies.

2.2.2 Magneto-hydrodynamic simulations in high-mass star formation

There have been several studies on outflows of low mass stars [Tomisaka, 2002, Hennebelle and Fromang, 2008, Machida et al., 2008, Price, 2012, Machida and Hosokawa, 2013, Tomida et al., 2013, Machida and Hosokawa, 2013, Bate et al., 2014, Tomida et al., 2015], though simulations of massive stars and especially collapse simulations of massive prestellar cores are much rarer. In terms of massive cloud-collapse simulations, we want to mention an early simulation by Banerjee and Pudritz [2007] who start their simulation with a massive Bonnor-Ebert-sphere setup and compare three simulations with each other: an isothermal collapse, a collapse with radiative cooling, and a magnetized collapse with radiative cooling. Their study is relevant here, because they demonstrated that only a simulation including a magnetic field could self-consistently produce outflows. They also argue, though they do not simulate this, that these outflows could help to relieve the radiation-pressure-problem of massive star formation by channeling radiation out of their outflow-cavities. Also, given the computational resources of that time, they were only able to resolve a magnetic tower flow, and did not see a sign of a magneto-centrifugal jet.
Generally, convergence considerations are rare, or at least they are not mentioned. There are three studies on collapse simulations that compare results for different resolutions: Hennebelle et al. [2011] and Seifried et al. [2011, 2012]. Hennebelle et al. [2011] simulated a massive (100 $M_\odot$) cloud collapse in ideal MHD. They ran their adaptive mesh refinement (AMR)-simulations with a maximal resolution of 2 au and compared these to a run with a lower resolution, corresponding to a maximal refinement of 8 au. They focus their attention and discussion on the influences of the magnetic field on cloud evolution and find episodic slow-velocity outflows.
The series of simulations conducted in Seifried et al. [2011] and Seifried et al. [2012] have similar initial conditions to our own simulations but have a different computational focus. They use a three-dimensional grid and do not include non-ideal MHD-effects. Both papers describe the collapse of 100 $M_\odot$ cores with variable rotational and magnetic energy densities using AMR with a maximal resolution of 4.7 au. Thematically, Seifried et al. [2011] focus on accretion rates and centrifugally supported disk formation, finding that strong magnetic fields can suppress centrifugally supported disk formation for simulations with mass-to-flux ratios of < 10. Seifried et al. [2012] analyze in detail the conditions for magneto-centrifugal jet-launching by Blandford and Payne [1982] and develop and test a criterion to decide whether the jet is launched centrifugally or magnetically. They find that both processes are present, and that the central part of the outflow is primarily centrifugally launched and the outer outflow is launched to a larger degree by magnetic forces. Moreover, they find that with high magnetic fields the collimation of their outflows is rather poor due to the strongly sub-Keplerian disk rotation that does not build up a strong toroidal magnetic field necessary to collimate the jet.
Machida et al. [2014] give a comprehensive overview comparing different collapse simulations w.r.t. sink cell size, resolution, and initial conditions for low and massive prestellar clouds. They tried to reproduce the simulations by several other authors, with the single study involving massive stars included in their reproduction being the one by Seifried et al. [2011, 2012]. Interesting is that they repeated Seifried et al. [2011]'s simulations in a nested grid of dimension $64 \times 64 \times 32$ with equatorial symmetry, resulting in higher resolutions of up to 0.6 au. The most remarkable finding of their study is that the outflow properties are greatly

affected by sink treatment and the size of the sink cell in all of their simulations.
Other authors focus on the issue of fragmentation without analyzing outflows in detail. Fragmentation in this context means that the Jeans mass can be reached at several small independent regions. This, in turn, leads to the fragmentation of a single massive prestellar core into several small gravitationally bound objects, effectively suppressing the formation of a single more massive entity. The interaction of these fragments then also hinders the formation of stable and fast outflows, as shown in Commerçon et al. [2011] and Hennebelle et al. [2011]. Both groups conduct MHD-AMR-collapse-simulations of 100 $M_\odot$ cores with a maximal resolution of 2 au. Hennebelle et al. [2011] focus on the effects of magnetic fields in massive star formation and fragmentation for different mass-to-flux ratios ($\bar{\mu} = 120, 5, 2$) with a barotropic equation of state. Due to the fragmentation, they were only able to find slow episodic non-bipolar outflows with velocities with an average $\simeq 3 - 4$ km/s and maximal velocities of 40 km/s. In contrast, Commerçon et al. [2011] focus on the suppression of fragmentation due to interplay of magnetic and radiative forces. They mention that in a simulation with $\bar{\mu} = 2$, they form only a single fragment with an outflow velocity of 2 km/s.
Several other authors are mostly interested in the large-scale environment and the effects of feedback of massive star formation. The simulations by Wang et al. [2010] and Myers et al. [2014] simulate the collapse of massive clouds with RMHD but use observationally motivated subgrid-models to introduce outflows from their sink cells and do not self-consistently produce outflows. They use large-scale computational domains focusing on the influences of these outflows on the large-scale magnetic field structure, star cluster formation, and star formation rate, thereby deducing the CMF and IMF of whole clusters. Peters et al. [2011] are also focussed on the larger scales and simulate a 1000 $M_\odot$ with AMR-RMHD and compare simulations with and without magnetic fields to study the effect of magnetic fields. They are able to produce very low-velocity outflows self-consistently. They interpret their results to imply that large-scale low-velocity tower flows of massive cores are much weaker than expected from their low-mass counterparts and they reason that this is mainly due to fragmentation, though to our knowledge, this could also be an effect of their large, 98 au cell sizes (as stated above, they focus on larger scales). So their simulations do not resolve the launching region of the centrifugally launched fast jet component and even the lower-velocity tower flows could reach higher velocities if they were launched closer to the central mass.
A recent study that specifically discussed jets and outflows of massive protostars is Matsushita et al. [2017]. They show 3D nested grid simulations of massive prestellar cores with a fixed resolution but varying energy ratios using a barotropic equation of state. They follow the outflow for a few 10^4yr and focus on the mass ejection rate. They do include non-ideal MHD effects and use a nested grid approach with a fixed number of cells in each level of $64 \times 64 \times 32$ combined with equatorial symmetry. On the highest level, they achieve a cell size of just 0.8 au which can resolve the launching region quite well, though is nearly one order of magnitude lower than the resolution we reach in the launching region. Similar to our simulation, they use a sink cell with 1 au radius. The main finding is that a proportionality between accretion and outflow rates exists in their simulations and they conclude that low and high mass stars probably have a similar launching mechanism, which means that their outflows are launched by magneto-centrifugal and magnetic pressure driven mechanisms. While their simulations are relatively similar to ours, they do not discuss how their outflows are launched and accelerated. In particular, no distinction between a magneto-centrifugal and a magnetic tower flow are made in the interpretation of their results, although they state that

the outflow was driven by a magneto-centrifugal process. They focus on the relation of the resulting properties like outflow momentum, accretion rate etc. to physical input parameters such as initial cloud mass, magnetic field, angular velocity etc., while we concentrate on the physical launching mechanisms and how numerical parameters influence the evolution of the cloud core. Finally, they do not consider the effects of different resolutions or sink cell sizes. Studies that do consider resolution aspects are discussed in the subsequent section.

2.2.3 Convergence aspects

As already mentioned, only a few authors test their setups on convergence and even if they do, only Seifried et al. [2011] compare more than two resolutions. Therefore, it remains unclear if many of those simulations converge to a stable solution and which resolution is necessary. Seifried et al. [2011] repeated their simulations with a factor of 4 higher as well as lower resolution than their fiducial case. They compare the density and temperature profiles as well as the velocity in the midplane. In the higher-resolution runs they can resolve shock features in density and temperature to a better degree than in their low-resolution runs and they state that the vertical structure of the disk may not even be sufficiently resolved in their highest resolution. Also, their criterion for sink-particle creation is met more often for higher resolutions.
Additionally, they show the accretion rate of their sink particle for the first 2 kyr of their simulations. The simulation with the highest resolution clearly shows a significantly different behaviour compared to the lower resolution simulations. During the last 500 yr shown, a process seems to evolve, that is only resolved by the highest resolution. Also, there is no indication of a trend of convergence. During these latter 500 yr, the accretion rate in the highest resolved simulation lies in between the low- and the mid-resolution simulations and, on average, increases with time. Judging from this trend, we expect the average value of the accretion rates to diverge significantly for longer simulations and with it the mass in the sink. This underlines the strong dependence of the physical evolution of the system under investigation on numerical resolution. With their convergence study focussed on the disk structure, it is not clear if they meet the requirement to resolve the jet-launching region enough for a quantitative analysis of the outflow-properties. We also want to point out that they introduce a threshold for the minimal density of 1.78×10^{-12} g cm^{-3} in their simulations to limit the maximal velocity of magneto-acoustic waves in their computational domain, which in turn results in larger numerical timesteps. This together with their relatively low resolution could act as an effective magnetic dissipation which would then lead to an underestimation for the minimal mass-to-flux-ratio to build up centrifugally supported disks.
While Hennebelle et al. [2011] study convergence properties of their simulations by comparing a high and a low resolution run, they use two slightly different Riemann Solvers with different numerical diffusivities and they run the high-resolution simulation only for half the time they run the low-resolution simulation ($0.1 - 0.2$ free-fall times after the formation of the first protostar for the high resolution simulations, and $0.4 - 0.5$ free-fall times for the low-resolution run). They find significant differences between the two simulations and remark on caveats for the low resolution runs.
In comparison, our simulations have very high resolutions with a minimal cell size of just 0.09 au and small sink cell radii of only 1.0 au. Simulations with this resolution have never been done before and enable us to analyze the details of disk formation and outflow launching

in detail. After we give an overview on the physical processes of our collapse simulations in Sec. 2.4, our detailed convergence studies in Sec. 2.5 and Sec. 2.6 show that many physical processes in such simulations are extremely resolution and sink cell size dependent. To this end, we compare the evolution of disk properties (disk radius, disk mass, and disk lifetime), outflow properties (linear and angular momenta, ejection-to-outflow ratios), as well as the protostellar mass and accretion rate for simulations with different resolutions ($\Delta x = 0.09$, $\Delta x = 0.17$, $\Delta x = 0.37$) and different sink cell sizes ($r_{\rm sink} = 1.0$ au, $r_{\rm sink} = 3.1$ au, $r_{\rm sink} = 10.9$ au, $r_{\rm sink} = 30.3$ au). Finally, in Sec. 2.7, we analyze the physical structure of the disk and outflow in detail, using the forces and magnetic field topology to produce a comprehensive physical picture of the processes shown. First, though, we introduce our numerical methods.

2.3 Methods

The basis of our simulations is the modular magneto-hydrodynamics code PLUTO [Mignone et al., 2007] combined with a self-gravity solver developed by Kuiper et al. [2010]. PLUTO is a free and open source code for the solution of mixed hyperbolic/parabolic systems of partial differential equations, primarily intended for (but not limited to) the use in astrophysical fluid dynamics using a finite volume or finite difference approach based on Godunov-type schemes. It natively includes modules for magneto-hydrodynamics and relativistic (magneto-) hydrodynamics.
We make use of its HLLD Riemann solver with linear interpolation and integrate by Runge-Kutta method of order 2. Since numerical schemes do not preserve the solenoidality of the magnetic field naturally, PLUTO includes several methods to ensure it. Here, we utilize PLUTO's state-of-the-art constrained transport algorithm to this end.
To close the system of equations, we chose an isothermal equation of state. PLUTO's modular nature allowed us to implement equations of state with different adiabatic indices that could also be varied depending on the position, time, and local variables to mimic the effects of radiative heating/cooling in a controlled way. While this approach might be useful in the future, it basically pre-determines a significant part of the simulation. Therefore, we conclude that an ideal equation of state combined with radiative transfer would be the *ultima ratio* w.r.t. a realistic outcome of our collapse simulation, as well as the only way to derive a realistic evolution for longer time spans. This would, on the other hand, vastly increase the number of physical processes and significantly aggravate the analysis of magneto-hydrodynamic effects we want to focus on. Therefore, an isothermal equation of state represents a solid choice for analyzing magneto-hydrodynamic effects in early phases of the collapse of massive prestellar cores and we will include radiative transfer in future studies.
PLUTO also supports the treatment of dissipative effects like viscosity, magnetic resistivity, and thermal conduction. In our simulations, we only need the former two. For the disk's shear viscosity, we adopt the prescription by Kuiper et al. [2010].
On the polar axis, we use axisymmetric and at the equator mirrorsymmetric boundaries that work perfectly with the constrained transport scheme of PLUTO. At the inner radial boundary, i.e. the sink cell, on the other hand, the situation is more difficult. Here, we experimented with various boundary conditions and with varying degrees of success. In the end, zero gradient boundary conditions were chosen at the inner radial boundary, as they are very

comprehensible and do not lead to problematic results. The outer radial boundary uses zero gradient boundaries as well but with the radial velocity constrained to positive, i.e. outflowing, velocities.
Our simulations include ohmic resistivity as a phenomenological model for the magnetic dissipation in the dead, dense, and radiatively shielded region of the disk, thereby enabling the formation of a centrifugally supported accretion disk that is not destroyed by magnetic breaking. We implement the resistivity model used by Machida et al. [2007] which is based on a numerical study by Nakano et al. [2002]. Nakano et al. [2002] investigated the different mechanisms of magnetic flux loss in molecular clouds by drift of dust grains. Machida et al. [2007]'s resulting ohmic resistivity is given by

$$\eta = \frac{740}{X_\mathrm{e}} \sqrt{\frac{T}{10\mathrm{K}}} \left[1 - \tanh \frac{n}{10^{15}\mathrm{cm}^{-3}}\right] \mathrm{cm}^2\mathrm{s}^{-1}\,, \tag{2.1}$$

with the ionization degree

$$X_\mathrm{e} = 5.7 \times 10^{-4} \left(\frac{n}{\mathrm{cm}^{-3}}\right)^{-1}\,. \tag{2.2}$$

We use the same equation at an isothermal temperature of 10 K. The dense dead zone in the accretion disk of the massive clouds cores that we simulate regularly reaches densities of $n_\mathrm{H} > 10^{12}$ cm^{-3}. This is according to Nakano et al. [2002], the regime where ohmic dissipation is the dominant flux-loss-mechanism. Three aspects of our numerical setup are discussed in more detail: the grid in Sec. 2.3.1, the initial conditions in Sec. 2.3.2, and the Alfén velocity limiter in Sec. 2.3.3.

2.3.1 Grid

We run our simulations on a two-dimensional spherical grid with equatorial- and axal symmetry. By stretching the grid in the radial direction logarithmically and tuning the number of cells in radial and polar direction accordingly, we generate a grid with cells of equal spatial extent in the radial and the polar direction that naturally reduces the cell size close to the origin. This increases the resolution of our simulations in the central region, where eventually the outflows launch and where the physical processes in the disk and outflow cavity require the most resolution. This simple but effective grid geometry has the highest dynamic range among all regular grid techniques utilized in previous studies of MHD jets in massive star formation. To achieve a similar dynamic range in a Cartesian AMR-simulation with 126 cells (corresponding to the highest number of cells we use in radial direction), one would need more than 13 levels of AMR refinement (in addition to the base resolution) and with it great computational resources. In our simulations, the entire computational grid reaches from the central sink cell radius, which is a parameter that we vary in our convergence study (correspondingly, r_sink = 0.1 au, 0.3 au, 1.0 au, 3.1 au, 10.9 au, 30.3 au), up to 0.1 pc.

2.3.2 Initial conditions

Initially, the cloud core has a radially symmetric density distribution $\rho \propto r^{-1.5}$ with the rotational axis and grid axes aligned along with the direction of the uniform magnetic field. Kinetic and thermal energies are chosen such that the core is supercritical, i.e. its gravitational pull is stronger than the forces stabilizing it and collapses immediately. The core rotates

initially with solid body rotation of a frequency of $3 \times 10^{-13} \mathrm{s}^{-1}$, corresponding to a total kinetic to gravitational energy ratio of 2%. The thermal energy is with a (isothermal) temperature of just 10 K negligible (thermal to gravitational energy fraction = 0.5%). Considering only gravity, the core would collapse with a free-fall time of

$$t_{\mathrm{ff}} = \frac{\pi}{2} \frac{r^{3/2}}{\sqrt{2GM}} \simeq 52 \text{ kyr} \,. \tag{2.3}$$

The mass-to-flux ratio $\bar{\mu}$ in units of the critical mass-to-flux-ratio [Nakano, 1988] is

$$\bar{\mu} = \frac{M_{\mathrm{core}}}{\Phi_{\mathrm{core}}} \Bigg/ \left(\frac{M}{\Phi}\right)_{\mathrm{crit}} = \frac{M_{\mathrm{core}}}{\int B_z dA} \Bigg/ \frac{1}{2\pi \sqrt{G}} \,, \tag{2.4}$$

with the total core mass M_{core}, the total magnetic flux Φ_{core}, and the area A is set to 20.

2.3.3 Alfvén limiter

The maximal time step of hydrodynamic simulations following explicit Godunov-type schemes like ours is, depending on the local cell size, limited by the highest signal velocity anywhere on the grid. In our case, this velocity is either the maximal velocity of material streams or magneto-acoustic waves as well as ordinary sound waves. The velocity of magneto-acoustic waves is limited by the sound speed or the Alfvén velocity (whichever is higher).
The Alfvén velocity gets particularly high in environments with high magnetic field strengths and low densities. In collapse simulations like ours, a situation like this occurs naturally in the jet-launching region. This is because material falling in from above can be accreted onto the star traveling along the magnetic field close to the pole without any resistance by magnetic or centrifugal forces. The magnetic field, on the other hand, is constantly accreted through the infalling material in the equatorial plane. It does not vanish into the sink cell but is conserved inside the computational domain due to the solenoidality of the magnetic field. Therefore, the magnetic field piles up in the center while the bulk mass above the disk is accreted by the protostar. This is even amplified when an outflow is launched above the star, as the outflow cavity reduces the density even further. These evolutionary processes lead to an increase of magnetic field and decrease of density. Therefore, the Alfvén velocity will increase quickly. As a result, the time step of our simulation decreases to what is effectively a halt.
Therefore, we chose to increase the density in this region to limit the maximal Alfvén velocity to 700 km/s. We tested various velocity limits and 700 km/s constitutes a trade-off between realistic magnetic field evolution and reasonable time steps. We monitor the mass that we create in this way throughout the whole simulation and in all simulations, it remains below 6% of the initial mass until one free-fall-time. We continue with an overview on the various processes that occur during the collapse of a massive prestellar core in the next section.

2.4 Temporal evolution

In the following, we describe the most important evolutionary phases of the system in chronological order. The timescales refer to the time from the onset of cloud collapse and to

the simulation with a sink cell size of 1 au and with a resolution of 126×20 grid cells. Qualitatively similar results also appear for lower resolved simulations and larger sink cell sizes, only shifted in time. Differences between these runs are discussed in 2.5 and 2.6, respectively.
In the first 4 kyr, the gravitationally super-critical cloud core collapses under its own gravity and neither magnetic nor centrifugal forces reach comparable magnitudes. The infalling material flows with super-Alfvénic velocities down to the equatorial plane. The comparatively low magnetic field strength has nearly no influence on the flow in this epoch and the magnetic field topology is determined primarily by the gas flow. As a result, the magnetic field gets dragged into the center along with the gas, yielding the well-known hour-glass like shape (Fig. 2.1). While most of the material of the original envelope is still infalling from all directions,

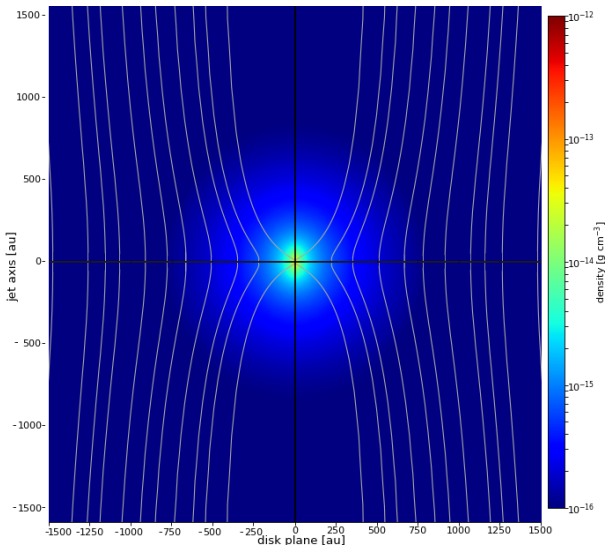

Figure 2.1: Density distribution near the protostar after 3.5 kyr (0.5 kyr previous to jet launching), overlaid with the hour-glass shaped magnetic field lines.

angular momentum conservation leads to the formation of a notably rotationally flattened envelope and hereupon a disk-like structure that is not yet centrifugally or magnetically supported.
The magneto-centrifugal jet launches at $\simeq$ 4 kyr. It immediately clears out an outflow cavity with two orders of magnitude lower density than the neighboring infalling envelope. Directly after the initial jet launching, magnetic and centrifugal forces can withstand gravity in the midplane for the first time and the accretion disk grows continuously outwards. The increasing magnetic field strength and the strong ram pressure of the outflow hinder accretion within the polar outflow cavity. At the same time, there is still a flow of material falling downwards along the cavity wall. This congestion leads to an increased density above the disk that is threaded and supported by the magnetic field (Fig. 2.2).
At $\simeq$ 8 kyr, a separate launching/acceleration region becomes distinguishable from the previously present magneto-centrifugal jet. This acceleration takes place at larger radii and higher altitudes above the disk (compared to the fast initial jet) in a region of relatively high density (compared to the outflow cavity) and high toroidal magnetic field strength. Therefore, it can be identified as a magnetic tower flow. The tower flow's acceleration in this direction is not as strong as the acceleration of the magneto-centrifugal component and results in lower

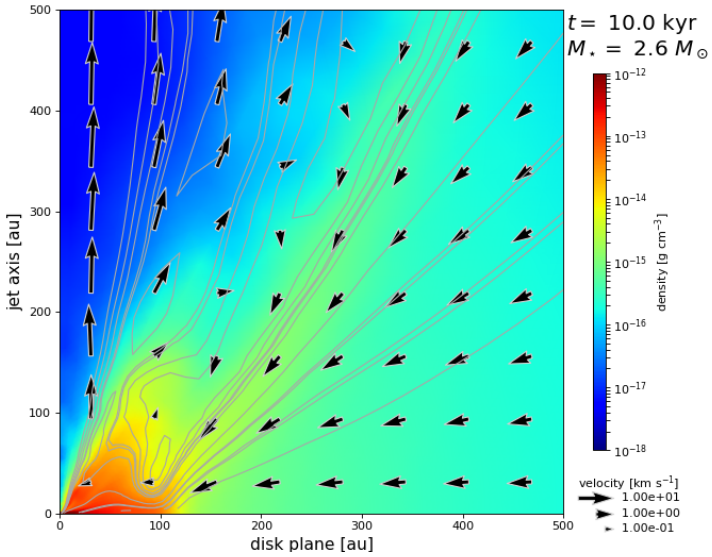

Figure 2.2: Increased density above the disk. Due to angular momentum conservation and magnetic forces, infalling gas cannot be accreted into the protostar as fast as it arrives from the outer envelope. The change from super- to sub-Alfvénic infall induced the distorted magnetic field morphology.

flow velocities. The magneto-centrifugal jet reaches outflow velocities of several 100 km/s, while typical outflow velocities of the tower flow only reach a few km/s.
From this point in time on, the accretion disk grows in size, the density contrast between the disk and its dense atmosphere above the disk continuously increases and the outflow is continuously active. The launching region of the fast magneto-centrifugal jet expands towards higher altitudes and the launching region of the slower tower flow towards higher altitudes and to larger disk radii (See Sec. 2.7 for details).
When the simulation reaches one free-fall time, the mass reservoir above the protostar gets depleted and with it, the supply of angular momentum for the disk ceases as well. Then the only channel left for accretion is through the accretion disk. As a result, the fast magneto-centrifugal jet component vanishes. When infall ceases, both the reservoir of material for star formation and its associated ram pressure are removed. Without this pressure from above, the magnetic pressure gradient becomes stronger than gravity up to much larger radii, and, as a result, the launching region of the slow tower flow vastly expands. Within the next 20 kyr, it encompasses 10000 au and continues to grow to the full extent of our simulated region of 0.1 pc before the end of the simulation at 100 kyr. As all processes described here are potentially depending on the details of our numerical setup, our convergence considerations are presented in the subsequent two sections.

2.5 Convergence properties for different resolutions

In this section, we present and discuss the convergence properties of the simulations performed. Specifically, we check here in detail if the simulation's results change with resolution and/or the size of the central sink cell. Such numerical convergence tests are crucial to extract robust scientific results from numerical simulations in general. Only parameters and results which show a proper convergence behavior represent meaningful outcomes of such a

study. This section is subdivided into the physical objects that are analyzed, since different physical effects potentially have different resolution requirements. First, we discuss the influences of different resolutions for the evolution of the accretion disk. Then, we continue with the outflows as well as the protostar. In the sections following that, a similar analysis is carried out for different sink cell sizes.
For the resolution analysis, we performed three simulations with 126×20 cells, 64×10 cells, and 32×5 cells in the radial, correspondingly polar direction. All physical and numerical parameters are kept exactly the same for the three simulations. Most importantly, their grid always stretches from 1.0 au to 20626.5 au = 0.1 pc. The given cell numbers translate to the following resolutions Δx in the innermost regions close to the protostar and where the jet is launched:

cell number	Δx [au]
126×20	0.09
64×10	0.17
32×5	0.37

Table 2.1: Cell numbers and corresponding resolutions Δx.

2.5.1 The accretion disk

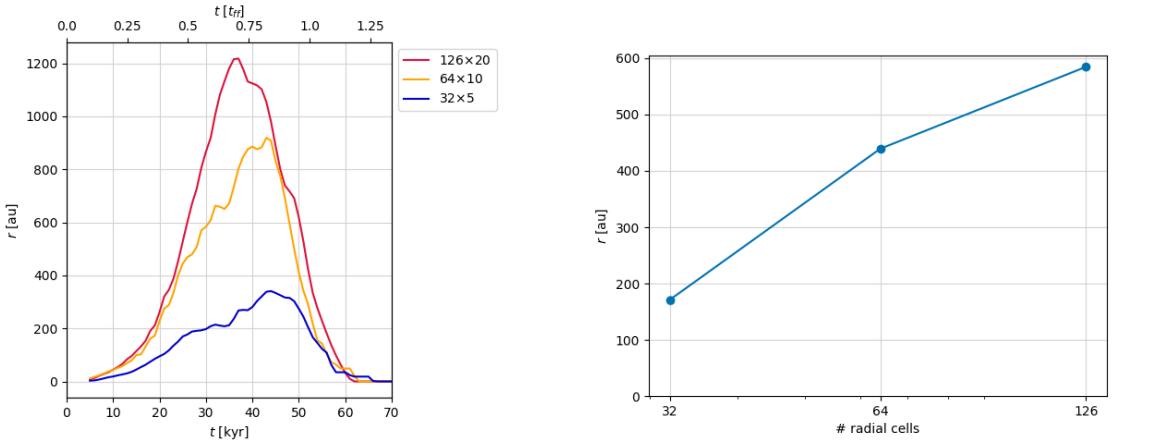

(a) Disk radius as function of time.

(b) Time-averaged disk radius as function of resolution.

Figure 2.3: Convergence properties of the disk radius for different resolutions.

Generally, we find circumstellar disk formation in all simulations we performed, regardless of resolution or sink cell size. Critical for this outcome is non-ideal MHD which reduces magnetic breaking in the magnetically decoupled, dense inner part of the accretion disk. Also, we found very massive and spatially extended disks that reach radii of several 100 au, which are, to our knowledge, the most extended disks ever reported in MHD simulations.
The physics of the accretion disk is converged for all but the lowest resolution case, in the sense that we do not observe any principle evolutionary feature present in one but not the other

simulation. This is also reflected in the plots shown in Fig. 2.3. In panel (a), we present the evolution of the disk radius as function of time and, in panel (b), we show its average value over the course of the first free-fall time. We also examined the disk mass as a function of time and, consequently, as a criterion for the its convergence. However, it evolves strikingly similar to the disk's radius and is, therefore, not shown here. To plot the disk radius, we flag a region as part of the disk when it reaches a density threshold of 10^{-15} g cm^{-3} and if it is in a relative stable force equilibrium. To check the latter, we compare the centrifugal force in the region with the gravitational pull and accept it as being in equilibrium if the centrifugal force lies within ±5% of the gravitational force. We double-checked this criterion in all simulations and it reliably only detects parts of the stellar environment that can be clearly identified as part of the accretion disk, i.e. that these regions lie close to the equatorial plane and have a significant density contrast to the envelope.
The most striking similarity between different kinds of simulations is the (centrifugally supported) disk's lifetime. The first detectable centrifugally supported structure lies within an 100 yr-interval for all resolutions, and after $\simeq$ 50 kyr, they vanish similarly within a time span of $\simeq$ 5 kyr.
It is quite obvious that the disk in lowest resolution simulation evolves differently from the higher resolved simulations with a significantly smaller (and less massive disk), also showing an earlier peak radius (and mass). This is also reflected in the disk's time evolutions in panel (b), with much larger discrepancies between simulation 32×5 and 64×10 than between 64×10 and 126×20. The disk radius increases very significantly from the simulation 32×5 to 64×10, with a difference of 61%, while from 64×10 to 126×20, the difference reduces to just 34%. This trend is indicative of more closely approaching a converged result. Also, the time evolution of the higher resolved simulations clearly shows a pronounced correlation during the whole simulation.
Additionally, a possible influence on the disk radius in the highest resolved simulation is due to it having more cells in the polar direction, resulting in the ability to resolve the same scale height with more cells. Therefore, the density of the cells at the equatorial plane tends to increase with resolution and with that, there tend to be more cells that fulfill the density criterion that we apply at each cell (in the equatorial plane, where we measure the disk radius and where most of the mass is concentrated). As a result, we expect the actual physical properties of the disk to be globally better converged than shown by these plots.
Concluding, both high resolution simulations with 64×10 and 128×20 grid cells yield converged results with respect to the accretion disk physics. This grid relates into spatial resolutions of 0.17 au and 0.8 au, respectively, within the launching region close to the central host star.

2.5.2 The magneto-centrifugal jet and the magnetic tower flow

In this section, we analyze the convergence properties of the outflows. Comparable to the previous considerations on the disk, we apply a criterion to decide if a region is considered part of the outflow. Here, we allow only regions within 30° from the polar axis, a minimum vertical velocity of 0.1 km/s, and with a distance of > 300 au from the origin to contribute to the total mass, momentum or angular momentum of the outflow. The minimal radius and maximal polar angle are used to only include stable parts of the outflow, thereby excluding short-lived perturbations in the disk or the central launching region.

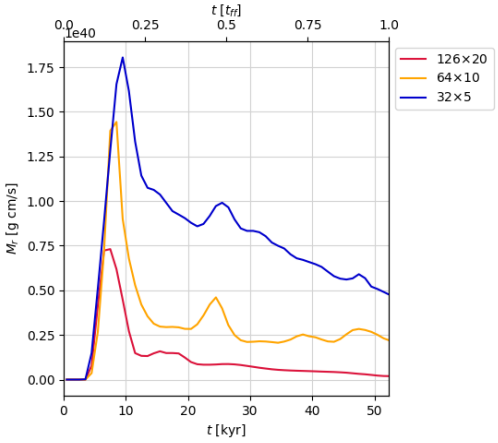

(a) Total linear outflow momentum as function of time.

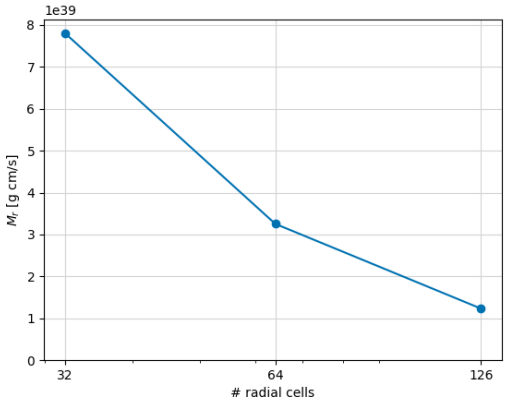

(b) Time-averaged outflow momentum as function of resolution.

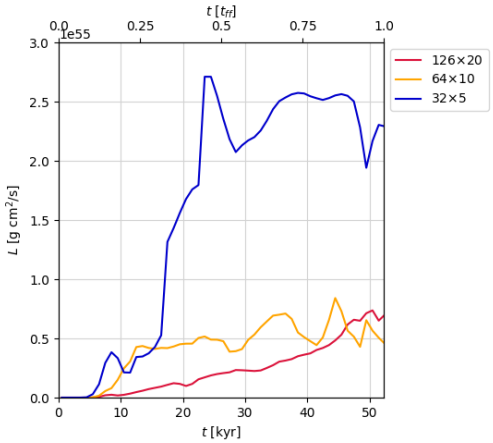

(c) Total outflow angular momentum as function of time.

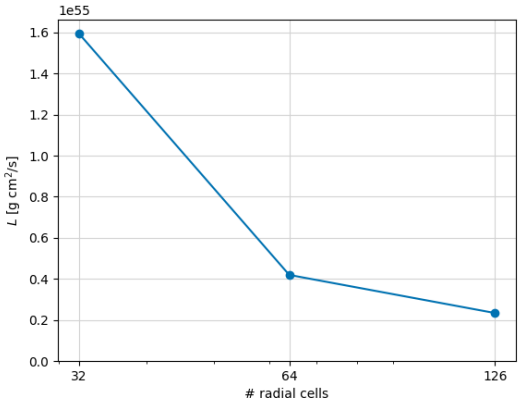

(d) Time-averaged outflow angular momentum as function of resolution.

Figure 2.4: Convergence properties of the outflow for different resolutions.

Similar to the accretion disk, the physical properties of the outflows seem well converged in both higher resolved simulations and are significantly different from the lowest resolved simulation. The most striking difference is that only in the higher resolved simulations (i.e. 64×10 and 126×20), a very wide low velocity tower flow can be independently identified. In contrast, in simulation 32×5, the magneto-centrifugal jet and the tower flow seem to be merged in the same cells.
Both the momentum as well as the angular momentum content of the outflow, shown in Fig. 2.4, panels (a) - (d), clearly demonstrate that both higher resolved simulations 64×10 and 126×20 follow a qualitatively similar evolution. The linear momentum seems to behave similarly for all simulations with a strong initial ejection burst at 4 kyr, containing a lot of momentum. This very high momentum is primarily carried by entrained envelope material that is moved upwards when the outflow cavity forms but does not necessarily leave the domain. For 32×5 and 64×10, the total momentum content of the outflow then decreases until the

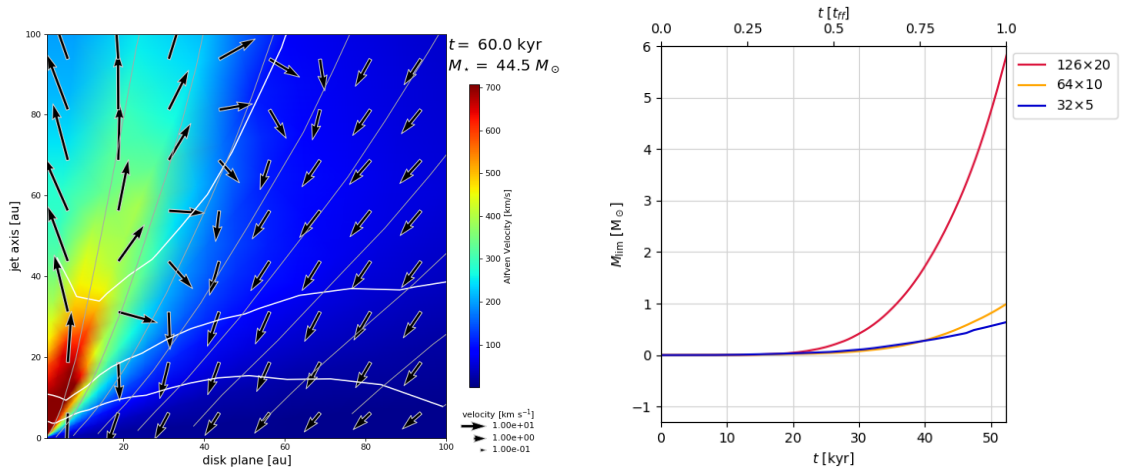

(a) Alfvén velocity after one free-fall time. The white density contours correspond to 10^{-15}g cm^{-3}, 10^{-14} g cm^{-3}, and 10^{-13} g cm^{-3}.

(b) Total mass generated by the Alfvén velocity-limiter.

Figure 2.5: Regions of activity of the Alfvén velocity-limiter and the injected mass for different resolutions.

end of the simulations and another short peak is visible after 20 kyr. For 126×20, the total linear momentum transported by the jet decreases as well after the initial burst but only up to a free-fall time at 52 kyr. A tower flow is only distinguishable in both higher resolution simulations 64×10 and 126×20 shortly after the initial launching of the fast jet component. It becomes dominant both in linear and angular momentum after one free-fall time, when the ram-pressure of the infalling envelope does not constrain it anymore.

The angular momentum content of the outflows seems to follow a totally different evolution in the lower resolved simulation 32×5. The reason is that it is impossible to distinguish between a slow tower flow and the fast magneto-centrifugal jet due to the low resolution. Comparing this simulation to the jet/wind launching region in the higher resolved simulations reveals that both processes initially take place so close to each other that they would have to take place in the same cells for simulation 32×5. In all simulations, the magnetic field close to the polar axis is strongly dominated by its poloidal components. Therefore, there is no magnetic pressure gradient in the vertical direction that would result in a force comparable to gravity, which would be a good indicator for a magnetic tower flow. Instead, for simulation 32×5, the strong centrifugal acceleration close to the polar axis, combined with the large cell size there, leads to a magneto-centrifugal acceleration active in a large volume. At larger radii, a magnetic pressure gradient develops in 32×5 as well, not as strong as gravity, but still contributing to the vertical acceleration. Therefore, basically the whole outflow in the low resolution simulation is powered by an unresolved magneto-centrifugal process, aided by a small magnetic pressure gradient, that together accelerates huge amounts of mass with relatively high velocities leading to the momentum-rich outflow visible in Fig. 2.4.

The last difference we want to point out here is that in simulation 126×20, the magneto-centrifugal jet ceases after one free-fall time. Like simulation 126×20, simulation 64×10 possesses the resolution necessary to develop an independent tower flow. Still, unlike in simulation 126×20, the magneto-centrifugal jet is active until the end of the simulation.

The reason is that simulation 126×20 can resolve the region close to the polar axis with twice the number of cells. This also allows for a higher density contrast, resulting in lower densities directly at the pole. Unfortunately, the polar axis is also the region with the highest magnetic field strengths. Therefore, the Alfvén velocity increases drastically, reducing the simulation timestep significantly. As described in section 2.3.3, we avoid a total halt of the simulation by injecting mass into cells that reach a certain Alfvén velocity. This Alfvén limiter is implemented in a momentum conserving fashion, damping the rotational velocity necessary for the centrifugal launching and the resulting flow upwards, eventually halting the fast magneto-centrifugal jet completely. This is also reflected in Fig. 2.5b which shows the mass created by this Alfvén velocity-limiter during the full 100 kyr simulation. Panel (a) of the same figure shows the Alfvén velocity in the close vicinity of the protostar after one free-fall time, as well as the density contours of its surroundings. As visible there, the Alfvén limiter is active in the outflow cavity and can, therefore, influence the jet's evolution. Fig. 2.5b shows that the Alfvén limiter produces more than 25 $M_\odot$ over the course of the simulation, while simulation 64×10 produces less than 5 $M_\odot$. In both cases, the bulk of this mass is produced after one free-fall time when the ceasing supply of material leads to very low densities in the polar regions. This drain of material due to the finite mass reservoir of the initial conditions would most likely not occur if larger-scale mass reservoirs will be taken into account; see Kuiper and Hosokawa [2018] for a comparison of these two accretion scenarios. An Alfvén velocity of 700 km/s is only reached in the cells in vicinity of the polar axis and close to the protostar, as visible in panel (b) for simulation 126×20. Therefore, it does not influence the magnetic tower flow at larger radii. The fact that the fast jet component vanishes in simulation 126×20 is not obvious from the linear and angular momentum transported by the jet after one free-fall time. The reason is that the fast jet, although it accelerates gas to very high velocities, only carries relatively low masses compared to the low-velocity tower flow and, therefore, also transports much less momentum in total if it is properly resolved. Another interesting aspect we can see here, is that angular momentum seems to be much more efficiently transported via the magnetic tower than via the fast jet. This is evident in simulations 64×10 and 126×20, where angular momentum transport increases significantly when the magnetic tower dominates the outflow after one free-fall time.
Concluding, resolutions of ≤ 0.17 au seem to be sufficient to resolve the magneto-centrifugal jet and a magnetic pressure-driven tower flow independently. Though, our simulations with the highest resolution of 0.09 au showed a significant influence of the Alfvén velocity-limiter that can be avoided with less resolution. Though this method is widely used and an implementation conserving the momentum is an obvious first choice, other methods of limiting the Alfvén velocity should also be considered for future research.

2.5.3 The protostar

The protostellar mass depicted in Fig. 2.6a shows that the simulations are clearly resolution dependent w.r.t. the protostellar evolution. These results partly mirror the insights that we gained from section 2.5.2. For lower resolutions, a significantly higher mass is ejected, as visible in Fig. 2.6b, and this ejection, by necessity, robs mass from the protostar. This is also reflected in the accretion rate to the protostar visible in Fig. 2.7.
To take this into perspective: for simulation 126×20 by one free-fall time 50 $M_\odot$ has been accreted to the protostar and only $\simeq 5$ $M_\odot$ were ejected. For 32×10, in contrast, the poorly

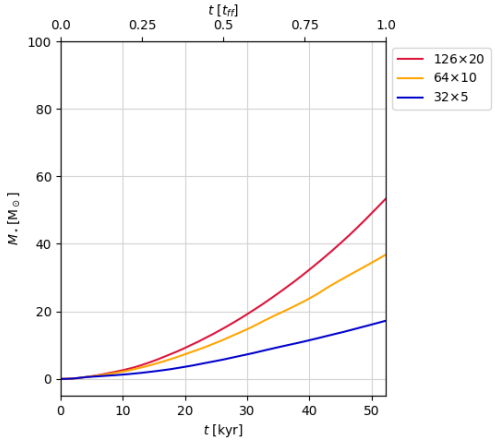

(a) Protostellar mass as a function of time.

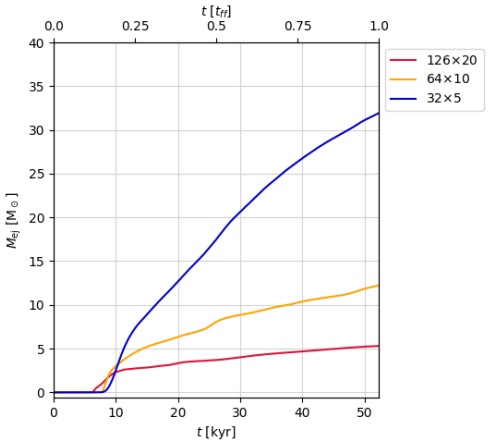

(b) Mass ejected from the computational domain as a function of time.

Figure 2.6: Convergence properties of the accreted and ejected mass for different resolutions.

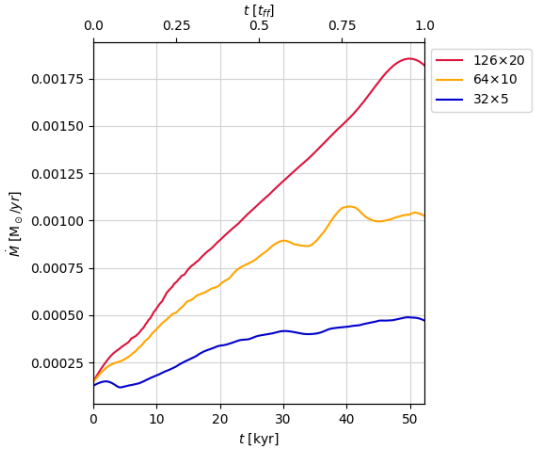

Figure 2.7: Accretion rate to the protostar as a function of time and for different resolutions.

resolved magneto-centrifugal launching mechanism ejects vast amounts of mass, such that at one free-fall time 32 $M_\odot$ were already ejected from the simulation, while only $\simeq$ 18 $M_\odot$ were accreted.

As a conclusion, different resolutions have a very significant influence on the outcome of such collapse simulations. While the disk evolution is not strongly affected, properly resolving magneto-centrifugal jets is of major importance, and the simulation with 32×5 cells, corresponding to a resolution of 0.37 au at the protostar, is not able to achieve this. We deem both the fact that the magneto-centrifugal jet ceases in the highest resolved simulation as well as the unrealistically low ejection-to-accretion ratios to be a result of the Alfvén limiter. Without it, however, a simulation with such a long temporal span and with such great resolutions would not have been possible. Also, the type of Alfvén limiter we implemented is the most commonly used, as other methods of changing the Alfvén velocity often have much greater complications. It is worth noting here that even before reaching one free-fall time, radiative effects become essential for the consequent realistic evolution of the system. We

expect them to have an impact on the bipolar low-density cavity region when the protostar reaches ≥ 20 $M_\odot$ which happens at $\simeq 30$ kyr in our simulations. Here, we focus on the convergence properties of the MHD physics and leave the interaction with the radiation feedback, as e.g. modeled in Kuiper and Hosokawa [2018], to future studies.
Up until this point, though, we consider our simulations to be a realistic approximation to reality due to their very high spatial resolution and due to the good agreement of the higher resolved simulations, especially concerning the launching event and the consequent evolution of the accretion disk and both types of outflows. Even though we do not expect a realistic outcome for our simulations after one free-fall time, all the described effects show the importance of thorough convergence analyses. Another important numerical parameter of our simulations is the sink cell size. Its influence on the results are checked in the following convergence study.

2.6 Convergence properties for different sink cell sizes

As described in Sec. 2.3.1, we use a spherical grid with cell sizes that increase logarithmically in the radial direction. This increases the resolution in the center and close to the protostar greatly, while we can still cover a large cloud core up to 0.1 pc. However, smaller cell sizes also result in small computational time steps and, therefore, we have to truncate this grid close to the origin. There we introduce a sink cell that models the forming protostar and the innermost regions around it.[4]
In the following sections, we discuss the effects of changing the size of this sink cell. Here, we compare four simulations with sink cell sizes of 30.3, 10.9, 3.1, and 1.0 au. Again, all other physical and numerical parameters are kept. However, instead of using the same number of cells in each direction, we keep the resolution and with it the cell sizes and positions constant. This means that the grid with a 30 au sink cell has a lower number of cells in the radial direction than a grid with a smaller sink radius. Still, the cells at radii > 30 au have the exact same positions and sizes in each direction. This way, a grid with smaller sink radius simply has additional cells closer to the forming protostar. The subsequent sections discuss the sink cell size's influence on the disk's, the outflows', and the protostar's evolution.

2.6.1 The accretion disk

The sink cell size impacts the convergence properties of the disk to a lesser degree than resolution changes. The disk radius closely follows a similar evolutionary trend regardless of sink cell size as visible in panel (a) of Fig. 2.8. Again, the disk lifetime seems to be mostly unaffected, though there are major discrepancies between simulations with very large and small sink cells, which is reflected by their corresponding time-average plotted in panel (b). The simulation with the largest sink cell radius $r_{\mathrm{sink}} = 30.3$ au shows a very significant divergence as its disk radius does not reach the same global maximum of $\simeq 1200$ au in contrast

[4]More or less all grid-based astrophysical simulations also use the concept of sink cells or sink particles, because with increasing densities, at some point, they cannot resolve physically important scales with enough cells anymore (usually the Jeans length or Toomre Q) and at that point it becomes more useful to use a subgrid model to simulate the insides of such a cell.

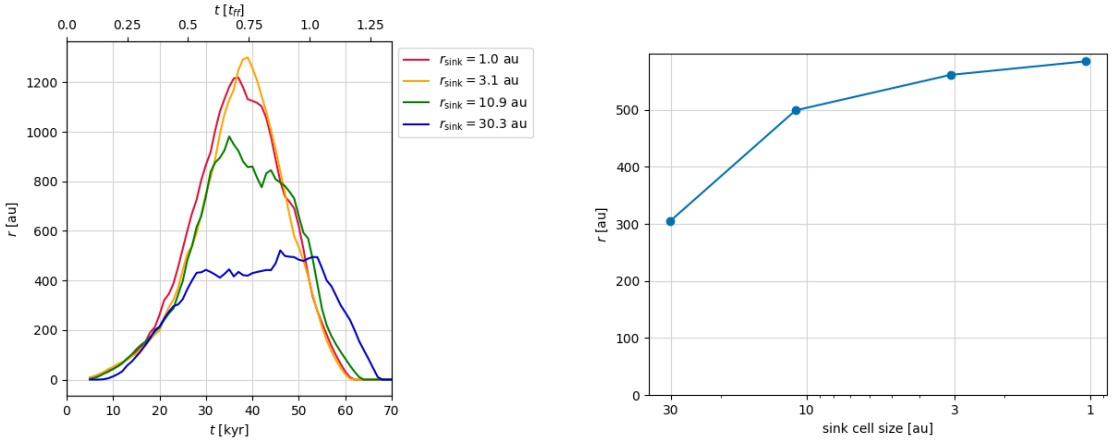

(a) Disk radius as a function of time.

(b) Time-averaged disk radius as a function of sink cell size.

Figure 2.8: Convergence properties of the disk radius for different sink cell sizes.

to the simulations with $r_{\mathrm{sink}} = 1.0$ au and $r_{\mathrm{sink}} = 3.1$ au, but remains only below 600 au at all times. The simulation with $r_{\mathrm{sink}} = 10.9$ au shows intermediate values for the disk radius. Further analysis shows that the part of the accretion disk that lies in the domain has a relatively similar-shaped density structure, but differs in angular momentum content. For the simulation with larger sink cell radii $r_{\mathrm{sink}} = 30.3$ au and $r_{\mathrm{sink}} = 10.9$ au, this results in a weaker centrifugal support. This probably stems from the fact that more material and with it more angular momentum was accreted into the larger sink cell and is not available to be redistributed in the disk to establish the necessary velocities.
As visible in Fig. 2.8b, with decreasing sink cell size our results clearly approach a converged state with very insignificant differences between $r_{\mathrm{sink}} = 3.1$ au and $r_{\mathrm{sink}} = 1.0$ au. As a conclusion, a sink radius of 3.1 au is sufficient to capture the physics of the accretion disk realistically. In contrast, already a sink radius of 10.9 au, which is a commonly used size for a sink particle/sink cell, has problems with the realistic accretion of angular momentum that is then missing from the forming disk.

2.6.2 The magneto-centrifugal jet and the magnetic tower flow

The outflows behave similarly to the disk with varying sink cell sizes. Here, we can clearly distinguish the evolutionary tracks of the simulation with $r_{\mathrm{sink}} = 30$ au from simulations with $r_{\mathrm{sink}} = 3$ au and $r_{\mathrm{sink}} = 1.0$ au, while the simulation with $r_{\mathrm{sink}} = 10$ au, again, shows an intermediate behaviour.
As visible in panel (a) of Fig. 2.9, showing the total linear outflow momentum as a function of time and panel (b) showing its time-average over the course of the simulation, the simulation with $r_{\mathrm{sink}} = 30.3$ au launches its outflow far later than the other simulations but with a much higher momentum over a long period of time, also resulting in much higher average momenta. Generally, lower sink cell radii tend to produce earlier outflows; simulation $r_{\mathrm{sink}} = 1.0$ au launches its outflow at 4 kyr, $r_{\mathrm{sink}} = 3.1$ au at 5 kyr, $r_{\mathrm{sink}} = 10.9$ au at 8 kyr, and $r_{\mathrm{sink}} = 30.3$ au at 12 kyr. Simulations with $r_{\mathrm{sink}} = 3$ au and $r_{\mathrm{sink}} = 1.0$ au, on the other hand, show a strong,

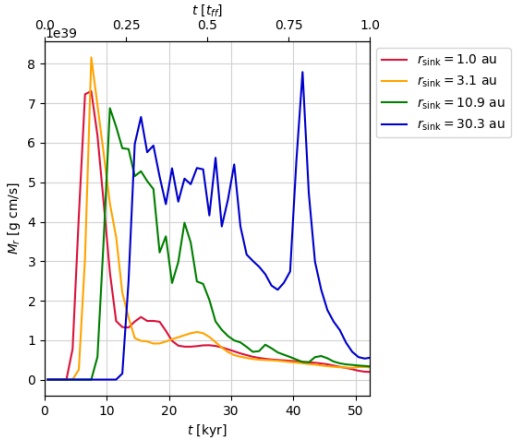

(a) Outflow momentum as a function of time.

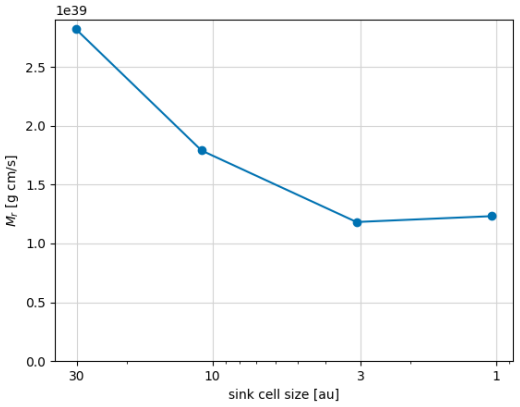

(b) Time-averaged outflow momentum as a function of sink cell size.

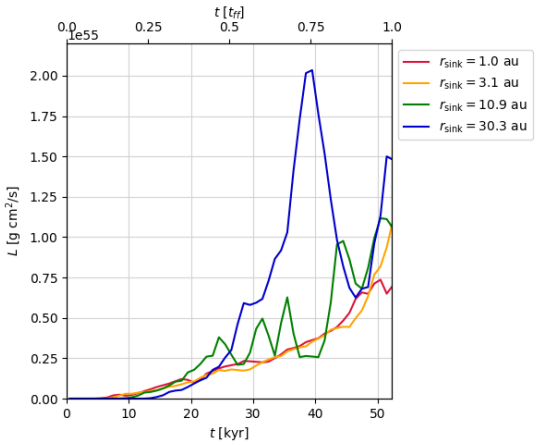

(c) Outflow angular momentum as a function of time.

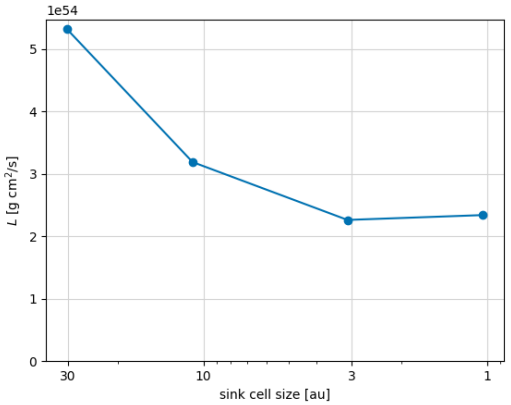

(d) Time-averaged outflow angular momentum as a function of sink cell size.

Figure 2.9: Convergence properties of the outflow for different sink cell sizes.

but short-lived outflow and then immediately settle down to lower average outflow momenta. This effect is foremost due to a broader launching region above the sink cell for larger sink radii which is due to two contributing factors. First, the physical extent of the cells launching the outflows increases with sink cell size, since the outflows are always launched in close proximity to the protostar and, consequently, launch very close to the sink cells, resulting in larger launching radii for simulations with a larger sink cell sizes. Second, the larger sink cell sizes also result in a slightly different magnetic field morphologies, effectively allowing even more cells to launch an outflow. This ultimately leads to an acceleration that affects a significantly larger volume, in turn launching more mass.
As also mentioned in Sec. 2.5, we found that most of the angular momentum is transported by the tower flow instead of the magneto-centrifugal jet and that the tower flow is active at larger radii. Therefore, it is not surprising that the angular momentum transport through outflows does not differ significantly between simulations with different sink cell radii. This is very

apparent in Fig. 2.9c, showing the angular momentum content of the outflow as a function of time, and in Fig. 2.9d, showing its time average, as the differences in angular momentum in the outflow are much smaller than the differences we just observed for the linear momentum. After one free-fall time, all simulations produce an extremely wide outflow tower flow. However, there is a surprising difference. In the simulation with $r_{\rm sink} = 30.3$ au, the linear and angular momentum in the outflow increases much less drastically than in the other simulations. This reveals another interesting aspect of this tower flow: it is extremely sensitive to changing magnetic field topology. In the simulation with $r_{\rm sink} = 30.3$ au, the wider and continuously active magneto-centrifugal outflow launched close to the large sink cell disturbs the magnetic field morphology at larger distances from the protostar than it does for lower sink cell radii. Therefore, while in simulations with small sink cell sizes it slowly engulfs the whole region from a few 100 au up to > 10000 au, the relatively weak tower flow can only develop in a few parts of the simulation for larger sink cells.
Similarly, the fast jet component totally vanishes for the simulations with $r_{\rm sink} = 3.1$ au and $r_{\rm sink} = 1.0$ au which is again due to the small cell sizes in the polar jet launching region where the Alvén limiter produces the most mass. It also suppresses the acceleration due to angular momentum conservation, analogous to simulations with high resolutions discussed in 2.5.2. This time, though, the resolution is constant in each simulation, but the cell sizes reduce close to the origin.
Generally, the influences of the sink cell size are most apparent closer to the origin and seem to disappear for larger radii at least w.r.t. the ejection-to-accretion efficiency, as indicated in Fig. 2.10, panels (a) and (c), when looking at the total sum of material ejected out of the domain and comparing it to the total accreted mass. There, we find a ratio of $12 - 22\%$ over the total simulation time, also for smaller sink cell sizes, such that the accretion-to-ejection efficiency on large spatial and temporal scales is of the expected magnitude.
Our discussion shows that sinks with 3 au and less are required for a converged result, and most (if not all) Cartesian AMR simulations use an accretion radius of their sink particles to be 4 times the highest grid resolution, i.e. much larger than 3 au, in many cases even larger than 30 au.

2.6.3 The protostar

Comparing the convergence of simulations with different sink radii w.r.t. accretion to the protostar reveals a non-intuitive feature: simulations with larger sink radii accrete less to the protostar and eject more mass out of the domain, as visible in Fig. 2.10a, showing the protostellar mass as a function of time and Fig. 2.10b showing the mass ejected from the simulation. Intuitively, one would expect that a larger sink would ultimately accrete material earlier, before it can be ejected by magneto-centrifugal ejection and, therefore, should show the opposite behaviour.
This feature is a consequence of two processes discussed above. Firstly, simulations with larger sinks produce broader magneto-centrifugal jets that also hinder the accretion to the protostar at intermediate polar angles between between 30° and 70° and only allow accretion close to the equatorial plane, where centrifugal forces and magnetic pressure stabilize the accretion disk further, which gives the outflows more time to eject mass. Secondly, they generally produce more massive outflows, reducing the mass available for accretion.
The first point is especially apparent in Fig. 2.11, showing the accretion rate to the protostar as

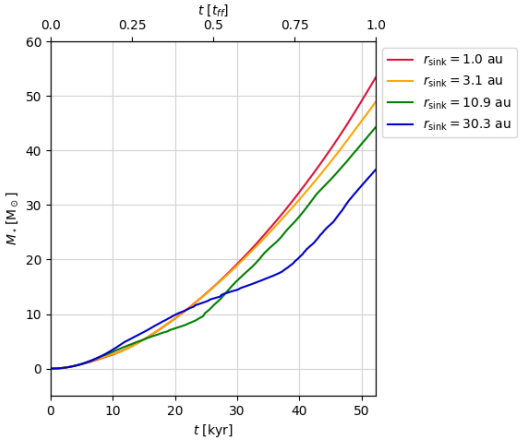

(a) Protostellar mass as a function of time.

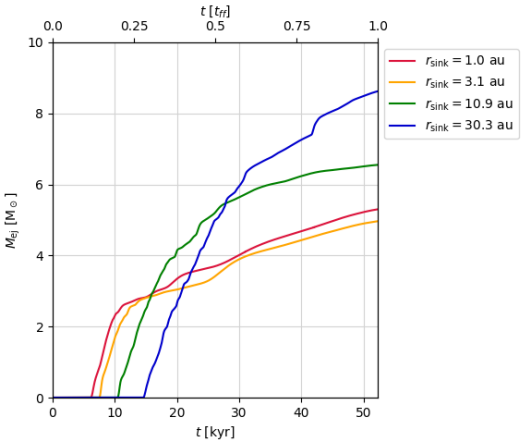

(b) Mass ejected from the computational domain as a function of time.

Figure 2.10: Convergence properties of the accreted and ejected mass for different sink cell sizes.

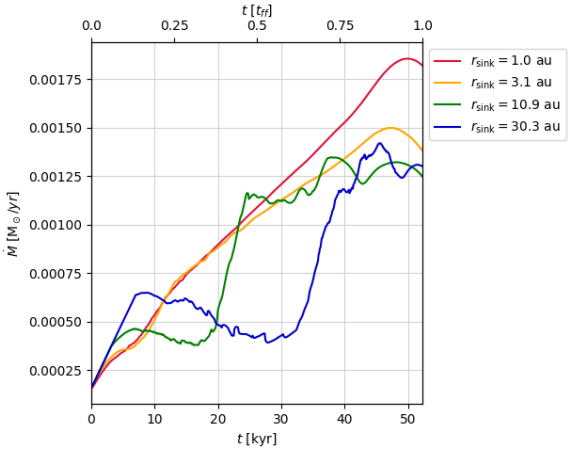

Figure 2.11: Accretion rate to the protostar as a function of time, and for different sink cell sizes.

a function of time, where the accretion after the initial jet launching event at $4 - 12$ kyr (depending on the sink cell size) is further postponed for simulations with larger sink radii ($r_{\mathrm{sink}} > 3.1$ au). The ejected mass shown in Fig. 2.10b shows a similar picture. For larger sink cell radii, the outflows are launched at a later time, accelerate more mass and, consequently, eject more mass out of the simulation, which is then not available for the accretion to the protostar either.

Concluding, we find that the influence of varying sink cell size is similar to the influences of changing resolution, while naively, one would expect that a smaller sink radius allows the jet launching region to extend closer to the central host star, i.e. deeper in the potential well. This, in turn, could lead to a faster magneto-centrifugal jet and, as a consequence, we would also have expected to see an increase in the momentum transported by it. The opposite results are visible here: while larger sink cell sizes lead to a later launching of magneto-centrifugal jets, they are loaded with more mass and their wider launching region hinders the accretion to the protostar, resulting in lower protostellar masses and higher ejection-to-outflow efficiencies.

Further, the influences of the sink radii seem to reduce with distance from the central object. We also find that a sink cell radius of 3.1 au seems to show all the qualitative behaviour we have seen for lower sink radii, while a simulation with $r_{\mathrm{sink}} = 10.9$ au still showed major differences, especially w.r.t. outflow properties. Therefore, to resolve the physics of the outflows properly, we deem a sink cell size of ≤ 3.1 au necessary. Equipped with the knowledge of our convergence study, we are able to assess the reliability of the physical results of our simulations. Well converged results are presented in the next section, before the whole project is summed up.

2.7 Physical Results

In this section, we analyze the data from the simulation with 126×20 and 64×10 cells and with a sink cell radius of $r_{\mathrm{sink}} = 1.0$ au i.e. the highest and second highest resolution simulation with the smallest sink cell. As shown in the previous sections, the disk physics as well as both launching mechanisms are soundly resolved in both simulation and promise realistic results at least up to a free-fall time. After this, the simulation clearly shows signs of unrealistic behaviour due to missing physical effects. The highest resolution simulation is best suited for the analysis of all but one aspect of the physical processes: the magneto-centrifugal jet. As the previous discussion showed, the Alfvén limiter significantly influences the magneto-centrifugal jet in the highest resolution, while other aspects, like the launching process and the independently resolved magneto-centrifugal jet and tower flow, are converged in both simulations. We begin our discussion, in the following subsections, with the physics during the initial free-fall epoch, continuing with jet launching, disk formation, and the formation of the wide angle wind in detail, considering all the forces involved, namely gravity, centrifugal, and magnetic forces.

2.7.1 Gravitational infall and disk formation

Our simulations begin at the onset of gravitational collapse. Consequently, gravity dominates the whole mass reservoir and the prestellar core collapses near free fall for the first 4 kyr. Angular momentum conservation leads to a notably rotationally flattened envelope, more pronounced in the very center. Magnetic fields are of minor importance here, since the initial cloud has only a weak magnetization with average magnetic field strength up to 4×10^{-5} Gs in the innermost 1000 au.
From here on, the first disk-like structure develops. The material is continuously accreted from the envelope and settles down in the midplane. While this disk-like structure is clearly visible in the density plot in Fig. 2.12, it is not yet stabilized, neither by centrifugal nor by magnetic forces. Even though it still has a significant infall velocity and is constantly accreted, it is visible for an extended amount of time because it is fed by the infalling envelope so that the material is always replenished. The subsequent formation process of the disk is depicted in Fig. 2.13. Panel (a) shows the density structure and panel (b) shows the centrifugal force compared with gravity at 5 kyr (on the top) and 10 kyr (on the bottom), respectively. The colors are chosen such that shades of blue indicate that gravity is stronger than the centrifugal force, shades of green mean that a region is close to force equilibrium, and shades of yellow and red visualize the predominance of centrifugal forces, leading to an acceleration towards

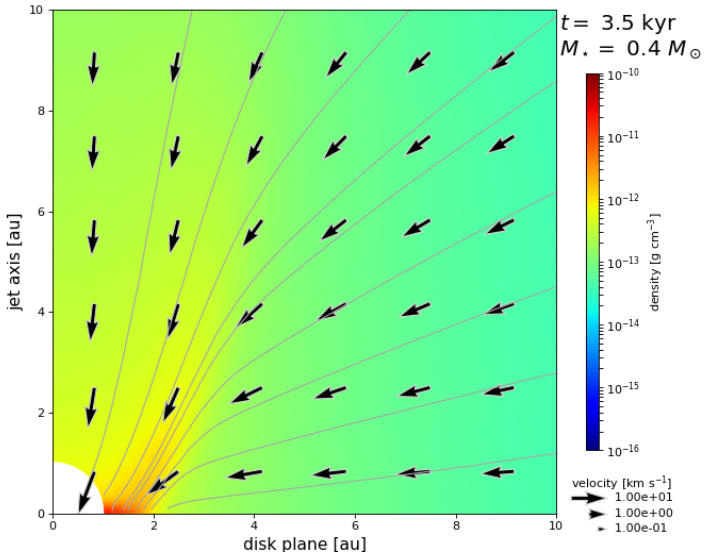

Figure 2.12: The first traces of a disk-like structure emerging.

greater radii.
At the shown time at 5 kyr, the jet has already launched and matured into a stable state and the disk has established a centrifugal support up to ≃ 5 au. Magnetic fields only play a role in the magneto-centrifugal launching process of the jet close to the polar axis and do not support the disk here to an important degree, as the Lorentz force in radial direction, and in the innermost ≃ 5 au of the disk, only accounts for a few percent of the centrifugal force. During the subsequent 5 kyr, the disk expands outwards, also expanding its radius of centrifugal support. At 10 kyr, a centrifugally supported high-density disk structure is already clearly visible in the lower panels of Fig. 2.13, which effectively extends from the protostar to ≃ 100 au. Also visible here is that the innermost 5 au of the disk are not supported by centrifugal forces. Instead, there, the increasing magnetic pressure has reached a magnitude to rival gravity, thereby supporting the accretion disk.
The disk's subsequent temporal evolution is depicted in Fig. 2.14. Here, we defined a threshold density of 10^{-15} g cm^{-3} to decide whether a region belongs to the disk or to the envelope. Additionally, we consider centrifugal support; we consider a region centrifugally supported if the magnitude of the centrifugal force lies within ±5% of the gravitational force. From Fig. 2.14, panel (a) we can see that a part of the disk (on the order of 200 au) is not centrifugally supported, although it reaches high densities of 10^{-15} g cm^{-3}, and that this unsupported part of the disk accounts for a relevant part of the disk's mass, as visible in panel (b) of the same figure.
In principal, there are two parts of the disk that are not supported by centrifugal forces. The innermost part of the disk, close to the protostar, is primarily magnetically dominated. Here, the disk is supported by the magnetic pressure in the equatorial plane. This part accounts for the first ≃ 5 au of the pseudo-disk at 10 kyr and does not contribute to the difference in disk radius, since we plot the maximal radius of the centrifugal disk here, from the protostar to its outer rim. In this part of the disk, the magnetic field is primarily pointing upwards from the equatorial plane. Therefore, angular momentum transport by the magnetic field in the disk is inefficient and its transport takes place primarily by viscous forces. At the same time, the high densities in this area will shield this region from ultra violet radiation, resulting in low

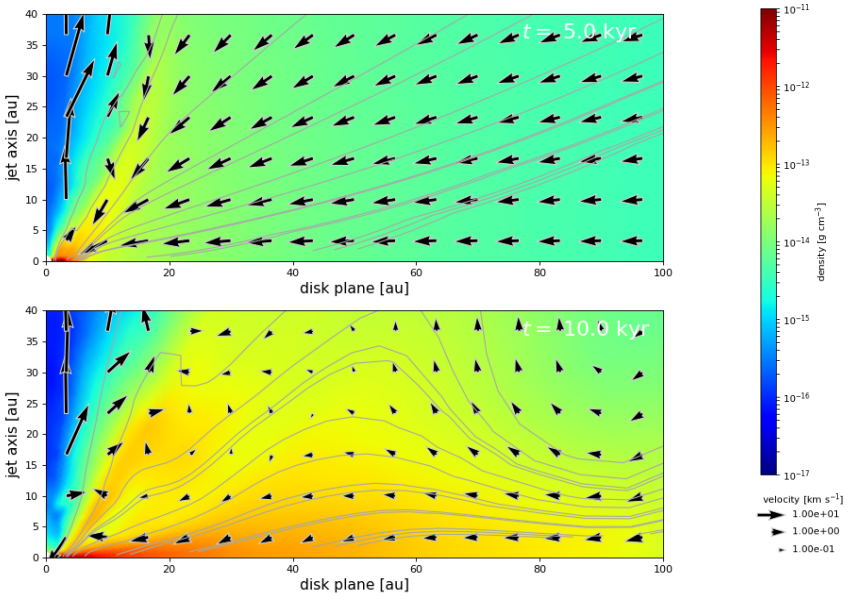

(a) Density structure at 5 kyr (upper panel) and at 10 kyr (lower panel).

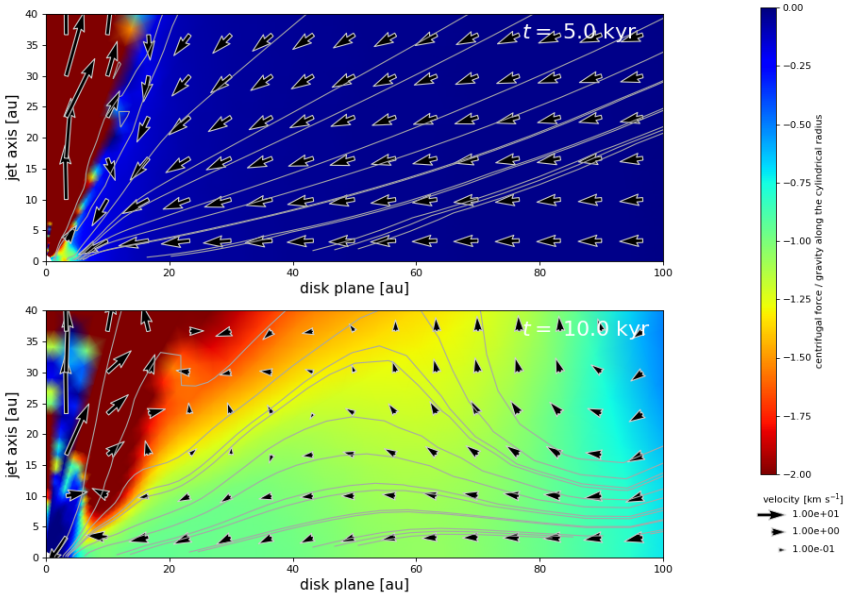

(b) Centrifugal force divided by gravity at 5 kyr (upper panel) and at 10 kyr (lower panel).

Figure 2.13: The disk extents outward during the shown 5 kyr. Clearly visible is that at 5 kyr, only the innermost $\simeq$ 5 au of the disk are centrifugally supported, while at 10 kyr, the disk has already established centrifugal support up to nearly 100 au.

ionizations and high magnetic diffusivities. We take this into account in our simulations by increasing magnetic diffusivity with density, resulting in particularly high values of diffusivity

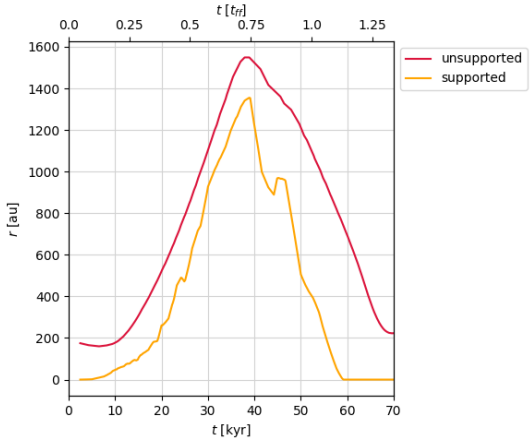

(a) Disk radius as a function of time.

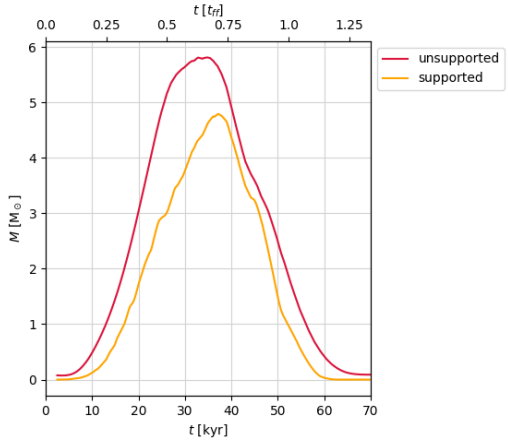

(b) Disk mass as a function of time.

Figure 2.14: Time evolution of the disk; the red line corresponds to the unsuppored, and the yellow line to the centrifugally supported disk.

in this region close to the protostar. Therefore, while the magnetic pressure in this region is high, the viscously decelerated material can still be accreted efficiently, and the region is not perfectly supported against gravity. In such accretion disks around forming high-mass stars, angular momentum transport is expected to be primarily due to gravitational torques of the forming spiral arms, see Kuiper et al. [2011] and Meyer et al. [2017, 2018] for details.
The larger unsupported part belongs to the outer rim of the disk, where material is accreted from larger radii and has not yet spun up to Keplerian velocities but will eventually become part of the centrifugally supported region. This outcome on the physics at the envelope-disk transition is also in agreement with previous simulations of massive disk formation which did not take into account magnetic fields [Kuiper et al., 2011, Kuiper and Hosokawa, 2018] and again shows that only the innermost part of the disk can be supported by magnetic forces.
The envelope is not only a mass reservoir but also a source of angular momentum. Therefore, when less material from larger radii rain onto the disk, it cannot replenish the angular momentum it loses by magnetic breaking, viscosity and potentially by outflows. Therefore, the centrifugal support of the disk vanishes after one free-fall time, as visible in Fig. 2.14. Additionally, the missing ram pressure exerted by the envelope then enables a much larger tower flow to develop that efficiently removes angular momentum from the disk, contributing heavily to its demise.
This effect can be visualized by comparing the green line in Fig. 2.15, which shows the total angular momentum in the outflow, with the angular momentum content in the disk in blue. Here, we consider all regions with positive vertical velocities as part of the outflows, such that they include the magneto-centrifugal jet and the tower flow. Additionally, Fig. 2.15 shows the angular momentum within a sphere of 1500 au radius (in brown) and its net flux though its surface, which we expect to be dominated by the angular momentum loss of the disk. The correlation of angular momentum in the disk and the angular momentum flux is obvious: during the whole simulation, the net flux is negative. Therefore, more angular momentum is accreted into 1500 au than is ejected which is also reflected by the angular momentum content of the disk. Not visible here is the amount of angular momentum extracted by viscous forces and magnetic breaking that lead to the constant reduction of angular momentum in the disk.

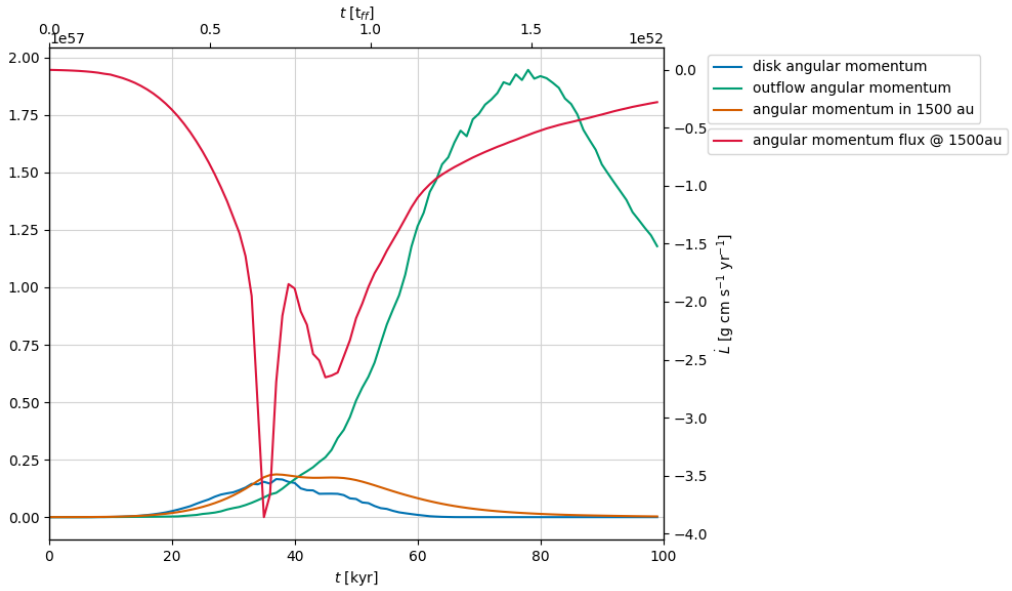

Figure 2.15: Angular momentum in the disk, the outflow, and a sphere of 1500 au radius around the protostar, as well as the angular momentum flux through the surface of said sphere as a function of time.

The maximal influx of angular momentum to the disk is reached at 35 kyr, corresponding to the maximum angular momentum content of the disk. After that, viscosity and magnetic breaking reduce the angular momentum in the disk faster than the envelope replenishes it. From the angular momentum content of the outflow we can deduce that only an insignificant part of the angular momentum extraction is carried out by outflows before one free-fall time, as the magnetic tower is not able to lift material up against the ram-pressure of the infall, and the magneto-centrifugal jet is launched from low radii, where it has a small magnetic lever arm and can only extract an insignificant portion of angular momentum. However, after one free-fall time at 52 kyr, the outflow begins to carry a massive part of the total angular momentum due to the developing tower flow.
Another process occuring after one free-fall-time is that the formerly high scale height of the disk decreases constantly. This is a result of the compression of the magnetic field lines towards the disk and closer to the midplane, as visible when comparing the upper panel of Fig. 2.16 (showing the situation at 5 kyr) with its lower panel (showing the situation after envelope dissipation at 70 kyr). This is also related to the vanishing support by the outer envelope and its constant influx of material that leads to an increased density above the disk. As a result, this potentially increases magnetic breaking, since magnetic field lines within the accretion disk are much more efficient in transporting angular momentum.
As we have seen, the evolution of the outflows has a prominent influence on the disk formation, but its physical evolution is an important topic by itself and will be analyzed in the following subsection.

2.7.2 The magneto-centrifugal jet

The first outflow launches at $\simeq$ 4 kyr after the onset of gravitational collapse. The initial launch event is triggered when the increasing magnetic field strength at the pole equals the

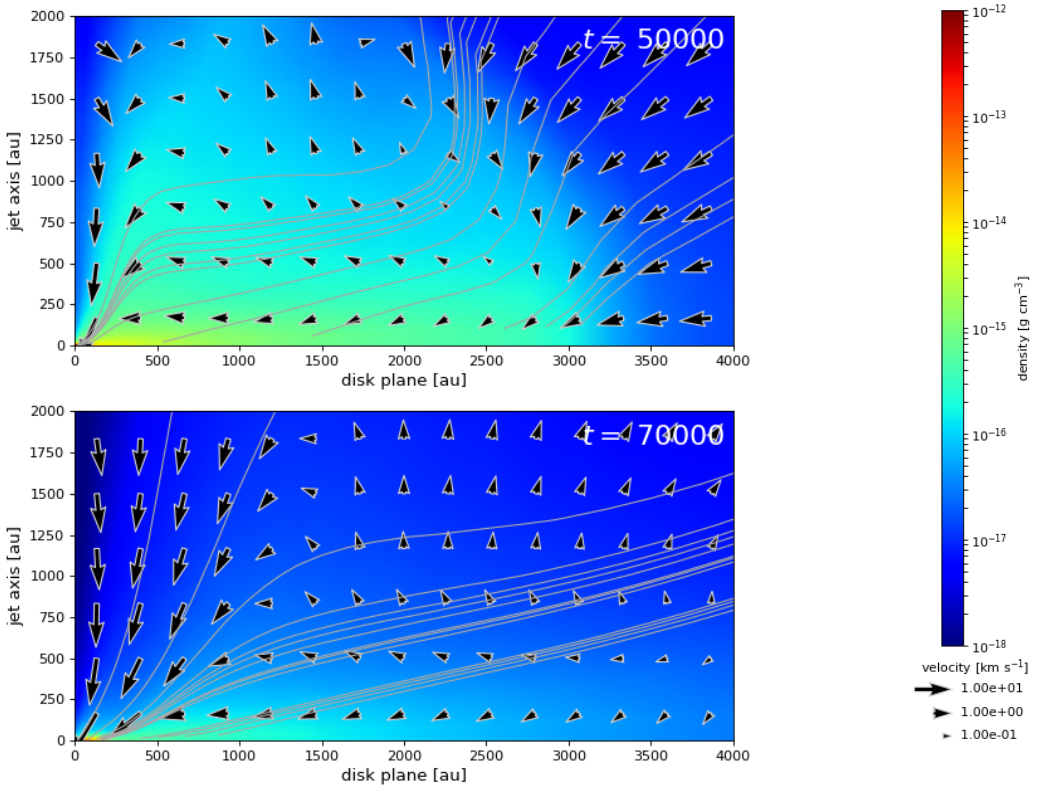

Figure 2.16: Density structure of the accretion disk at 50 kyr (upper panel) and at 70 kyr (lower panel), showing how the disk's atmosphere vanishes after the mass reservoir above the disk is depleted.

level where the local Alfvén velocity reaches the infall-velocity, making the gas flow sub-Alvénic. Previously, the infalling gas was traveling much faster than the magneto-acoustic signal velocity and, in turn, the magnetic field topology was determined by the gas movement. When the flow approaches the sub-Alfvénic regime, the magnetic field lines start to resist the gas movement to a larger degree. Eventually, the Alfvén velocity equals the flow velocity, coinciding with a force-equilibrium between inertial and magnetic forces and the first outflow is launched by a magneto-centrifugal launching process.
The outflow immediately carves out an outflow cavity with a density contrast of 10^2. This also changes the magnetic field topology in the launching region, and the topology of the outflow region changes rapidly for $\simeq 100$ yr, until it reaches a state where it does not change significantly on timescales on the order of several 100 yr. The magnetic field lines that provide the necessary rotational acceleration are anchored in the inner accretion disk at radii < 1 au.[5] In our simulations, the acceleration happens far above the surface of the disk and with magnetic field lines steeply inclined with respect to the equatorial plane, as visible in Fig. 2.17. This is not contradicting Blandford and Payne [1982], who state that in their solution for magneto-centrifugally launched jets the angle between magnetic field lines and the surface of the accretion disk has to be $< 60°$ to be able to accelerate a particle along the corresponding field line. They assumed perfect conductivity, self-similarity for the properties of the jet, and that the particle is launched from the surface of a thin disk. All these assumptions are not met in our simulations. However, this is unsurprising as Blandford and Payne [1982] already argued "A realistic accretion disk must be far more complicated." In our evolving collapse, the foot points of magnetic field lines can move with the accreting material inwards at the equatorial plane, while particles higher up on these field lines are potentially still infalling. When this process continues, the rotational velocity at the foot point of the field line increases, and the rotating field line then accelerates the rotational movement of the previously infalling material, eventually increasing the centrifugal force to match gravity and ultimately reversing the flow direction along the field line. Another process that contributes material to the launching region above the disk and working at the same time is due to non-ideal MHD, which enables particles to slip with respect to the magnetic field lines. When the infalling gas of the envelope comes to a stop at the dense region close to the disk and the protostar, due to the increasing magnetic and centrifugal forces counteracting gravity, it cannot reverse its flow direction immediately, since the high ram pressure of the infalling gas at higher altitudes prevents that. However, it can slip w.r.t. the field lines and can, therefore, diffuse through the wall of the outflow cavity and be accelerated upwards. This launching at higher altitudes is even implicitly included in Blandford and Payne [1982]'s model. With the magneto-centrifugal launching mechanism shown there, it is possible to accelerate particles at higher angles of $\vec{B}$ with the equatorial plane, when the assumption that the particle is directly launched from a thin accretion disk is dropped. This principle is visible in Fig. 2.18, showing the equipotential surfaces of a bead on a wire, where the potential $V(r, z)$ in the vicinity of a central object of mass M is given by

$$V(r,z) = -\frac{GM}{r_0}\left(\frac{1}{2}\left(\frac{r}{r_0}\right)^2 + \frac{r_0}{(r^2+z^2)^{1/2}}\right). \tag{2.5}$$

Here r denotes the cylindrical radius and z the altitude above the equatorial plane. Following

[5] We simulate the rapid rotation of the protostar and the inner accretion disk by zero-gradient boundary conditions for the rotational component of the velocity of the sink cell.

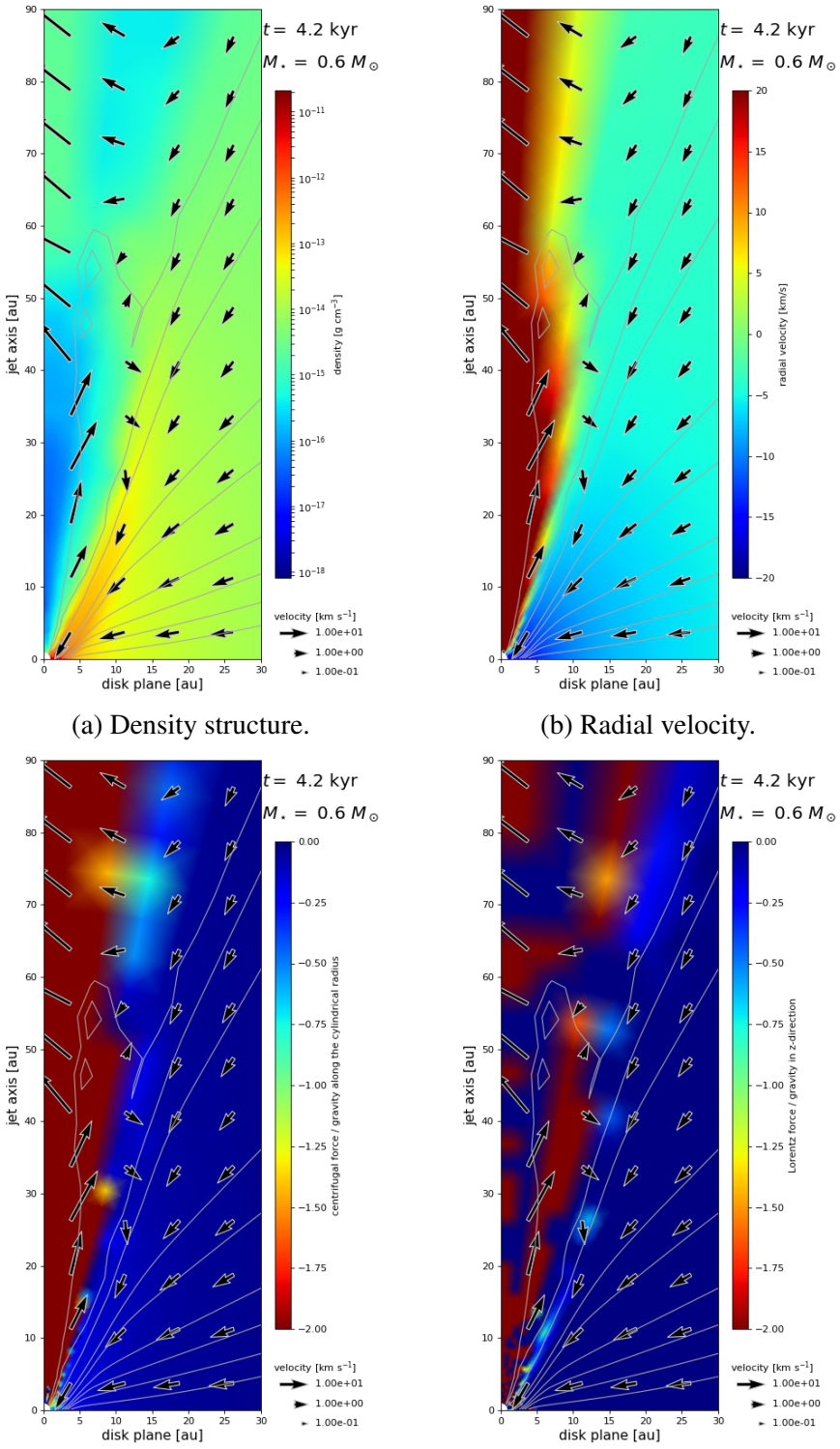

(a) Density structure.

(b) Radial velocity.

(c) Centrifugal force divided by gravity.

(d) Upward pointing Lorentz force divided by gravity.

Figure 2.17: A fast jet is launched from the inner accretion disk, carving out a sparse outflow cavity. The fast rotating field lines close to the protostar exert a strong centrifugal force outwards that moves particles rapidly up the magnetic field lines. The high magnetic field strength enable the Lorentz force to lift the centrifugally accelerated particles upwards, overcoming gravity and inverting the flow direction at the cavity wall.

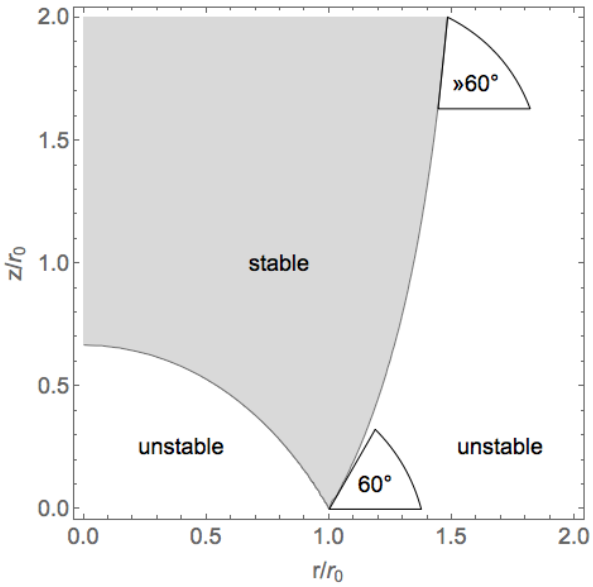

Figure 2.18: Reproduction of Fig. 1 from Blandford and Payne [1982]: equipotential surfaces for a bead on a wire, corotating with the Keplerian angular velocity $\sqrt{GM/r_0^3}$ which is released at r_0.

the field line anchored at r_0 upwards to higher z, we see that the angle increases continuously. This is where, in our simulation, particles are accelerated at altitudes several times the foot point radius of the field line, and with high angles of B. This fast jet is stable during the course of the subsequent simulation. Though, since the mass of the protostar and its immediate surroundings increase with time, the gravitational force increases more rapidly than the Lorentz force needed to accelerate particles upwards along the magnetic field lines. This means that the region where the Lorentz force in vertical direction is stronger than gravity moves upwards during the course of the simulation, effectively moving the launching region with it. There, much of the material that feeds the jet stems directly from the infalling envelope. It is channeled into the jet without ever reaching the midplane and, therefore, it still has significant momentum towards the protostar before its vertical velocity can be inverted by magneto-centrifugal acceleration. In turn, the region of positive vertical velocity is several au above the region of force equilibrium between magnetic and gravitational force. While, initially, it lies within 1 au altitude, at 15 kyr, it has already moved to 1.8 au and continues to increase in altitude to 12.9 au at 46 kyr.
47 kyr after the initial collapse, the supply of material falling in from cylindrical radii close to the sink cell and with it the supply of angular momentum have reduced so much that this fast magneto-centrifugal launching mechanism ceases to work in the highest resolved simulation 126×20, as the Alfvén limiter produces too much mass, while conserving (angular) momentum. Therefore, the last remnants of the outflow then rapidly move outwards along the polar axis and in its wake, material starts to fall in again that is never accelerated upwards by magneto-centrifugal launching. As mentioned above, the simulation with lower resolution and 64×10 cells does not show this behaviour, as the Alfvén limiter produces much less mass. In all simulations, there is another outflow component that remains, a slower wide-angle wind powered by a magnetic tower, which is discussed in the following section.

2.7.3 Wide angle winds

The first traces of a slower wide angle wind become apparent after $\simeq$ 7 kyr. It can be distinguished from the magneto-centrifugal jet by a strong toroidal magnetic field, $\simeq 0$ velocities in the equatorial plane, and higher densities in the launching regions. Its launching mechanism requires that magnetic field lines wind up and produce a vertical magnetic field gradient. This can only happen if the inertial forces of the gas flow are stronger than the magnetic forces and in a region of differential rotation or with a vertical rotational velocity gradient. Therefore, this launching mechanism develops just outside of the Alfvén surface and above the accretion disk, where these conditions are met for the first time. Initially, this is close enough to the magneto-centrifugal jet that both outflows merge at larger altitudes, so that both launching/acceleration principles contribute to the flux. However, with the growing accretion disk, the potential launching area of this magnetic tower grows towards larger radii. Its time evolution is visible in Fig. 2.19, which shows multiple quantities at different simulation times. The first column shows the situation after the jet and tower flow have just formed but are already matured to a stable state and are clearly distinguishable at 10 kyr. The second column shows the situation at an intermediate time, where the launching region of the tower flow has grown outwards at 35 kyr (please note the scale on the x-axis), and the last column shows the tower flow after one free-fall time, when the infall has subsided and the tower flow has expanded at 60 kyr.
At 10 kyr, the tower flow is clearly visible as a separate structure in the (slow) vertical velocity in panel (b), as well as through the ratio of toroidal to poloidal magnetic field[6] $B_\phi/B_{\rm pol}$ shown in panel (c). Here, a strong toroidal magnetic field component, shown by the bright areas in panel (c) indicates that the magnetic field lies to a large degree parallel to the equatorial plane. Usually, this happens outside of the Alfvén surface when the magnetic field lines are wound up by the differential gas flow of an accretion disk and hints at the magnetic pressure-driven nature of the outflow.
During the course of the subsequent simulation, the tower flow's launching radius moves continuously outwards as visible in Fig. 2.19 when comparing the earlier images on the left to the later ones on the right. In panel (a), we can see that the tower flow is active in areas of substantial density. Consequently, it can also accelerate a lot of mass and momentum, though, as visible in panel (b), to much lower terminal velocities compared to the magneto-centrifugal outflow. When the simulation reaches one free-fall-time, there is no more material left to fall in from above. This also means that the considerable ram-pressure of the infall is removed. Thereby, even a small vertical magnetic pressure gradient suffices to drive an outflow. As a result, the wide angle component quickly expands up to more than 10000 au. Comparing the snapshot at 35 kyr with the one at 60 kyr, we can see the effect of the vanishing ram-pressure of the infalling envelope, not only in the extent of the outflow but also in the higher velocities visible in panel (b) where the tower flow has finally accelerated material to velocities of several km/s, while before it was only reaching fractions of km/s.
Comparing our findings with earlier simulations, e.g. the well-cited work by Banerjee and Pudritz [2007], we are, to our knowledge, the first that can clearly distinguish between

[6] *Poloidal* means the components of the magnetic field that lie in the planes perpendicular to the equatorial plane. In cylindrical coordinates, one would speak of the radial direction (often depicted by ϖ) and the vertical direction (usually z). In contrast, the toroidal component of the magnetic field corresponds the components in the equatorial plane, in cylindrical or spherical coordinates the azimuthal direction (usually ϕ).

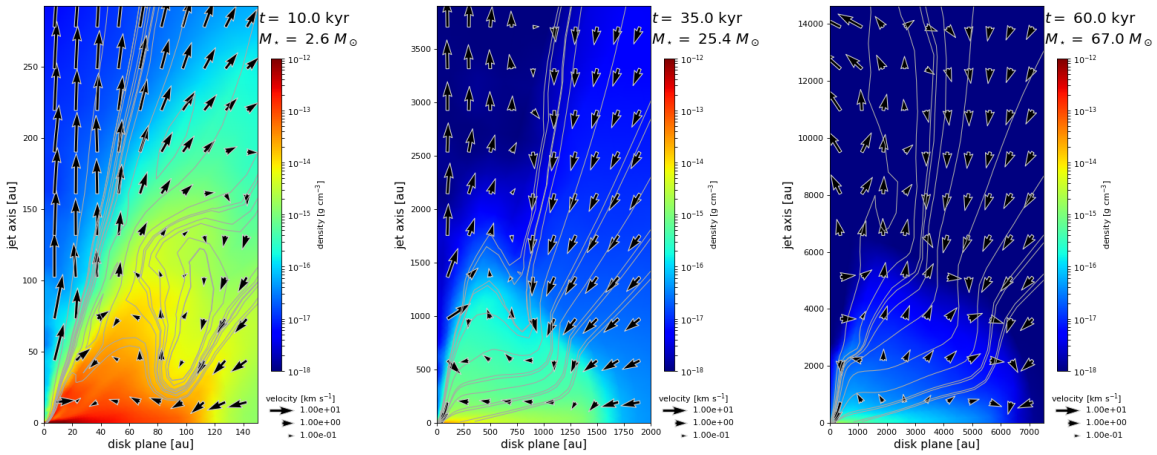

(a) Density structure.

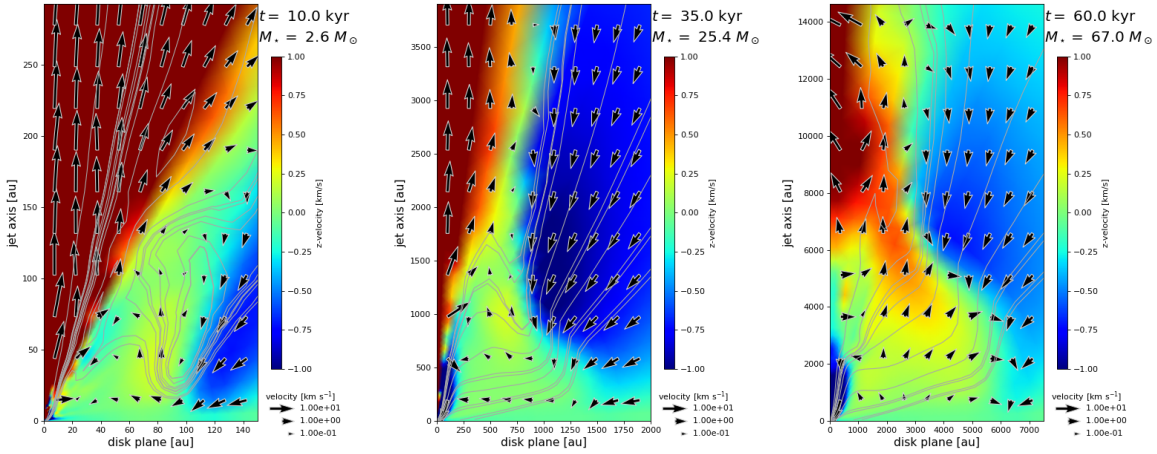

(b) Vertical velocity.

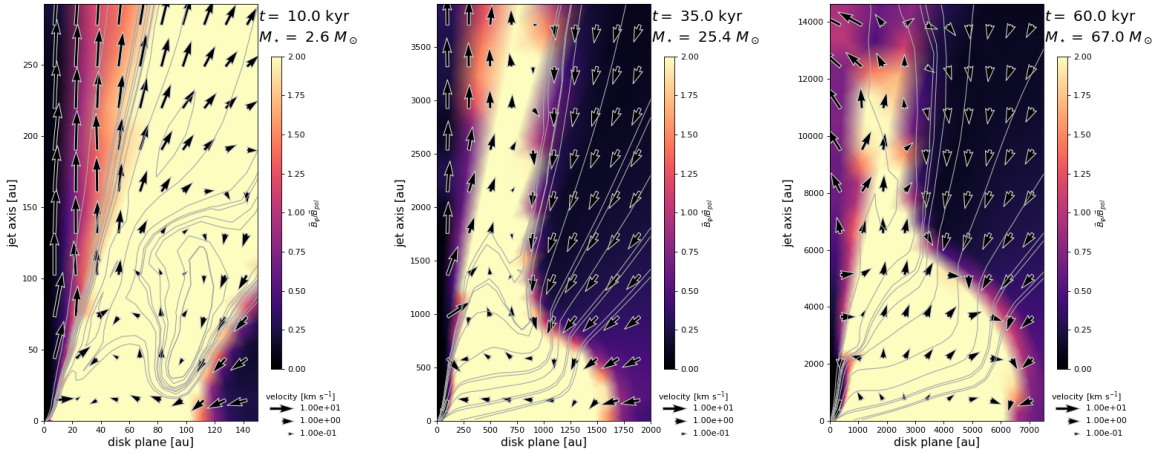

(c) $B_\phi / B_{\rm pol}$.

Figure 2.19: Evolution of the outflow, from 10 kyr at to the left, 35 kyr in the center, to 60 kyr to the right. During this timespan, the magnetic tower flow, indicated by the bright areas in panel (c), expands significantly outwards.

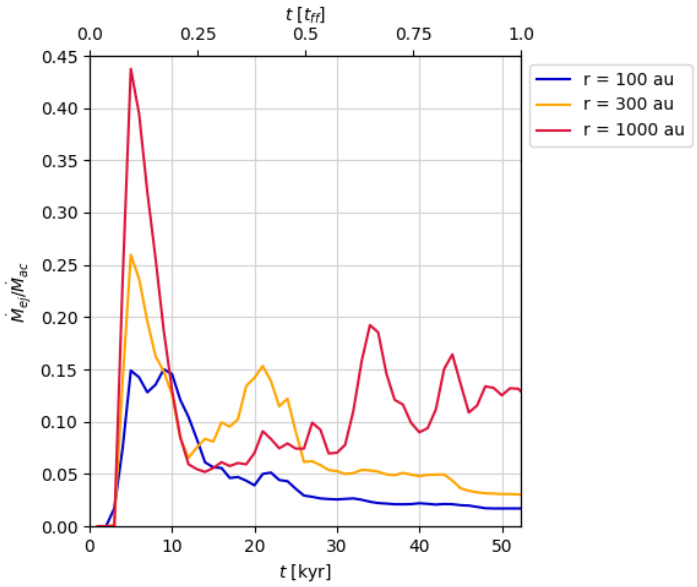

Figure 2.20: The ejection-to-outflow efficiency for different radii.

magneto-centrifugal jet and the massive, slow tower flow which they also describe. In principle, we think that other simulations, for example Matsushita et al. [2017] should be able to resolve this as well, though they do not mention a distinction in particular.
Seifried et al. [2012] analyzed the jet-launching mechanism in detail. Similar to our results, they find outflow components that can be described as magneto-centrifugally launched and magnetic pressure-driven. They find a magnetic pressure-driven component in two distinct situations. In the early stages of disk formation, a magnetic tower develops but only as an early transient phenomenon. Later, magnetic pressure contributes to the launching at larger radii, and correctly they argue that, in their simulations, this magnetic pressure driving should be considered a part of the magneto-centrifugal launching process, which also matches the [Blandford and Payne, 1982] model. We agree that at larger radii, outside the Alfvén radius, magnetic pressure potentially contributes to the acceleration of formerly magneto-centrifugal jets. However, we find that one needs a significantly higher resolution to distinguish between magneto-centrifugal jet and tower flow. In fact, we find a similar hybrid magneto-centrifugal and magnetic pressure-driven outflow for our low-resolution simulations.
Both launching mechanisms contribute to the ejection-to-outflow efficiency. In Fig. 2.20, we present the ejection-to-outflow efficiency at different radii, for simulation 64×10. At all radii, the launching event with its very massive outflow by entrainment is visible. However, since more material can be entrained at higher radii, the ejected mass gets larger with increasing radius. After this initial ejection by entrainment, the efficiency goes down to values $\simeq 0.1$ as is expected from observations. Towards even later evolutionary timescales, we can observe how the magneto-centrifugal jet and the tower flow separate from each other in radius. At one free-fall time, the magneto-centrifugal jet component that is active well within the first 100 au only reaches a low ejection-to-accretion ratio of 0.015, while at larger radii the tower flow contributes significantly, increasing the ejection-to-outflow efficiency to 0.15 at 1000 au. While the magneto-centrifugal jet is affected by the Alfvén limiter in the highest resolution simulations (which we do not discuss here), we want to note that integrated over the whole timescale of the simulation, we find ejection-to-outflow efficiencies of $\simeq 0.12$, which are quite

compatible with observations. This is visible in Fig. 2.6 panels (a) and (b). The reason is that the magneto-centrifugal jet only contributes to a minor degree to the total outflowing mass, additionally indicating that the total observed ejection-to-outflow efficiency is also a time-dependent quantity.

2.8 Summary

There are numerous unresolved questions regarding the formation process of massive stars. In contrast to low-mass stars, they are commonly found in large distances from our solar system, reducing the potential resolution of their observations. This is not the only factor that makes their formation process more difficult to observe than their low-mass counterparts. More massive stars form in equally massive and, therefore, denser cloud cores, rendering their environment more opaque to observations. There are, however, traces of their formation process that are visible to us; their bright large-scale jets and outflows, which are the focus of the present chapter. Given that we have access to much more information on low-mass protostars, it is natural to pose the question, to what degree the formation processes of low and high-mass stars work similarly, and where they diverge. Another important issue arises from the fact that massive stars influence their environment via different feedback mechanisms much more than low-mass stars do, even in their early stages of evolution. Therefore, important aspects of our analyses are the properties of protostellar jets and outflows.
To contribute to the solution of some of those issues, we conduct magneto-hydrodynamic (MHD) simulations using the state-of-the-art code PLUTO, combining non-ideal MHD, self-gravity, and very high resolutions, as they have never been achieved before. Our setup includes a 100 $M_\odot$ cloud core that collapses under its own self-gravity to self-consistently form a dense disk structure, launching tightly collimated magneto-centrifugal jets and wide angle tower flows. To benchmark the quality of our results and analyze requirements of general MHD-simulations, we conduct a detailed convergence study, not only changing the resolution, but also the radius of sink cells, which represent the forming protostar and analyze the requirements to resolve physical processes in the disk and during outflow launching. Previous simulations sometimes found that centrifugally supported disk formation is even possible in ideal MHD. We do not fancy this to be accurate. We conclude that non-ideal MHD is required to form such accretion disks. We think that in earlier studies, which show the formation of small circumstellar disks in ideal MHD, the formation process is most likely enabled by numerical diffusivity due to lack of resolution per disk pressure scale height. With the resolution our simulations provide, centrifugally supported disk formation is only possible when considering a magnetically dead zone in the most dense regions of the accretion disks. By including such a dead zone, the size of the disk in our MHD simulations approaches values of non-magnetic simulations, i.e. several 100 au, where the exact value depends on the initial angular momentum content of the collapsing cloud. The resolution study reveals a strong dependence of the disk size on spatial resolution, with higher resolution simulations forming larger and more massive disks. The reason is that it is necessary to resolve the densest part of the disk's midplane in order to see the strongest impact of the non-ideal MHD term. We found that a converged result is obtained for a spatial resolution of $\Delta x \leq 0.17$ au (at a radius of 1 au). The central result of the resolution study is that the nature of the outflow depends critically on spatial resolution. Only high resolution simulations are able to resolve a

magneto-centrifugally launched, and highly collimated jet from a slow wide-angle magnetic pressure-driven tower flow. As reported in earlier simulations, we found a broad and massive tower flow at early stages of the cloud collapse, though only when using low resolutions. In higher resolution simulations, this massive outflow separates into two distinguishable, temporally and spatially separated components. The magneto-centrifugal jet is active close to the polar axis at early times. Later, the tower flow develops at larger disk radii. In agreement with earlier simulations, we found that the majority of the angular momentum is transported by the tower flow, since it is active at larger radii where more angular momentum is present in the accretion disk. Therefore, we conclude that another mechanism must be available to remove angular momentum before the tower flow has reached its full potential. A very good candidate are gravitational torques, as described by Kuiper et al. [2011].

The convergence study, that varies the size of the sink cells, representing the accreting protostar, shows converged results for sink cell sizes ≤ 3.1 au. For large sink cells, the magnetic field morphology in the jet launching regions deviates significantly from the morphology evolved in simulations with sink cell sizes of ≤ 3.1 au, leading to a much broader magneto-centrifugal outflow that also, due to entrainment, transports much more mass. The resulting wide, and massive outflow partially hinders accretion, and, as a result, these simulations show temporally decreased accretion rates to the protostar. On the other hand, the two simulations with sink cell sizes of 1.0 au and 3.1 au show a close to identical evolution of the magnetic field morphology, resulting in a converged disk, jet, and tower flow system with higher, and potentially more realistic accretion rates.

Our force analyses show that the launching, acceleration, and collimation of the jet component is consistent with the mechanism described by the analytical work of Blandford and Payne [1982]. Similarly, the magnetic tower flow follows the principles of Lynden-Bell [2003]. In addition to these analytical and idealized studies, our cloud collapse simulations include the interaction of the two outflow components with the large-scale infalling stellar environment and provide a temporal dimension that shows a conclusive picture of a cloud-collapse with great dynamic range.

By resolving these high dynamic ranges and the two separate outflow components, we found that the mass outflow rate is dominated by the entrained material from the interaction of the jet with the stellar environment and that only parts of the ejected medium have been directly launched from the accretion disk. Furthermore, accretion as well as ejection are processes that vary in time. Taking into account both the mass that is launched from the disk's surface as well as the entrained material from the envelope, we found an ejection-to-accretion efficiency of 10%, over the whole course of our simulation, as expected by observations.

Jets and outflows in star formation represent a universal process with respect to the basic physics of launching, acceleration, and collimation, and act independently of stellar mass. Massive stars not only possess slow wide-angle tower flows, transporting large amounts of mass, but also produce magneto-centrifugal jets, just as their low-mass counterparts do. As a consequence, the very early evolution of the system acts as a scaled-up version of low-mass star formation, at least with respect to the launching of jets and outflows. The actual significant contrast between low-mass and high-mass star formation lies in the embeddedness of the high-mass star, which implies that the jet and tower flow interact with the infalling large-scale stellar environment. This potentially results in the entrainment of much more mass that additionally leads to visually broader outflows on large scales. According to our results, the original launching mechanisms of these entrained massive outflows could still be

magneto-centrifugal in nature. On the contrary, a magnetic-pressure driven outflow would even be hindered by the massive envelope of massive protostars and can only develop fully when much of the original envelope has already dispersed.
The massive young stellar object in the LMC observed by McLeod et al. [2018] appears to possess exactly such a highly collimated fast magneto-centrifugal jet that we describe here. The reported jet velocities of $300 - 400$ km/s and derived outflow lifetimes of $(28 - 37)$ kyr match our simulations very well. When only considering the magneto-centrifugal jet, i.e. regions with vertical velocities of > 10 km/s, we arrive at average mass outflow rates of 2.15×10^{-6} $M_\odot$ yr^{-1}, which is remarkably close to their estimate of 2.9×10^{-6} $M_\odot$ yr^{-1}.

Chapter 3

Asymmetries in position-velocity-diagrams of protostellar accretion disks

To gain insight, astrophysicist have three approaches at their disposal: observations, simulations and analytic theories. All methods are intertwined and have to work in concert to produce a coherent picture of reality. Nevertheless, this interplay of observation and theory often poses a challenging task. In principle, we expect accretions disks to have nearly symmetric velocity structures relative to the central object. However, there are frequent observations of protostellar accretion disks that show an asymmetry in their position-velocity diagrams, not explainable by asymmetries in their physical velocity structure, caused e.g. by fragmentation. In this chapter, we explain and show that such asymmetries naturally occur from a Doppler-resonance between the accretion disk and the infalling envelope or disk outflows.

3.1 Introduction

Position-velocity-diagrams (pv-diagrams) are a commonly used tool to visualize and reconstruct the observed velocity structure of a wide range of objects. They enable a spatial reconstruction of the three-dimensional velocity structure of the observed object by combining spatial and spectrographic data in one image. Initially, observational raw data contains vast amounts of information that can be processed to gain valuable insights. A typical observation produces a data cube of two spatial and one spectrographic dimension. To reduce this information and to make it more accessible, pv-diagrams are created by slicing a data cube along a line in the observational image, reducing the spatial information to just one dimension. Therefore, pv-diagrams show the position along a slice of observational data on one axis and the velocity along the line of sight on the other axis, provided by spectrographic data. This makes them very versatile as one can choose the line along which to slice the data and the molecular line to visualize different physical phenomena. A particularly insightful application of pv-diagrams is the analysis of accretion disks. Physically, they are expected to be symmetrical w.r.t. the central object, but their pv-diagrams often exhibit asymmetries. We compiled a list of examples showing such asymmetries. Observations of AFGL 4176 by

Johnston et al. [2015, Fig. 4, panels (a) to (c)] and of G35.03+0.35 by Beltrán et al. [2014, Fig. 18, panels (a) and (c)] show a higher emission on the blue than on the red shifted sides of their pv-diagrams. Observations of NGC 6334 by Hunter et al. [2014, Fig. 11, third panel on the left], on the other hand, show a higher emission on the red than on the blue shifted sides of their pv-diagrams. Observations of IRAS 20126+4104, taken by Cesaroni et al. [2014], even show the peak shifting between the red and blue depending on the line of CH_3CN considered. While for the lower excitation levels $K = 2, K = 3, K = 4$ the higher emission is detected on the blue shifted side, for $K = 8$ it is on the red shifted side. We propose that these asymmetries naturally arise when not only emission but also resonant absorption is considered and for objects embedded in large-scale infalling or outflowing regions, i.e. for cases with sufficiently high optical depth in the outer regions around the embedded disks.
Subsequently, we will first describe the pivotal principle that gives rise to these asymmetries in such accretion disks. It is found in Sec. 3.2. Ohashi et al. [1997] show a simple, yet insightful, and frequently cited, model of the pv-diagram of an accretion disk in their appendix. Since it is so well renowned, it also provides the starting point of our analysis, the details of which are discussed in Sec. 3.3. After that, our results are described in Sec. 3.4, concluding with a summary in Sec. 3.5.

3.2 Hypothesis

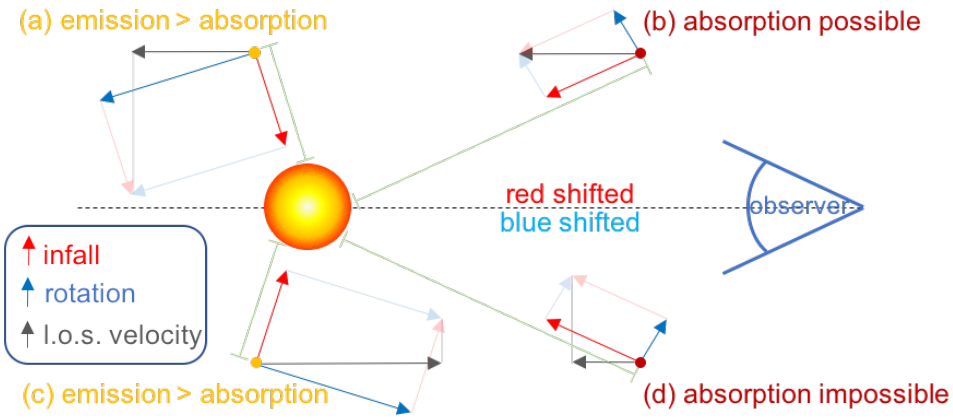

Figure 3.1: The principle of spectroscopic resonance between infall and rotation.

A possible explanation for these asymmetries is the hypothesis presented in this section, and diagrammed in Fig. 3.1. In the following description, we will first focus on the case with higher emissions from the blue-shifted parts that is produced by a resonance between a rotating accretion disk and an infalling envelope. Still, the same kind of resonance also appears for higher emissions from the red-shifted side, considering an outflow instead of an infall. The principle idea is that particles rotating close to the central object in an accretion disk can reach the same line of sight velocity w.r.t. the observer as primarily infalling particles at larger distances. Consequently, their spectra are Doppler-shifted by the same amount at both positions, and photons emitted at a more distant position can be reabsorbed closer to the observer. Most importantly, the source function at the point along the beam where the line-of-sight velocity is reached the last time before arriving at the observer has to be lower

than at the point where the velocity was reached previously, in order for a detectable absorption. This reabsorption by resonances of molecular lines can, therefore, be considered a special case of self-absorption.
As a prerequisite, in the regions responsible for the initial emission, the rotational and infall velocities have to be of a similar magnitude as indicated by Fig. 3.1. A situation where a visible, flattened, and infalling envelope is still present potentially belongs to a relatively early evolutionary stage. Accordingly, we expect such asymmetries with more intense blue-shifted radiation to occur predominantly in very young sources, as it is crucial that these outer, colder envelope regions are still dense enough to have a significant optical depth. Under these requirements, consider molecules in close rotation to the protostar e.g. at location (a) in Fig. 3.1. The characteristic emission from these molecules is red-shifted by a frequency corresponding to their line-of-sight velocity. If this exact line-of-sight velocity is again reached by molecules at another optically relevant region, e.g. at location (b), the radiation can be reabsorbed. Depending on the exact details of the profiles of rotational and infall velocities as well as the source function, arguably more radiation of this frequency is emitted from the hot inner accretion disk at location (a) than is emitted in the cold outer regions of the envelope by molecules at location (b). Therefore, when this resonance occurs, it reduces the intensity of the Doppler-shifted line detected by the observer. At location (c), i.e. the mirror-image of location (a) on the blue-shifted side of the disk, the rotation and infall velocities are equal to location (a), but the rotational component along the line of sight points in the opposite direction, and, as a result, the particle at location (c) has a relatively high line-of-sight velocity towards the observer. In this example, consequently, there are no molecules at a location (d) (or any other location between the intensly radiating molecules in the hot accretion disk and the observer) that reach similar line-of-sight velocities towards the observer. For that reason, the re-absorption found on the red-shifted side does not appear on the blue-shifted side. As a result, the observer receives more emission of this line at the corresponding Doppler-shift from the blue-shifted side than from the red-shifted side.
The same idea can be applied for a resonance between the rotation of an accretion disk and outflow velocities of equal magnitude. In this case, the principal radial velocities as indicated in Fig. 3.1 have to be inverted. This shifts the resonance of emission and absorption to the blue-shifted side, resulting in the observer to receive more emission from the red-shifted part.

Source	Outflow	Reference
NGC 6334 I (N) SMA 1 (b)	SiO outflow	Hunter et al. [2014], Fig. 8
AFGL4176	CO outflow	Johnston et al. [2015], Fig. 2
IRAS23151 + 5912	CO outflow	Beuther et al. [2007], Fig. 1
G35 .03 + 0.35 HMC A	CO outflow	Beltrán et al. [2014] Fig. 10
IRAS 20126 + 4104	HCO+ outflow	Cesaroni et al. [2014], Fig. 7
G 11.92 - 0.61 MM1	CO outflow	Ilee et al. [2016], Fig. 1

Table 3.1: Table with observed outflows and asymmetric pv-diagrams.

This principle neatly fits into the notice that e.g. in Cesaroni et al. [2014]'s observations, the higher emission shifts from the blue-shifted side to the red-shifted side for higher excitation lines of CH_3CN, since we would expect an outflow on the surface of an accretion disk to show much stronger emissions from higher excitations as it receives significantly more intense radiation from the protostar and, consequently, also reaches much higher average excitation

levels than the radiatively shielded part of the disk. Therefore, we should see hints to outflow structures in sources with this kind of asymmetry and, indeed, all these sources show signs of outflows as summarized in table 3.1.
To explore this idea further, and see the quantitative effect of these asymmetries in pv-diagrams, we developed an easily comprehensible radiative transfer code that is displayed and applied in the following.

3.3 Methods

We employ a two-dimensional spatial grid spanning $\simeq$ 8000 au in each dimension with the protostar at the origin with a cell size of 50 au $\times$ 50 au. Spectrally, we use a grid corresponding to relative velocities spanning from -6 km/s to 6 km/s with a spectral resolution of 0.2 km/s. Although we have conducted such calculations for several molecules, here we present the results obtained for CH_3CN, since observations frequently show similar asymmetries in its lines. However, it is worth noting that we were able to reproduce similar asymmetries for CH_3OH and there is no reason why other molecules should not show such asymmetries, as long as they are abundant and emissive enough.
As mentioned, the starting point of our analysis is the simple model by Ohashi et al. [1997]. They show a thin accretion disk of 2000 au radius and analyze its edge-on pv-diagram, considering both infall and rotational velocities. For the rotational velocity, they show two models: one with a Keplerian velocity profile, and, consequently, no infall velocity and a model with an infall velocity profile $v_{\mathrm{inf}} \propto r^{-1/2}$ and a momentum conserving rotational velocity profile $v_{\mathrm{rot}} \propto r^{-1}$. Here, we focus on the second model. To summarize their approach, they use the following configuration:

$$v_{\mathrm{inf}} = \sqrt{\frac{2GM_\star}{r}} \tag{3.1}$$

$$v_{\mathrm{rot}} = \frac{v_0 r_{\mathrm{d}}}{r}\,, \tag{3.2}$$

where they take a disk radius r_{d} of 2000 au and vary the initial rotational velocity v_0. To accompany this velocity profile, they assume a disk surface density of $\Sigma \propto r^{-1.5}$ and take a (pre-)stellar mass of $M_\star = 0.1\ \mathrm{M}_\odot$. Most importantly, they assume that the brightness temperature is proportional to the disk column density along the line of sight. This is a very reasonable first assumption, though it is also the reason why their model cannot explain asymmetries and why we examine their model again.
These parameters result in the pv-diagrams shown in Fig. 10 of Ohashi et al. [1997]. The lower right panel there shows the typical butterfly-like shape of the pv-diagram with high intensities of relatively fast moving particles in the center and slower moving gas on the outer rim of the disk. This simple model can already be compared to many observations that show a somewhat similar picture. However, there is a feature often observed that cannot be explained using this model alone: asymmetries between the red and blue-shifted sides of the pv-diagrams.
The crucial difference to Ohashi et al. [1997] is that we simulate a relatively massive, optically dense disk of a forming higher mass protostar. This means we use a similar velocity profile to Ohashi et al. [1997], since it matches the observations well, but otherwise we use parameters

expected for much more massive protostars. Consequently, our central object has a temperature of 35000 K and a radius of $7R_\odot$. Similarly to Ohashi et al. [1997], we use a density distribution $\propto r^{-1.5}$. Though, a more massive central object is also expected to have a much more massive disk. Therefore, we use a significantly higher density of $\rho_0 = 2.5 \cdot 10^{-17}$ at the reference radius of $r_0 = 2000$ au which results in

$$\rho(r) = \rho_0 \left(\frac{r}{r_0}\right)^{-1.5} . \tag{3.3}$$

We assume that the abundance of emitting molecules is proportional to this density, with an abundance of 10^{-9} w.r.t. the abundance of hydrogen. For the stellar spectrum, we simply assume a black body with its total flux $I_\star$ proportional to the Planck function

$$I_\star(\nu) = \pi \frac{2h\nu^3}{c^2} \frac{1}{e^{h\nu/k_\mathrm{B}T} - 1} . \tag{3.4}$$

For the source function S at a given radius, we assume that it is proportional to the fraction of the sky subtended by the central star as seen by the emitting particle

$$S(\nu, r) = \frac{I_\star(\nu)}{2} \left(1 - \sqrt{1 - \frac{R_\star}{r}}\right)^2 . \tag{3.5}$$

While this is only an approximate source function, it is a reasonable approximation. Obtaining the real source function would have to be done by a more complicated, iterative process. See Kee et al. [2018] for more information. We reduce the source function in the central $\simeq 500$ au, due to the high dust densities that make these regions fairly opaque. This choice is motivated by analysis of observations, for instance Beuther et al. [2017] who state that "The hole in the center of the map is caused by the absorption against the strong continuum…". To model this effect, we multiply the source function by

$$1 - 0.5 f_\mathrm{err} \left(\frac{r - 400\ \mathrm{au}}{100\ \mathrm{au}}\right) \tag{3.6}$$

with the complementary error function

$$f_\mathrm{err}(x) = 1 - \frac{2}{\sqrt{\pi}} \int_0^x e^{-t^2} dt , \tag{3.7}$$

in order to reduce emission in the central 500 au.
To calculate the opacities, we take the levels, transitions, and statistical weights from the Leiden database and calculate from that the partition function and populations, assuming a temperature profile of

$$T(r) = \left(10 \left(\frac{r}{r_0}\right)^{-2} + 100\right) \mathrm{K} . \tag{3.8}$$

The resulting line opacities α_{ij} are then given by

$$\alpha_{ij}(\nu) = \frac{h\nu_{ij}}{4\pi} (n_j B_{ji} - n_i B_{ij}) \phi_{ij}(\nu) , \tag{3.9}$$

where B_{ij} is the Einstein B-coefficient for extinction, B_{ji} is the Einstein B-coefficient for stimulated emission, and n_i and n_j are the corresponding populations. $\phi_{ij}(\nu)$ is the line profile function. Here, we assume a Gaussian profile with the width ς, assumed to be the thermal velocity of the particles, resulting in

$$\phi(\nu)_{ij} = \frac{1}{\varsigma(T)\sqrt{\pi}} e^{-\left(\frac{\nu-\nu_{ij}}{\varsigma}\right)^2} . \tag{3.10}$$

For the velocities, we stick to the setup of Ohashi et al. [1997] and assume a rotational velocity that is based on angular momentum conservation

$$v_\phi = v_{\phi\,0} \left(\frac{r}{r_0}\right)^{-1} \tag{3.11}$$

with $v_{\phi\,0} = 0.5$ km/s. For the infall velocity, we assume that the disk is not yet in a stable equilibrium, though significantly slowed down by centrifugal, magnetic and radiative forces. Therefore, we do not use the full free-fall velocity but a slower infall profile of

$$v_\mathrm{r} = -v_{\mathrm{r}\,0} \left(\frac{r}{r_0}\right)^{-0.5} , \tag{3.12}$$

with $v_{\mathrm{r}\,0} = 0.75$ km/s.
With these parameters, the calculation uses the Sobolev plus exact integration method [Lamers et al., 1987], which assumes that the emission and absorption properties are purely local, or more physically, that the projected width of the profile function is small with respect to the variations of density and source function. During the numerical integration, each photon package is advanced from a cell at a larger distance x_{i+1} to a cell at a closer distance x_i via

$$I(\nu, x_i, y_j) = \left(1 - e^{-\Delta\tau}\right) S\left(\nu, r(x_i, y_i)\right) + I(\nu, x_{i+1}, y_j) e^{-\Delta\tau} , \tag{3.13}$$

here x denotes the coordinate along the line of sight and y the coordinate perpendicular to the line of sight. Subsequently, the results of our application of this scheme are discussed.

3.4 Results

To test our initial setup, we aim to reproduce a similar and, most importantly, symmetric pv-diagram as shown in Ohashi et al. [1997]. To this end, we remove the possibility of absorption from the radiation transport algorithm, i.e. we replace Eq. (3.13) by

$$I(\nu, x_i, y_j) = \left(1 - e^{-\Delta\tau}\right) S\left(\nu, r(x_i, y_i)\right) + I(\nu, x_{i+1}, y_j) . \tag{3.14}$$

While we use a slightly more elaborate algorithm to generate it, this still produces a symmetric pv-diagram similar to the one obtained by Ohashi et al. [1997], as the combination of infall and rotation produces a pv-diagram with the expected butterfly-like shape, as visible in Fig. 3.2. Also similar to Ohashi et al. [1997]'s approach, we smooth the image along the disk (i.e. the y-direction), by averaging over a number of neighboring cells corresponding to a resolution of 250 au. More realistic than this case, however, is a setup that allows absorption. In the next sections, we explore two such cases: first, the combination of an accretion disk with an infalling envelope, followed by a setup combining an accretion disk with an outflow.

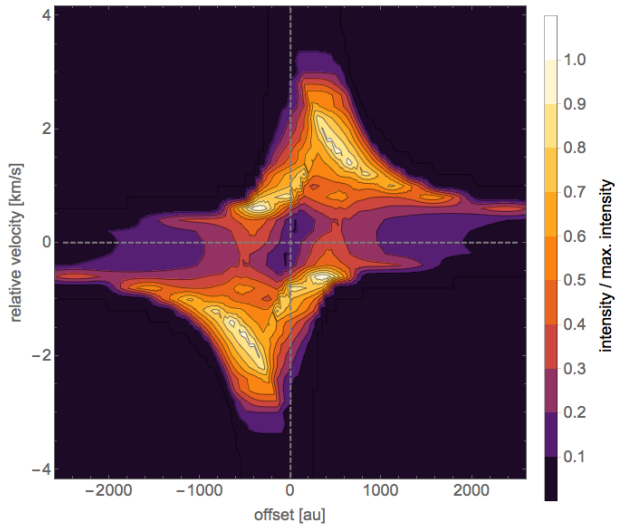

Figure 3.2: Position-velocity-diagram for the disk-infall case neglecting resonant absorption.

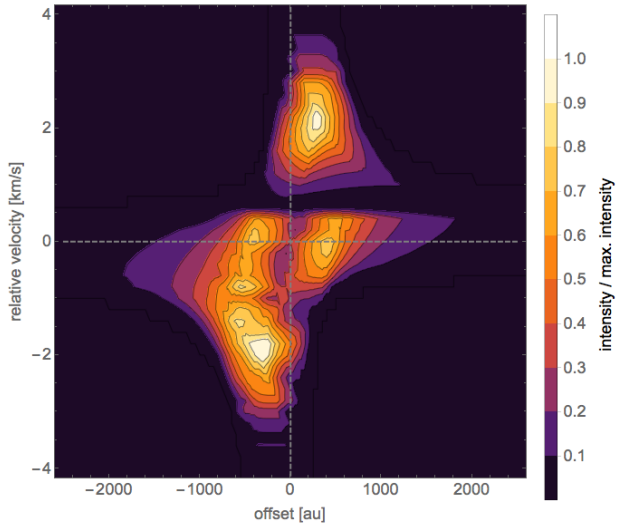

Figure 3.3: Position-velocity-diagram for the disk-infall case including resonant absorption.

3.4.1 Infall case

Continuing in the same manner, but including absorption in the algorithm, we arrive at the pv-diagram shown in Fig. 3.3. It is worth noting that between both pv-diagrams, no other parameters were modified. However, including the absorption has a very significant effect. Most importantly, the pv-diagram has become asymmetric, with higher intensities coming from the blue-shifted side of the accretion disk. To see how these asymmetries arise, we can follow rays on both sides of the disk/envelope-system, and analyze where the emission and absorption respectively happen. The probably most important prerequisite for obtaining such asymmetries is that infalling and rotational velocities have similar magnitudes, such that both contribute similarly to the resulting line-of-sight velocities and, as a result, overlap in frequency space. In Fig. 3.4, we present a plot of the resulting line-of-sight velocities plotted in a face-on view on the disk. The observer is placed in the negative x-direction and the

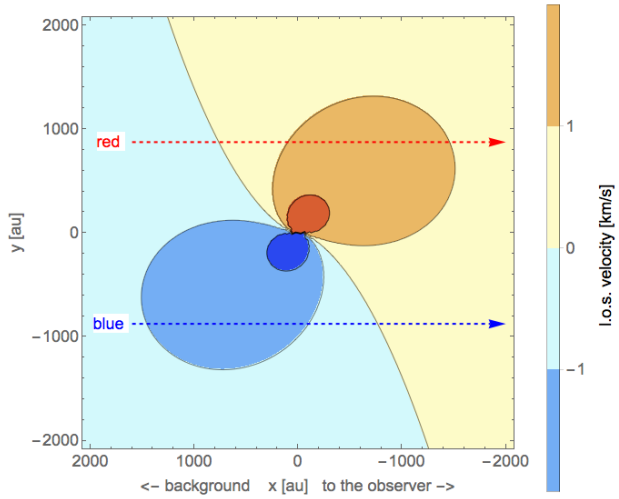

Figure 3.4: A face-on view on the accretion disk, showing the line-of-sight velocity. The arrows indicate the rays that we follow in the remaining plots. Here, the observer is positioned at negative values of x and the pv-diagram is made close to edge-on, where y is the position along the accretion disk where the velocities are measured.

pv-diagram is produced by scanning the disk edge-on, i.e. here in the y-direction. For the demonstration, we chose a frequency corresponding to a Doppler-shift of ±1 km/s, and a location at an offset of ±875 au from the central host star. In Fig. 3.4, we can clearly see that these rays of light cross the l.o.s. velocity contour of ±1 km/s two times, such that emission and reabsorption is possible near (due to thermal broadening) the crossing points.

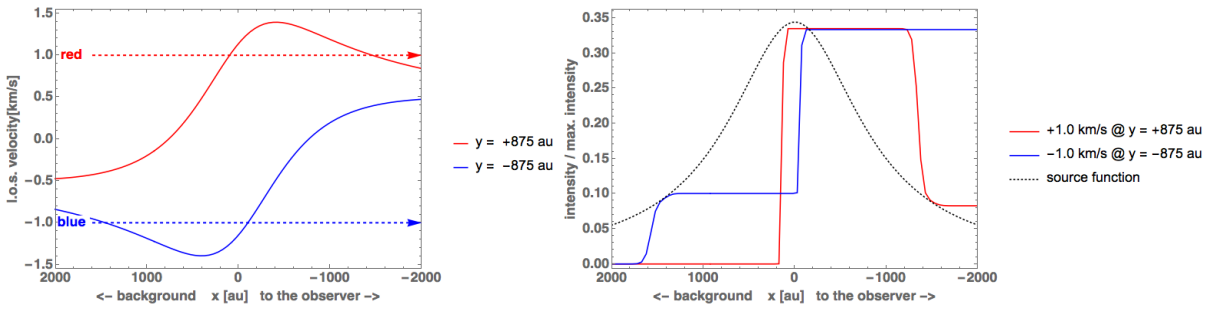

(a) Line-of-sight velocity.

(b) Intensity.

Figure 3.5: Line-of-sight velocities and intensities resulting from emission and absorption along rays on the red and blue-shifted side, when traversing a rotating disk and infalling envelope.

This is also reflected in Fig. 3.5a, where we can see the exact position where the rays cross regions with these line-of-sight velocity and in Fig. 3.5b, where we can see the intensity of these frequencies along the ray as it traverses the accretion disk and the envelope compared to the local source function. There it becomes obvious why there has to be an asymmetry. Following the rays from the left-hand side to the right-hand side, the ray on the red-shifted side first crosses regions with line-of-sight velocities of 1 km/s close to the origin, with high emissivities and crosses again in colder regions where this radiation is then reabsorbed. The opposite happens for the ray on the blue-shifted side. It first travels through cool

low-emissivity regions and afterwards reaches the point in the disk opposite to the point where the red ray gets its initial emission, such that the total intensity rises to the same value, though without the possibility to be reabsorbed.

3.4.2 Outflow case

Similarly, an asymmetry with higher emission from the red-shifted side can be achieved when instead of assuming infall, one assumes a wind above the surface of the accretion disk and into the envelope. This situation would we visible when observing at higher angles with respect to the accretion disk. For example, a slow magnetic pressure-driven tower flow, as present in the simulations in chapter 2, could accelerate material with relatively slow velocities towards the observer. To demonstrate this point, we use the same model as discussed above with a single

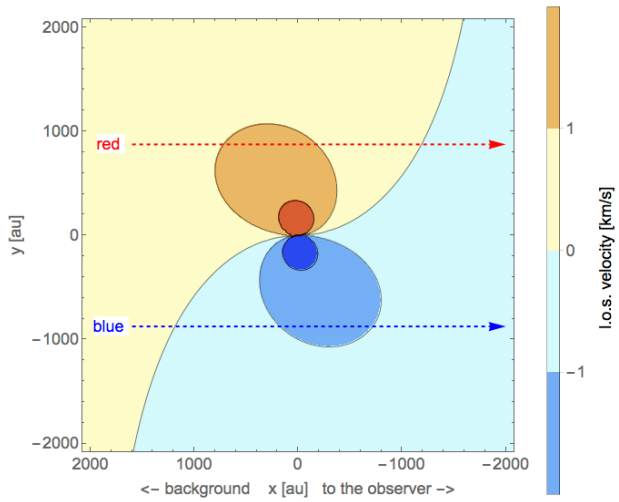

Figure 3.6: Line-of-sight velocity in a top-down view on the accretion disk for a rotating disk and a slow disk wind.

modification: a constant outward radial velocity of 0.5 km/s instead of an infall. With that, we arrive at the line-of-sight velocity in the accretion disk-outflow model presented in Fig. 3.6. As we can see here, we expect the absorption now to occur on the blue-shifted side. Indeed, we could repeat our discussion above for the following plots of the line-of-sight velocity along the ray in Fig. 3.7a and the resulting emission and absorption visible in the intensity evolution along the rays in Fig. 3.7b that validate this expectation.
Also, the concluding pv-diagram in Fig. 3.8 is quite similar to observed pv-diagrams [e.g. Johnston et al., 2015, Fig. 2].
Such an outflow also explains asymmetries that shift from having higher emissions on the blue-shifted side to having higher emissions from the red-shifted side for higher excitations, as observed by Cesaroni et al. [2014, Fig.7]. The reasoning is that outflows typically have a strong density contrast to the accretion disk. This also makes them less opaque. Therefore, radiation from the star can penetrate them and lead to higher average excitation levels even at relatively large radii. Effects such as shock heating would contribute to that as well. As a result, we would expect higher concentrations of higher excited species in the outflowing parts

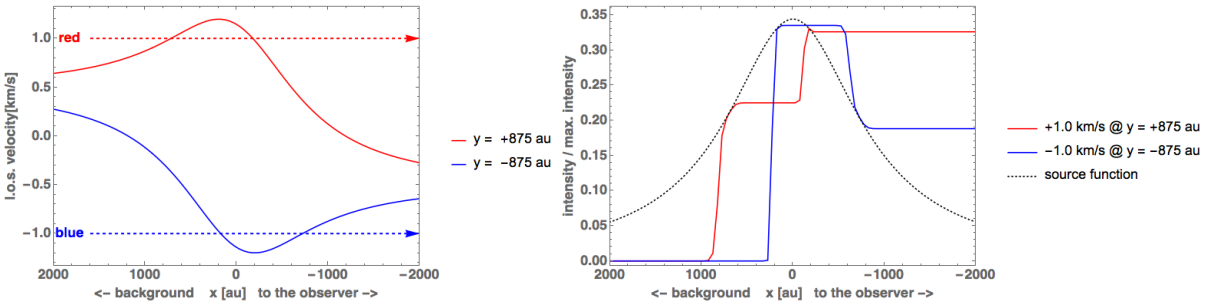

(a) Line-of-sight velocity. (b) Intensity.

Figure 3.7: Line-of-sight velocities and intensities resulting from emission and absorption along rays on the red and blue-shifted side, when traversing a disk/outflow structure.

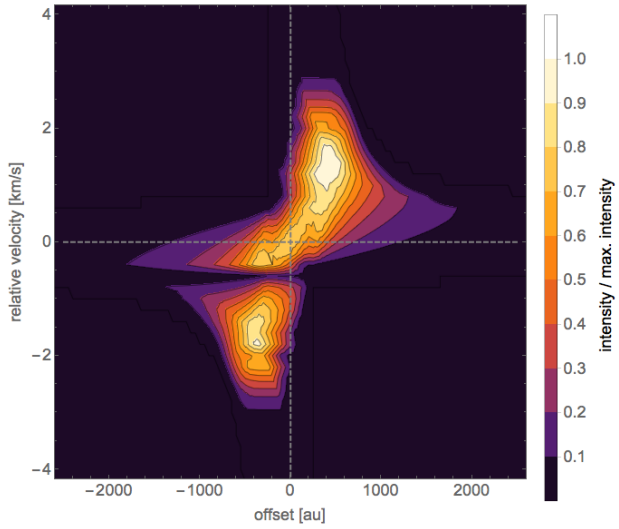

Figure 3.8: Position-velocity-diagram for the disk-outflow case.

of the object, which would result in higher emissions from the red-shifted side in the corresponding lines.

3.5 Summary

Asymmetries in position-velocity diagrams are commonly observed. As we have shown here, they can arise naturally from a resonance between rotation and infall (or outflow) velocities found in accretion disks around young stellar objects, when the emission from the central, warmer part of the accretion disk is reabsorbed in outer, colder parts, where similar line-of-sight velocities are reached. The effect explains higher emissions from the blue-shifted side as a resonance between infall and rotation, and higher emissions from the red-shifted side as a resonance between an outflow and the rotation of the disk. The nature of this effect can be seen as a special case of self-absorption by molecular lines.
We expect that young objects with dense infalling envelopes can exhibit higher blue-shifted emission via this mechanism. On the other hand, higher red-shifted emission could be found in any source that has a jet, outflow or disk wind with velocities comparable to its rotational velocity. Therefore, this asymmetry could occur in a wide range of evolutionary stages. Consequently, a shift depending on the excitation level from the blue shift dominated to the red shift dominated asymmetry would probably be bound to objects that have a dense infalling envelope and at the same time possess winds.

Appendices

Appendix A

Symbols

symbol	description
A	area
α_{ij}	line opacity
$\vec{B}$	total magnetic field vector
B_{ij}	Einstein B-coefficient
c	light-speed
$\frac{D}{Dt}$	comoving (Lagrangian) derivative
Δx	resolution
$\vec{E}$	electric field
ϵ	total internal specific energy
η	magnetic diffusivity
η_{visc}	coefficient of shear viscosity
$\mathbf{F}$	combined flux tensor
f_{err}	complementary error function
F_{ext}	external forces
F_{g}	gravitational force
F_{L}	Lorentz force
F_{vis}	radiative flux in the visual band
Φ	total magnetic flux
φ	azimuthal angle
ϕ_{ij}	line profile function
G	gravitational constant
γ	adiabatic index
h	Planck constant
$I_\star$	total radiative flux of a (proto)star
j	emission coefficient
$\vec{j}$	electric current
k_{B}	Boltzmann constant
κ_{dust}	dust opacity
L	luminosity
$\vec{L}$	angular momentum

symbol	description
$\bar{l}$	typical length scale
L_{Edd}	Eddington-luminosity
M	total mass
$M_\star$	(proto)stellar mass
M_{A}	Alfvén Mach Number
m_{H}	mass of atomic hydrogen
M_{J}	Jeans mass
M_{vis}	absolute magnitude in the visual band
μ	molecular mass
$\bar{\mu}$	mass-to-flux ratio
n	number density
n_i	level population
ν	frequency
p	pressure
$\mathbf{Q}$	combined vector of hydrodynamic quantities
r	radius (depending on context spherical or cylindrical)
$R_\star$	(proto)stellar radius
r_0	reference radius
r_{c}	radius of curvature
r_{d}	disk radius
r_{sink}	sink cell radius
Re	Reynolds number
ρ	density
S	source function
σ	electric charge density
ς	width of the line profile function
σ_{B}	Stefan-Boltzmann constant
σ_{visc}	viscous stress tensor
T	temperature
t	time
T_{eff}	effective black-body temperature
t_{ff}	free-fall time
t_{KH}	Kelvin-Helmholtz-time
ϑ	polar angle
τ	optical depth
V	potential
V_{grav}	gravitational potential
$\mathbf{V}$	vector of velocities
$\vec{v}$	velocity
v	absolute value of the velocity
$\bar{v}$	typical velocity
$\vec{v}_{\mathrm{A}}$	Alfvén velocity
$\vec{v}_{\mathrm{AD}}$	ambipolar diffusion drift
$\vec{v}_{\mathrm{e}}$	electron velocity
$\vec{v}_{\mathrm{H}}$	Hall drift

symbol	description
$\vec{v}_\mathrm{i}$	ion velocity
X_e	ionization degree
ξ	absorption coefficient
x	coordinate along the line of sight
y	coordinate perpendicular to the line of sight
z	altitude above the equatorial plane

Appendix B

Abbreviations

abbreviation	description
AMR	adaptive mesh refinement
CMF	core mass function
e.g.	exempli grata (for example)
eos	equation of state
GMC	giant molecular cloud
HR	Hertzsprung-Russel, as in the Hertzsprung-Russel diagram
i.e.	id est (that is)
IMF	initial mass function
ISM	interstellar matter medium
LMC	Large Magellanic Cloud
MHD	magneto-hydrodynamics
PDE	partial differential equation
w.r.t.	with respect to

Bibliography

V. Agra-Amboage, C. Dougados, S. Cabrit, P. J. V. Garcia, and P. Ferruit. [O I] sub-arcsecond study of a microjet from an intermediate mass young star: RY Tauri. *A&A*, 493(3): 1029–1041, 2009.

M. Audard, P. Ábrahám, M. M. Dunham, J. D. Green, N. Grosso, K. Hamaguchi, J. H. Kastner, A. Kóspál, G. Lodato, M. Romanova, S. L. Skinner, E. I. Vorobyov, and Z. Zhu. Episodic Accretion in Young Stars. *Protostars Planets VI*, pages 387–410, 2014.

S. A. Balbus and J. F. Hawley. A Powerful Local Shear Instability in Weakly Magnetized Disks. I. Linear Analysis. *ApJ*, 376:20, 1991.

R. Banerjee and R. E. Pudritz. Massive star formation via high accretion rates and early disk-driven outflows. *ApJ*, 660(1):479, 2007.

M. R. Bate, T. S. Tricco, and D. J. Price. Collapse of a molecular cloud core to stellar densities: Stellar-core and outflow formation in radiation magnetohydrodynamic simulations. *MNRAS*, 437(1):77–95, 2014.

M. T. Beltrán, a. Sánchez-Monge, R. Cesaroni, M. S. N. Kumar, D. Galli, C. M. Walmsley, S. Etoka, R. S. Furuya, L. Moscadelli, T. Stanke, F. F. S. van der Tak, S. Vig, K.-S. Wang, H. Zinnecker, D. Elia, and E. Schisano. Filamentary structure and Keplerian rotation in the high-mass star-forming region G35.03+0.35 imaged with ALMA. *A&A*, 571:A52, 2014.

H. Beuther, Q. Zhang, T. R. Hunter, T. K. Sridharan, and E. A. Bergin. The 10^5 $L_\odot$ high-mass protostellar object IRAS 23151+5912. *A&A*, 473(2):493–500, 2007.

H. Beuther, A. Ahmadi, J. Mottram, F. Bosco, H. Linz, and P. Klaassen. CORE: Fragmentation and disk formation in high-mass star formation. *Mem. S.A.It.*, 88(584):3, 2017.

R. D. Blandford and D. G. Payne. Hydromagnetic flows from accretion discs and the production of radio jets. *MNRAS*, 199:883–903, 1982.

I. A. Bonnell, M. R. Bate, C. J. Clarke, and J. E. Pringle. Competitive accretion in embedded stellar clusters. *MNRAS*, 323(4):785–794, 2001.

S. Cabrit, C. Codella, F. Gueth, B. Nisini, A. Gusdorf, C. Dougados, and F. Bacciotti. PdBI sub-arcsecond study of the SiO microjet in HH212: Origin and collimation of class 0 jets. *A&A*, 468(3):L29–L32, 2007.

A. Caratti o Garatti, R. Garcia Lopez, S. Antoniucci, B. Nisini, T. Giannini, J. Eislöffel, T. P. Ray, D. Lorenzetti, and S. Cabrit. POISSON project: II. A multi-wavelength spectroscopic and photometric survey of young protostars in L 1641. *A&A*, 538:A64, 2012.

A. Caratti o Garatti, B. Stecklum, G. Weigelt, D. Schertl, K.-H. Hofmann, S. Kraus, R. D. Oudmaijer, W. J. de Wit, A. Sanna, R. Garcia Lopez, A. Kreplin, and T. P. Ray. Tracing jet emission at the base of a high-mass YSO: First AMBER/VLTI observations of the Br γ emission in IRAS 13481-6124. *A&A*, 589:L4, 2016.

R. Cesaroni, D. Galli, R. Neri, and C. M. Walmsley. Imaging the disk around IRAS 20126+4104 at subarcsecond resolution. *A&A*, 566:A73, 2014.

B. Commerçon, P. Hennebelle, and T. Henning. Collapse of Massive Magnetized Dense Cores Using Radiation Magnetohydrodynamics: Early Fragmentation Inhibition. *ApJ*, 742(1):L9, 2011.

R. Courant, K. Friedrichs, and H. Lewyt. On the Partial Difference Equations of Mathematical Physics. *Math. Ann.*, 100:20, 1928.

L. E. Ellerbroek, L. Podio, L. Kaper, H. Sana, D. Huppenkothen, A. de Koter, and L. Monaco. The outflow history of two Herbig-Haro jets in RCW 36: HH 1042 and HH 1043. *A&A*, 551:A5, 2013.

N. J. Evans, M. M. Dunham, J. K. Jørgensen, M. L. Enoch, B. Merín, E. F. van Dishoeck, J. M. Alcalá, P. C. Myers, K. R. Stapelfeldt, T. L. Huard, L. E. Allen, P. M. Harvey, T. van Kempen, G. A. Blake, D. W. Koerner, L. G. Mundy, D. L. Padgett, and A. I. Sargent. The Spitzer C2d Legacy Results: Star-Formation Rates and Efficiencies; Evolution and Lifetimes. *ApJS*, 181(2):321–350, 2009.

Frank, Ray, H. G. Arce, F. Bacciotti, J. Bally, M. Benisty, J. Eislöffel, M. Güdel, S. Lebdev, B. Nisini, and A. Raga. Jets and Outflows From Star to Cloud Observations Confront Theory. In *Protostars and Planets VI*. University of Arizona Press, Tucson SN, 2014.

P. Hennebelle and S. Fromang. Magnetic processes in a collapsing dense core. *A&A*, 477: 9–24, 2008.

P. Hennebelle, B. Commerçon, M. Joos, R. S. Klessen, M. Krumholz, J. C. Tan, and R. Teyssier. Collapse, outflows and fragmentation of massive, turbulent and magnetized prestellar barotropic cores. *A&A*, 528:A72, 2011.

T. R. Hunter, C. L. Brogan, C. J. Cyganowski, and K. H. Young. Subarcsecond imaging of the ngc 6334 i(n) protocluster: Two dozen compact sources and a massive disk candidate. *ApJ*, 788(2):187, 2014.

J. D. Ilee, C. J. Cyganowski, P. Nazari, T. R. Hunter, C. L. Brogan, D. H. Forgan, and Q. Zhang. G11.92-0.61 MM1: A Keplerian disc around a massive young proto-O star. *MNRAS*, 462(4):4386–4401, 2016.

K. G. Johnston, T. P. Robitaille, H. Beuther, H. Linz, P. Boley, R. Kuiper, E. Keto, M. G. Hoare, and R. van Boekel. A Keplerian-Like Disk Around the Forming O-Type Star Afgl 4176. *ApJ*, 813(1):L19, 2015.

N. D. Kee, S. Owocki, and J. O. Sundqvist. Line-driven ablation of circumstellar discs - I. Optically thin decretion discs of classical Oe/Be stars. *MNRAS*, 458:2323–2335, 2016.

N. D. Kee, S. Owocki, and R. Kuiper. Line-driven ablation of circumstellar discs – II. Analysing the role of multiple resonances. *MNRAS*, 474(1):847–853, 2018.

M. R. Krumholz and C. F. McKee. A minimum column density of 1 g cm-2 for massive star formation. *Nature*, 451:1082, 2008.

R. Kuiper and T. Hosokawa. First hydrodynamics simulations of radiation forces and photoionization feedback in massive star formation. *ArXiv180410211 Astro-Ph*, 2018.

R. Kuiper, H. Klahr, H. Beuther, and T. Henning. Circumventing the Radiation Pressure Barrier in the Formation of Massive Stars Via Disk Accretion. *ApJ*, 722(2):1556–1576, 2010.

R. Kuiper, H. Klahr, H. Beuther, and T. Henning. Three-Dimensional Simulation of Massive Star Formation in the Disk Accretion Scenario. *ApJ*, 732(1):20, 2011.

M. W. Kunz and T. C. Mouschovias. The initial core mass function due to ambipolar diffusion in molecular clouds. *MNRAS*, 399(1):L94–L98, 2009.

H. Lamers, M. Cerruti-Sola, and M. Perinotto. The'SEI'method for accurate and efficient calculations of line profiles in spherically symmetric stellar winds. *ApJ*, 314:726–738, 1987.

R. B. Larson. Numerical Calculations of the Dynamics of a Collapsing Proto-Star. *MNRAS*, 145(3):271–295, 1969.

R. V. E. Lovelace, M. M. Romanova, and G. S. Bisnovatyi-Kogan. Spin-up/spin-down of magnetized stars with accretion discs and outflows. *MNRAS*, 275(2):244–254, 1995.

D. Lynden-Bell. On why discs generate magnetic towers and collimate jets. *MNRAS*, 341: 1360–1372, 2003.

M. N. Machida and T. Hosokawa. Evolution of protostellar outflow around low-mass protostar. *MNRAS*, 431(2):1719–1744, 2013.

M. N. Machida, S.-i. Inutsuka, and T. Matsumoto. Magnetic Fields and Rotations of Protostars. *ApJ*, 670:1198–1213, 2007.

M. N. Machida, S.-i. Inutsuka, and T. Matsumoto. High- and Low-Velocity Magnetized Outflows in the Star Formation Process in a Gravitationally Coll. *ApJ*, 676:1088–1108, 2008.

M. N. Machida, S.-i. Inutsuka, and T. Matsumoto. Conditions for circumstellar disc formation: Effects of initial cloud configuration and sink treatment. *MNRAS*, 438(3):2278–2306, 2014.

Y. Matsushita, M. N. Machida, Y. Sakurai, and T. Hosokawa. Massive outflows driven by magnetic effects in star-forming clouds with high mass accretion rates. *MNRAS*, 470(1): 1026–1049, 2017.

A. F. McLeod, M. Reiter, R. Kuiper, P. D. Klaassen, and C. J. Evans. A parsec-scale optical jet from a massive young star in the Large Magellanic Cloud. *Nature*, 554(7692):334–336, 2018.

L. Mestel. Problems of Star Formation - I. *QJRAS*, 6:161, 1965.

D. M.-A. Meyer, E. I. Vorobyov, R. Kuiper, and W. Kley. On the existence of accretion-driven bursts in massive star formation. *MNRAS*, 464(1):L90–L94, 2017.

D. M.-A. Meyer, R. Kuiper, W. Kley, K. G. Johnston, and E. Vorobyov. Forming spectroscopic massive protobinaries by disc fragmentation. *MNRAS*, 473(3):3615–3637, 2018.

A. Mignone, G. Bodo, S. Massaglia, T. Matsakos, O. Tesileanu, C. Zanni, and A. Ferrari. PLUTO: A Numerical Code for Computational Astrophysics. *APJS*, 170:228–242, 2007.

A. T. Myers, R. I. Klein, M. R. Krumholz, and C. F. McKee. Star cluster formation in turbulent, magnetized dense clumps with radiative and outflow feedback. *MNRAS*, 439(4): 3420–3438, 2014.

T. Nakano. The Behavior of Magnetic Fields in Star Forming Regions. In *Galactic and Extragalactic Star Formation*, pages 111–133. Springer, Dordrecht, 1988.

T. Nakano. Conditions for the formation of massive stars through nonspherical accretion. *ApJ*, 345:464, Oct. 1989.

T. Nakano, R. Nishi, and T. Umebayashi. Mechanism of Magnetic Flux Loss in Molecular Clouds. *ApJ*, 573:199–214, 2002.

S. S. R. Offner, P. C. Clark, P. Hennebelle, N. Bastian, M. R. Bate, P. F. Hopkins, E. Moreaux, and A. P. Whitworth. The Origin and Universality of the Stellar Initial Mass Function. In *Protostars and Planets VI*. University of Arizona Press, Tucson SN, 2014.

N. Ohashi, M. Hayashi, P. T. P. Ho, and M. Momose. Interferometric Imaging of IRAS 043682557 in the L1527 Molecular Cloud Core: A Dynamically Infalling Envelope with. *ApJ*, 475:211–223, 1997.

P. Padoan, T. Haugbølle, and A. Nordlund. Infall-Driven Protostellar Accretion and the Solution to the Luminosity Problem. *ApJ*, 797(1):32, 2014.

G. Pelletier and R. E. Pudritz. Hydromagnetic disk winds in young stellar objects and active galactic nuclei. *ApJ*, 394:117–138, 1992.

T. Peters, R. Banerjee, R. S. Klessen, and M.-M. M. Low. The Interplay of Magnetic Fields, Fragmentation, and Ionization Feedback in High-Mass Star Formation. *ApJ*, 729(1):72, 2011.

D. J. Price. Smoothed particle hydrodynamics and magnetohydrodynamics. *J. Comput. Phys.*, 231:759–794, 2012.

A. Sanna, R. Cesaroni, L. Moscadelli, Q. Zhang, K. M. Menten, S. Molinari, A. Caratti o Garatti, and J. M. De Buizer. A subarcsecond study of the hot molecular core in G023.01-00.41. *A&A*, 565:A34, 2014.

D. Seifried, R. Banerjee, R. S. Klessen, D. Duffin, and R. E. Pudritz. Magnetic fields during the early stages of massive star formation - I. Accretion and disc evolution: Magnetic fields in massive star formation. *MNRAS*, 417(2):1054–1073, 2011.

D. Seifried, R. E. Pudritz, R. Banerjee, D. Duffin, and R. S. Klessen. Magnetic fields during the early stages of massive star formation - II. A generalized outflow criterion: Magnetic fields in massive star formation - II. *MNRAS*, 422(1):347–366, 2012.

F. Shu, J. R. Najita, E. Ostriker, F. Wilkin, S. Ruden, and S. Lizano. Magnetocentrifugally driven flows from young stars and disks. 1: A generalized model. *ApJ*, 429:781–796, 1994.

H. C. Spruit. Essential magnetohydrodynamics for astrophysics. 2013.

B. Stecklum, A. Caratti o Garatti, S. Klose, and P. Wiseman. Mid-Term Near-Infrared Variability of the Massive Young Stellar Object RAFGL 7009S associated with G25.65+1.05. *ATEL*, 10842, 2017.

J. C. Tan, S. Kong, M. J. Butler, P. Caselli, and F. Fontani. The Dynamics of Massive Starless Cores with Alma. *ApJ*, 779(2):96, 2013.

K. Tomida, K. Tomisaka, T. Matsumoto, Y. Hori, S. Okuzumi, M. N. Machida, and K. Saigo. Radiation Magnetohydrodynamic Simulations of Protostellar Collapse: Protostellar Core Formation. *ApJ*, 763(1):6, 2013.

K. Tomida, S. Okuzumi, and M. N. Machida. Radiation Magnetohydrodynamic Simulations of Protostellar Collapse: Nonideal Magnetohydrodynamic Effects and Early Formation of Circumstellar Disks. *ApJ*, 801(2):117, 2015.

K. Tomisaka. Collapse of Rotating Magnetized Molecular Cloud Cores and Mass Outflows. *ApJ*, 575:306–326, 2002.

B. Vaidya, C. Fendt, H. Beuther, and O. Porth. Jet Formation from Massive Young Stars: Magnetohydrodynamics Versus Radiation Pressure. *ApJ*, 742(1):56, 2011.

P. Wang, Z.-Y. Li, T. Abel, and F. Nakamura. Outflow Feedback Regulated Massive Star Formation in Parsec-Scale Cluster-Forming Clumps. *ApJ*, 709(1):27–41, 2010.

H. W. Yorke and C. Sonnhalter. On the Formation of Massive Stars. *ApJ*, 569:17, 2002.

H. Zinnecker and H. W. Yorke. Toward Understanding Massive Star Formation. *ARA&A*, 45 (1):481–563, 2007.